



UNIVERSITA' DEGLI STUDI DI PADOVA
DEPARTMENT OF INDUSTRIAL ENGINEERING
MASTER DEGREE COURSE IN MECHANICAL ENGINEERING

Master degree thesis in Mechanical Engineering

**THERMO-FLUID DYNAMICS DESIGN OF THE
COOLING SYSTEM FOR AN AUTOMOTIVE
BATTERY PACK**

Supervisor: Prof. Pierfrancesco BRUNELLO

Student: LUCA BARBETTA 1182326

ANNO ACCADEMICO 2018 - 2019

LUCA BARBETTA

**THERMO-FLUID-DYNAMICS DESIGN
OF THE COOLING SYSTEM FOR AN
AUTOMOTIVE BATTERY PACK**



Master's degree thesis

Supervisor: Prof. Pierfrancesco Brunello

Università degli studi di Padova
Department of industrial engineering
Master's course in mechanical engineering
December 2019

To those who are not afraid of the dark

Abstract

This thesis describes the process of design and verification of the cooling system for a specific battery pack, made of lithium cells with 18650 format, along with a summary of the design process that led to the electrical configuration of the pack.

The liquid cooling system has been conceived in order to exploit the higher axial thermal conductivity of the cylindrical cells and provide the best cooling uniformity possible, despite the complex shape of the pack.

An analytical feasibility study on the fluid flow, along with the coupling of the battery side with the air radiator, suggested the possibility of the system to reach the desired performance.

To quantify the thermal resistance between the soldered cells and the cooling devices walls, an experimental measure has been carried out and replicated in a finite elements model, in order to calibrate a localized resistance and implement it in the final numerical 3D simulation. The complete simulation suggested modifications to the cooling devices geometry to optimize the liquid flow, adjustments to the flow rates and an estimate of the maximum temperature reached by the cells and the maximum temperature difference between them.

Contents

1	Summary in Italian - Riassunto in Italiano	1
2	Introduction	7
2.1	Project history and first choices	8
2.2	Thesis structure	8
3	Battery pack design overview	11
3.1	Objectives	11
3.2	Other initial design considerations	15
3.3	Electrical configuration	20
4	Technological scouting	23
4.1	Previous art	23
4.2	18650 thermal properties	24
4.3	Cooling configuration	25
4.4	Cooling homogeneity	27
5	Parameters and precursory data	31
5.1	Cells heat generation	32
5.2	Connection plates heat generation	33
5.3	Conduction calibration	35
6	Feasibility study	43
6.1	Radiator performance	43
6.2	BCPs performance	45
6.3	System steady state	47
7	Exchangers manufacturing	51
8	Numerical simulation	53
8.1	Objectives of the simulation	53
8.2	Geometry simplifications	54
8.3	Meshing	55
8.3.1	Conformal mesh interruption	56
8.3.2	Meshing methods, sizings and results	57
8.3.3	Meshing problems	64
8.4	Ansys Fluent	65

8.4.1	Mathematical models	65
8.4.2	Setup	67
8.4.3	Solution convergence	67
8.5	Results	69
8.5.1	Fluid flow	71
8.5.2	Temperature and pressure	73
8.5.3	Comparison of the flow with and without spirals . .	76
8.6	Comments	77
9	Conclusions	79
10	Future developments	81
A	Data-logger calibration	85
B	Matlab scripts	87

List of Figures

2.1	Front view of the frame's CAD model	9
2.2	Rear view of the frame's CAD model	10
3.1	Mugello combustion moto3 telemetry	12
3.2	A common torque curve for a 250cc racing engine	13
3.3	Battery case in its final position	14
3.4	Lithium ion battery life vs. temperature	14
3.5	Pouch cells disposition attempt number 1	15
3.6	Pouch cells disposition attempt number 2	16
3.7	Popular battery chemistries and properties	16
3.8	Cells' honeycomb geometry	18
3.9	Cells' disposition	18
3.10	Cells' disposition in the frame from the side	19
3.11	Cells' disposition from above	19
3.12	Electrical connection plates	20
3.13	Electrical connection plates: detail	21
4.1	Internal structure of a 18650 cell	24
4.2	BCPs placement	26
4.3	Thermal pad layer	27
4.4	Comparison between spiralic and radial flow	28
4.5	Central BCP internals	29
4.6	Lateral BCP internals	29
4.7	Inlets position detail	30
5.1	Electrical simulation of a compact plate	33
5.2	Electrical simulation of a long plate	34
5.3	Example of positive tab structure of a 18650 cell	36
5.4	Tabs setup for measure	36
5.5	Resistors setup for measure	37
5.6	The cold side of the conduction measure	38
5.7	Measure setup: thermal coupling and isolation	38
5.8	Graph of the conduction measure	39
5.9	Cell conduction equivalence scheme	40
5.10	Cell conduction simulation	42
6.1	Radiators disposition on the bike	44
6.2	Radiator performance varying air speed, plots	45

6.3	Radiator-battery system scheme	48
6.4	Radiator-battery coupling iteration scheme	49
7.1	Spirals holder	52
8.1	Symmetry and others simplification	54
8.2	Cells, plates and in/outlets simplifications	55
8.3	Exchanger simplification	55
8.4	Mesh orthogonal quality chart	58
8.5	Inlets/outlets meshing detail	58
8.6	Mesh overview of the lateral fluid domain	59
8.7	General mesh settings	59
8.8	Cells mesh settings	60
8.9	Electrical plates and thermal pads mesh settings	61
8.10	Exchangers mesh settings	62
8.11	Spiral's tip and fluid thickness mesh	63
8.12	Meshing method for in/outlets ducts	63
8.13	Error in meshing	64
8.14	Problem in meshing	65
8.15	Complete temperature contour	69
8.16	Significant cells axes positions	70
8.17	Fluid flow improvements	72
8.18	Contours of temperature and pressure	73
8.19	Temperature of the cells' axis	74
8.20	Horizontal section temperature contour	74
8.21	Horizontal section temperature contour, detail	75
8.22	Streamlines and temperatures without spirals	76

List of Tables

5.1	Thermal conductive layers characteristics	41
6.1	BCPs geometry data	45
6.2	BCP performance study	46
8.1	Mass flow on single outlets and percentage of the total flow	70
8.2	Fluent's heat transfer coefficients and conduction check . .	71
8.3	Heat transfer coefficients without spirals	77

Chapter 1

Summary in Italian - Riassunto in Italiano

La tesi è incentrata sulla progettazione e simulazione 3D del sistema di raffreddamento per una batteria al litio, nata per fornire energia a un prototipo di moto3 equivalente a propulsione elettrica.

Il progetto nasce, esternamente all'università, da un gruppo di studenti, ex-studenti e professionisti appassionati di motorsport.

In questo contesto viene definito il telaio e certi obiettivi prestazionali per la batteria, tra cui avere energia sufficiente a percorrere 60 km, con l'andamento tenuto in pista da una classica moto3 a combustione, ed essere rimovibile dal veicolo; il motore scelto eroga 35 kW continui e 70 kW per pochi secondi.

Nella progettazione è perseguito un compromesso soddisfacente fra massima efficienza di raffreddamento, omogeneità dello stesso all'interno del pacco, facilità ed economicità di realizzazione del sistema.

Per limitare le correnti in gioco, responsabili del calore prodotto per effetto Joule, la tensione massima viene scelta pari a quella massima sostenibile dal motore: 400 V.

Per formare il pacco, dopo svariati tentativi e ricerche, sono state scelte le celle cilindriche formato 18650, a causa della loro affidabilità e capacità di tassellare lo spazio poligonale a disposizione.

Le celle sono state disposte con asse allineato alla direzione trasversale al veicolo, raggruppate a nido d'ape (figura 3.9); il telaio è stato leggermente allargato per ospitare 3 pile di celle, una in fianco all'altra, con i poli delle celle affacciati.

La connessione elettrica fra le celle è ottenuta con lamine di rame con spessore 0.2 mm, saldate tramite spot-welding o, preferibilmente, con tecnica laser.

La configurazione elettrica raggiunta dopo un breve studio di fattibilità è riassumibile con la sigla 96S-11P : 96 pacchetti di celle collegati in parallelo, contenenti ognuno 11 celle, per un totale di 1056; in questo modo la

tensione massima del pacco è di 403.2 V e la capacità nominale è di circa 35 Ah.

Il sistema di raffreddamento è stato quindi studiato tenendo conto delle soluzioni comunemente adottate; queste tuttavia sembrano non sfruttare una caratteristica fondamentale delle celle al litio: l'ortotropia della conduzione termica. Le celle cilindriche presentano infatti una conduzione termica assiale di due ordini di grandezza maggiore rispetto a quella radiale: utilizzare la superficie laterale del cilindro per il raffreddamento risulta così molto meno efficiente che utilizzare le due basi.

Sulle due basi sono tuttavia presenti i poli elettrici della cella e la struttura del polo positivo (figura 4.1 e 5.3), a causa della presenza di alcuni sistemi di sicurezza, risulta complicata e non simulabile nel dettaglio in una simulazione estesa del pacco pile; per questo motivo, è stata condotta una misura sperimentale (figure 5.4, 5.5, 5.6 e 5.7) delle caratteristiche di conduzione termica delle strutture interne di una comune 18650, ottenendo un prezioso dato (figura 5.10) inserito poi nella simulazione numerica. La configurazione di raffreddamento adottata prevede delle piastre di raffreddamento ad acqua (chiamati BCP, da Battery Cooling Plates), all'interno della batteria, ed un classico radiatore ad aria esterno ad essa (figure 4.2 e 6.1).

Un raffreddamento ad aria sarebbe stato più semplice ed economico, tuttavia non avrebbe permesso di alloggiare la stessa quantità di celle e raggiungere quindi la capacità desiderata.

Dei BCP metallici (in rame per le massime prestazioni e facilità di costruzione) molto sottili sono stati quindi ipotizzati, posizionati nell'intercapedine tra un raggruppamento e l'altro.

Due BCP più spessi (3 mm di passaggio fluido) raffredderanno sia il raggruppamento centrale che quelli laterali e sono per ciò chiamati "centrali", mentre due più sottili (2.5 mm) raffredderanno solo i gruppi laterali, e sono per ciò chiamati "laterali"; le pareti di scambio termico dei BCP, spesse 0.5 mm, devono essere il più sottili possibile per agevolare lo scambio termico, ma devono anche avere una discreta rigidità per sostenere la pressione dei tiranti, descritti più avanti.

Per rendere il più possibile omogeneo il raffreddamento, il liquido viene fatto arrivare al centro dei BCP (aprendo un varco fra le celle del raggruppamento laterale per lasciar spazio alle tubazioni) e viene fatto fluire in canali spiralitici (figure 4.5 e 4.6), ottenuti brasando delle paratie fra le due pareti dei BCP, fino ad essere estratto da uscite multiple al perimetro: sono presenti 4 canali nel BCP centrale (con altrettante uscite) e due in quello laterale.

I BCP metallici devono beneficiare di un ottimo contatto termico con le celle, ma contemporaneamente devono rimanere isolati dalle piastre di conduzione; per ottenere questo, uno strato di materiale elastomerico termoconduttivo, comunemente conosciuto in elettronica come thermal pad, viene interposto fra BCP e piastre elettriche.

Essendo il Thermal pad un materiale elastoplastico, ulteriori accortezze

sono necessarie per mantenere, anche in caso di danneggiamento del pacco pile, i BCP isolati dalle celle, pena cortocircuito delle stesse con conseguenze catastrofiche.

Al contempo, una matrice di tiranti comprimerà lateralmente il pacco per assicurare pressione sulle interfacce tra rame e thermal pad, riducendo così le resistenze di interfaccia.

Un importante dettaglio della costruzione concerne l'accoppiamento termico fra le celle e le piastre di conduzione elettrica: la saldatura a punti infatti tende a non creare un contatto termico ottimale e, come accennato prima, il polo positivo della cella presenta varie cavità che si oppongono al passaggio di calore.

Un notevole miglioramento nella misura della resistenza termica è stato ottenuto, in fase di saldatura a punti della piastra di conduzione, distribuendo della pasta, decapante e contenete stagno bassofondente, nella zona di saldatura: fondendo durante la saldatura va a riempire l'intercapedine per capillarità, espellendo l'aria e riducendo molto la resistenza di interfaccia.

Dal lato del polo positivo, la resistenza termica è stata dimezzata riempiendo gli intercapedini (accessibili dall'esterno) con una buona pasta termica: la soluzione richiederà tuttavia di verificare che la pasta, una volta seccata, non precluda il funzionamento della valvola di emergenza e non comporti una eccessiva autoscarica della cella.

Per quanto riguarda la verifica del sistema, uno studio di fattibilità (tabella 6.2) sulle capacità refrigeranti del flusso di liquido è stato eseguito prima della simulazione numerica, modellando i canali come rettilinei e con un flusso di calore imposto; il calore prodotto dal pacco pile è stato ottenuto sommando il calore per effetto Joule nelle celle (stima di prima approssimazione, il valore effettivo verrà misurato sperimentalmente successivamente alla stesura di questo trattato) e nelle piastre di conduzione, per le quali una veloce simulazione termo-elettrica si è resa necessaria.

Tramite un software (appendice B, capace di calcolare il calore scambiato dai radiatori sportivi, è stato possibile calcolare i parametri di regime del sistema accoppiato batteria-radiatore e questo ha permesso di verificare approssimativamente se i BCP potessero essere in grado di mantenere le celle a una temperatura sicura nonché quale portata fosse necessaria per farlo.

Ottenuti questi dati, una simulazione numerica della batteria completa (sfruttando la sua simmetria) è stata allestita in ANSYS Fluent, per verificare non solo che la temperatura massima fosse sostenibile dalle celle, ma anche che la temperatura fosse il più possibile uniforme.

L'uniformità del raffreddamento è infatti un problema molto sentito nel campo dell'accumulazione elettrica, in quanto sia le performance che la vita utile delle celle sono fortemente influenzate dalla temperatura operativa.

La simulazione tridimensionale, senza ridurre le pareti attraverso cui avviene lo scambio termico a pareti bidimensionali, è stata necessaria ad indagare l'interazione fra i due BCP e la distribuzione di temperatura in tutta la batteria.

Le guide spirali del flusso, nonché la posizione dei tiranti, sono state modificate per ottenere un flusso ordinato e a velocità il più possibile uniforme; le spirali consentono infatti, al contrario del flusso radiale, di convogliare il fluido agli outlet evitando zone ferme e di controllare la velocità del fluido in funzione della distanza dal centro.

La mesh della geometria si è rivelata estremamente complicata, probabilmente a causa delle spline utilizzate nella fase di CAD per definire le spirali, generando frequenti e inspiegabili errori da parte del software di meshing e impedendo di ottenere una mesh intelligente.

Si è quindi rivelato necessario infittire la mesh, in modo poco discriminato fino al limite hardware della macchina, non riuscendo tuttavia a ottenere un abbassamento soddisfacente del residuo dell'equazione di continuità.

Tuttavia, siccome parametri importanti come la differenza fra il flusso di liquido in entrata e in uscita e la differenza tra il calore prodotto dalle celle e quello trasferito al liquido erano sufficientemente basse, i risultati della simulazione sono stati ritenuti comunque significativi.

E' stato quindi possibile determinare che, con la batteria che produce 3258 W in calore e una temperatura dell'aria esterna di 40 °C che arriva al radiatore alla velocità di 182 km/h, la temperatura massima raggiunta dalle celle è di 60,0 °C e che la massima differenza di temperatura tra due celle è di 5,02 °C, mentre all'interno della stessa cella è di circa 3 °C.

Questi valori sono ritenuti comunque una sovrastima, in quanto nella realtà ci sarà una componente di raffreddamento passivo, dato dalla radiazione e dalla convezione con l'aria esterna, che ridurranno sia la temperatura massima che la massima differenza all'interno del pacco; il gradiente instaurato dal raffreddamento passivo sarà infatti contrario a quello forzato dal sistema di raffreddamento attivo e tenderà ad annullarlo.

Dalla simulazione è emersa un leggero sbilanciamento tra il calore asportato dai due BCP, leggermente in favore del laterale, probabilmente a causa del metodo di calcolo adottato nello studio di fattibilità. Si sono inoltre confrontate le prestazioni del sistema di raffreddamento con il caso in cui vengano rimosse le guide spirali all'interno dei BCP e il vantaggio risulta notevole, sia in termini di uniformità che di temperatura assoluta.

Tra i futuri sviluppi si annovera sicuramente la misura sperimentale dell'effettivo calore generato dalle celle, una volta scelto il modello commerciale da utilizzare; la costruzione di un modello ridotto della batteria, per verificare i metodi di produzione e misurare sperimentalmente le prestazioni del sistema; la ricerca di un accoppiamento termico migliore di quello fornito dallo strato di thermal pad.

Si individuano infine alcuni limiti del design, ad esempio la difficoltà di sostituzione di una eventuale cella difettosa e il rischio di corto circuito di un intero pacco parallelo se una singola cella dovesse cortocircuitare. Sulla geometria interna degli scambiatori è stata depositata una domanda di brevetto.

Chapter 2

Introduction

Nowadays electric vehicles development is a fast-emerging market and nearly every vehicle constructor has an electric model in its catalog.

Along with consumer-grade vehicles, electric racing vehicles and championships are appearing on the scene.

The racing environment, however, suffers the fan's nostalgia for roaring engine noise, gasoline and oil smell.

This is probably among the reasons why racing motorcycles producers have mainly developed powerful, heavy bikes, capable of proving the brute force nature of electric drive-trains; this approach leaves the low-power branch relatively uncovered.

An important side effect of this philosophy is the tight structural fusion of the entire bike with his power source, meaning the battery pack.

Not having reached the energy-to-weight ratio of the fossil fuels, the battery pack ends up taking a huge amount of the total bike weight, which is often 30-50% heavier than a regular internal combustion bike.

Indeed, the battery of a motoGP-like electric bike weighs more than 100 kg, for a race autonomy of about 50 km, and its replacement requires several minutes at least. [1] [2]

In addition, a 100 kg block is not easily manageable: it needs at least three people to move it securely (or one/two people and a workshop crane), not to mention that handling a night stand-sized box is difficult for three people.

If the battery pack would weigh about a half of that, two people (or one person using a crane) would be able to move it with ease.

This would mean that the bike can be separated from its battery and coupled with a fully charged one for a brand new ride; this also allows to charge the battery in a safe container, away from people and equipment.

These considerations are the main reasons that drive Corvedo Motors' work and its dedication to designing an electric racing motorbike.

The battery's cooling is the most challenging part of its design.

The problems deriving from a low cell temperature ($< 10\text{ }^{\circ}\text{C}$) will not be considered, since not recurring in racing environment.

Lithium cells with high energy-to-weight ratio have, in most cases, a maximum operative temperature of 60 °C and an optimal range between 25 and 45 °C. [21]

In a hot and windless summer day, the air directly above the asphalt can easily reach and rise above 40 °C in some tracks.

While a combustion engine has an operative temperature of about 80-90 °C and the temperature difference with external air is around 40-50 °C, in the case of a battery this difference stands at about 15-20 °C.

The limited temperature difference means that, to remove the same amount of heat, the cooling system must be, proportionally, more efficient.

On the other hand, an electric battery produces way less heat than a combustion engine, thus making the problem manageable.

In addition, more complications rise from the removable battery feature: therefore the battery pack case must be as compact and light as possible.

2.1 Project history and first choices

A summary of the project's history (and the group developing it) is necessary to understand some of the choices made.

The group, born in 2016 essentially for hobby, put together engineers, engineering students and professionals in the field.

It initially carried up the design of a traditional combustion Moto3 bike and, after obtaining a mainly complete design on CAD in 2018, decided to convert the design to hold an electric power train and pursue its realization and commercialization.

The frame design, with two lateral aluminum beams, has been revised and adapted from the combustion project with some changes: the combustion engine block is not stiffening the frame any longer; its structure can be easily appreciated from figures 2.1 and 2.2.

The main constraint has been the frame width: it initially being equal to the combustion model and subsequently increased by some millimeters to accommodate the final battery configuration.

2.2 Thesis structure

The next two chapters will describe the intuitive phase of the design, where as many considerations and problems as possible are taken into account to identify the most suitable solution, both from the electric and thermal perspective.

Once a satisfactory general configuration is reached, some precursory data is calculated/measured to be used in a feasibility study, which will quickly prove if the system performance can meet the expectations and provide some starting values for the numerical simulation.

The main uncertainty in the modeling is due to the multiple conduction layers coupled with the complicate internal structure of the cell, thus a measure to determine the thermal resistance of said design will be described.

After the description of a manufacturing process to produce the cooling devices, the numerical simulation of the entire pack will be described and its results discussed, to highlight limits and performance of the system.

In conclusion, further refinements of the simulation and experiments programmed will be discussed.

A clarification: some parameters are not yet fully determined during this thesis and the results reported are an example of the study; for example, since the actual cells that will be used in the battery are not determined yet, the internal resistance (and thus the heat generated by the battery) has been chosen to be plausible and is, thanks to several attempts and partial solutions during the thesis, most likely to make the system pass the last checks.

The present procedure represents, anyway, a valid example for a performance study of the designed system.

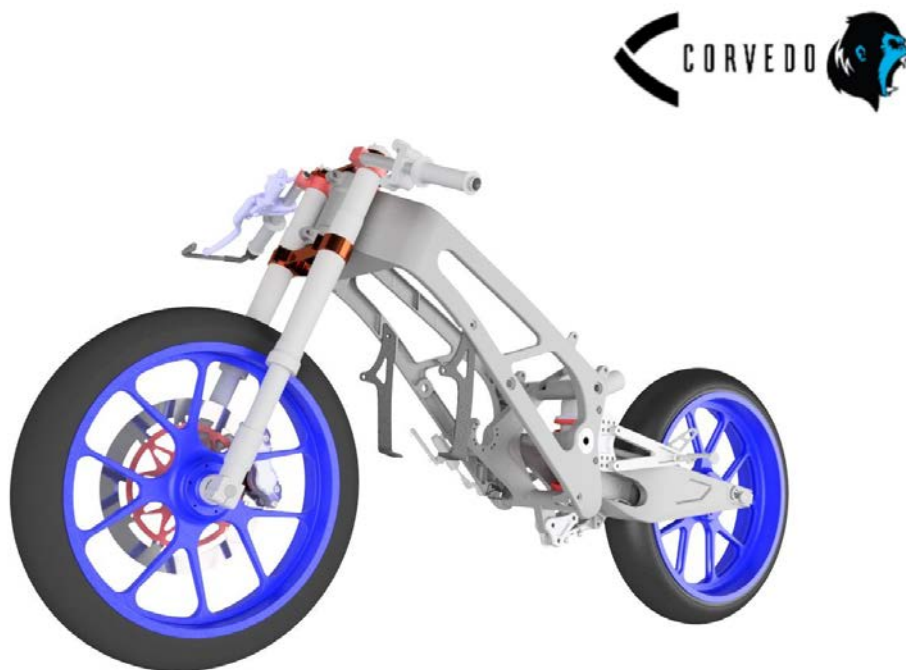


Figure 2.1: Front view of the frame's CAD model

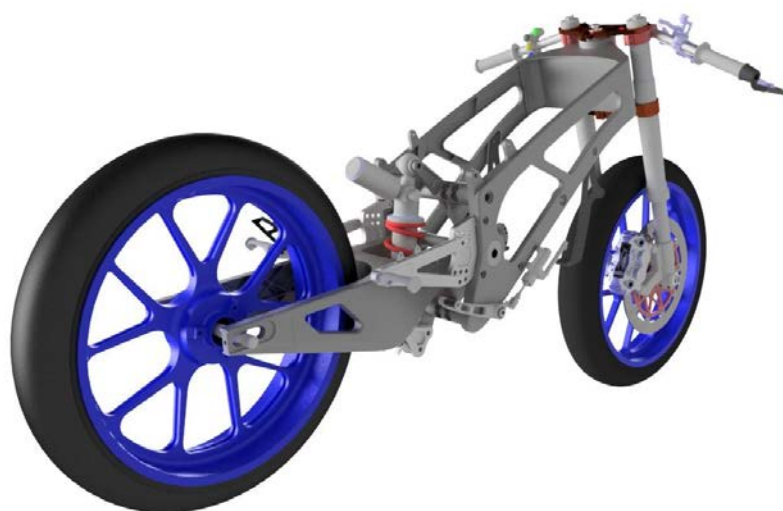


Figure 2.2: Rear view of the frame's CAD model

Chapter 3

Battery pack design overview

In this section the objectives of the design will be listed and described, along with the first considerations on the pack characteristics, cells type, disposition and electrical connection.

3.1 Objectives

The design of the entire motorcycle started from few clear target performance and characteristics, analyzed here in order to understand the constraints of the design and obtain some initial data.

High autonomy: the target event the bike must be able to complete is the TTZero, in a high speed track of about 60 km.

The telemetry of a combustion moto3 during a lap at Mugello circuit has been obtained from a friendly team and is plotted in figure 3.1.

Supposing a common torque curve (figure 3.2) for the engine and using the RPM and TPS telemetry, the power developed by the engine in each moment has been computed.

By integration of the latter curve, the necessary energy to accomplish a lap at that pace has been valued (about 750 Wh/lap).

This way, the esteem of the energy needed to travel 60 km, with 35 kW as maximum power and the “duty cycle” of the Mugello circuit, has been done:

$$750 \frac{Wh}{lap} \cdot \frac{60km}{5.245 \frac{km}{lap}} \approx 8500Wh$$

since 5.245 km is the length of the Mugello circuit.

To preserve the battery and prolong its life, it’s good practice to drain only a fraction of the nominal capacity; for this reason the choice of **draining only two thirds of the nominal capacity** has been made.

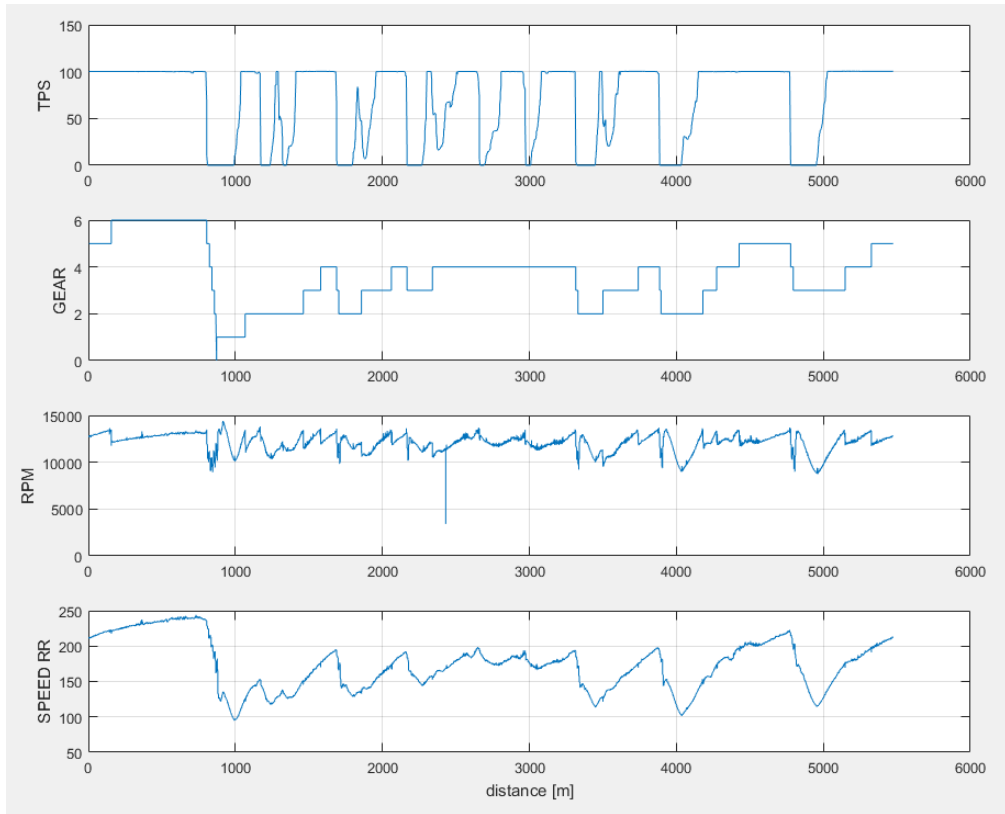


Figure 3.1: Mugello combustion moto3 telemetry, used for the needed energy esteem

$$8.5 \text{ KWh} \cdot 3/2 = 12.75 \text{ KWh} \quad \text{Battery design energy}$$

This goal is, clearly, one of the most important of the design. To achieve this autonomy, contain dimensions, weight and cost while maintaining a reasonable reliability of the system, lithium-based cells have been judged as the best compromise [7]; further considerations will follow.

Easy battery swap: its position must be easy to access, surrounded by an adequate extraction space and, possibly, exploit the room between the frame's beams; its shape must be compact for an easy handling and to facilitate cooling homogeneity.

Indeed, multiple different packs distributed in the frame would require a monitoring system, assuring that the average temperature of a pack is equal to the others, while an unique pack would homogenize himself through inside heat conduction.

A low position with extraction from the bottom would need additional devices to lift the vehicle and support the battery.

A lower position with lateral extraction would instead require a higher pass for the frame (with consequent loss of stiffness) and a less compact design of the battery pack; it would mean a very low center of mass and a more complicated transmission layout, since the motor could not be directly

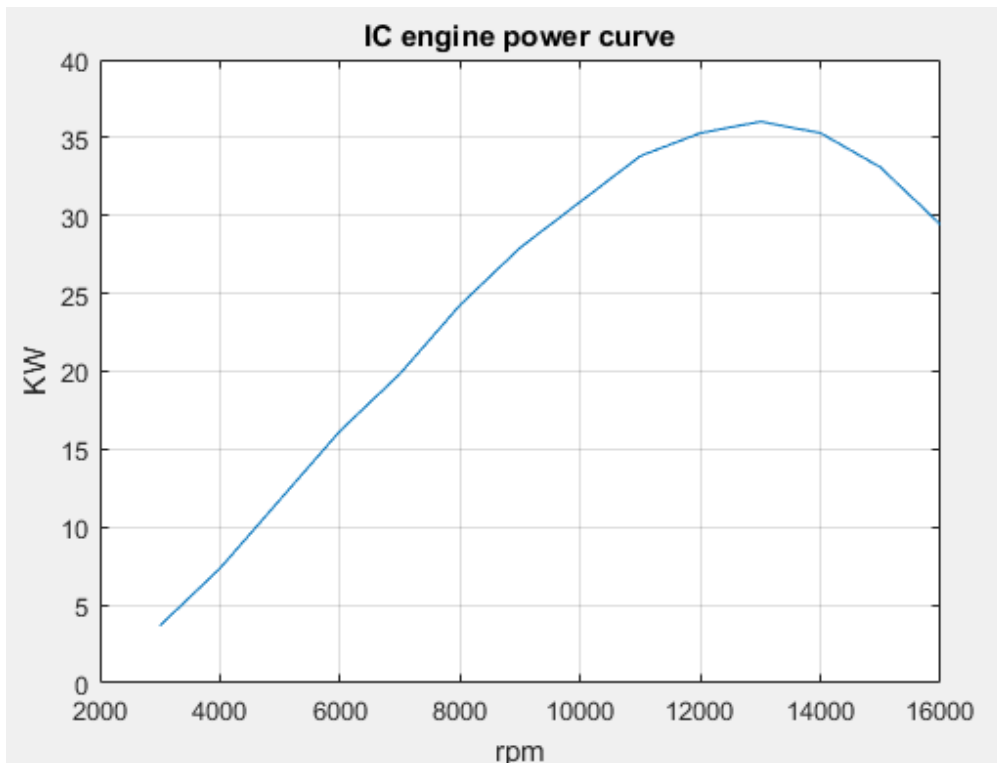


Figure 3.2: A common torque curve for a 250cc racing engine has been supposed

keyed to the pinion shaft¹.

An upper position, with extraction from above, approximately in place of the gas tank, would meet the above-mentioned requirements; however, it would entail a high center of mass.

This last solution has been chosen and in figure 3.3 the reader can appreciate the battery case in its final position, although the case shape is at an intermediate stage.

Highly efficient cooling: As mentioned in the introduction, the limited temperature difference between the cells and the external air makes the efficiency of the cooling system of primary importance.

Taking into consideration the worst case of **40 °C external air** temperature, and considering that the cells' temperature will be always higher, the more efficient the cooling system is, the more is probable to be able to maintain the cells in the optimal temperature range under any circumstances.

The **maximum acceptable temperature** will be considered equal to the maximum operative temperature stated by most high energy li-ion cells producers: **60 °C**; as figure 3.4 explains, above that temperature the life span begins to degrade significantly. [21]

For these reasons, the highest cooling performance have been pursued,

¹ The pinion position is determined by considerations on the vehicle's dynamics.

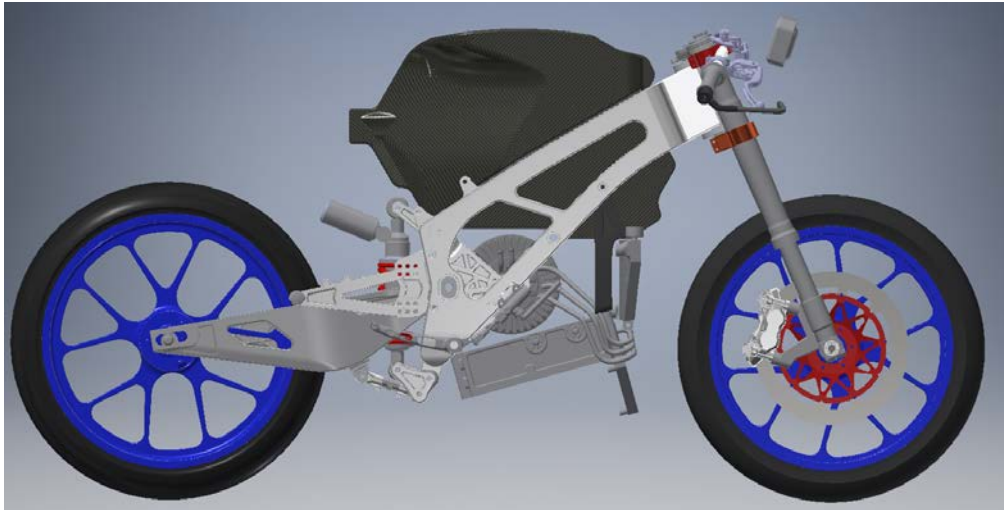


Figure 3.3: Battery case in its final position, although the shape is subject to modifications

while maintaining a reasonable system's cost and complexity.

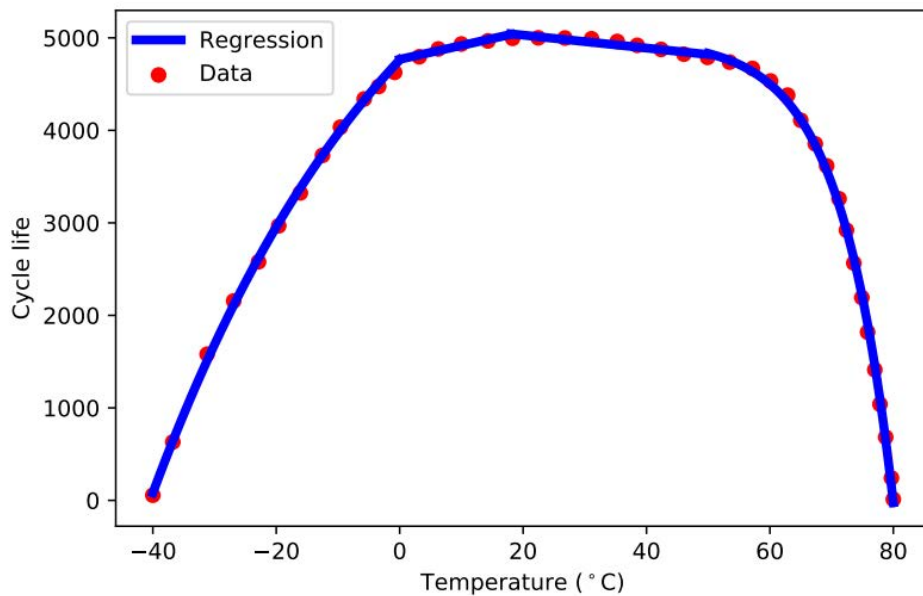


Figure 3.4: Lithium ion battery life vs. temperature

Cooling homogeneity: temperature affects in various ways the cells' performance: to mention some, it decreases the internal resistance and raises the voltage. [12]

Cells connected in the same pack, operating at different temperatures, contribute differently to the supplied power and thus wear differently; this can lead to low performance and/or shorten the useful life of the entire pack. [18]

For these reasons its important to maintain the best cooling homogeneity

achievable across the battery pack.

3.2 Other initial design considerations

Other considerations on the general design will be now explained.

One of the first components identified is the motor, a brushless synchronous capable of **35 kW continuous and 70 kW peak**.

The team got in touch with the motor producer and identified a suitable ESC (Electronic Speed Controller).

Pack voltage : The maximum voltage supported by the identified motor is **400V**.

A high operative voltage allows to contain maximum currents, responsible for Joule effect and thus for the heat produced by all the power train elements.

The pack series configuration will thus respect this limit and be close to it.

Cell type: A discretely long research for pouch/prismatic type cells didn't end up in a reliable, mainstream and sufficiently small cell.

The dimension of the cell is of crucial importance: a polygonal volume in the tank position has been assigned to the battery pack and the cells must be able to fill it up efficiently.

As depicted by figures 3.5 and 3.6, some attempts in arranging huge pouch cells in the volume assigned to the battery have been made: although the reached energy capacity was not even close to the one achievable with small format cells like 18650.

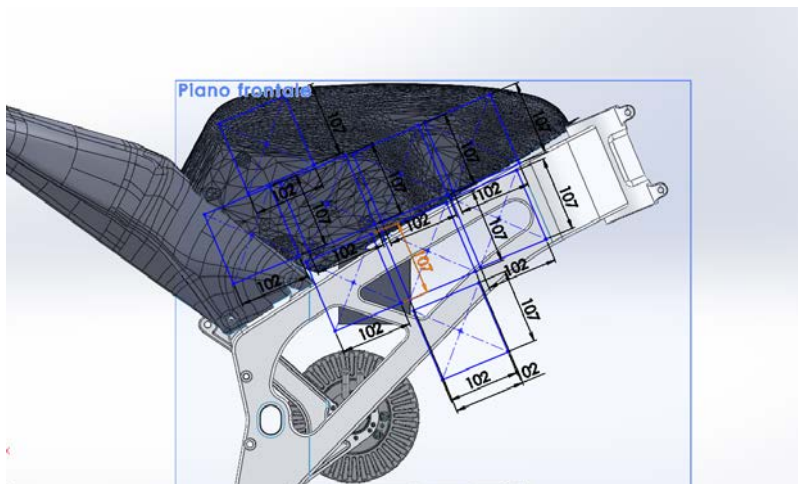


Figure 3.5: Pouch cells disposition attempt number 1

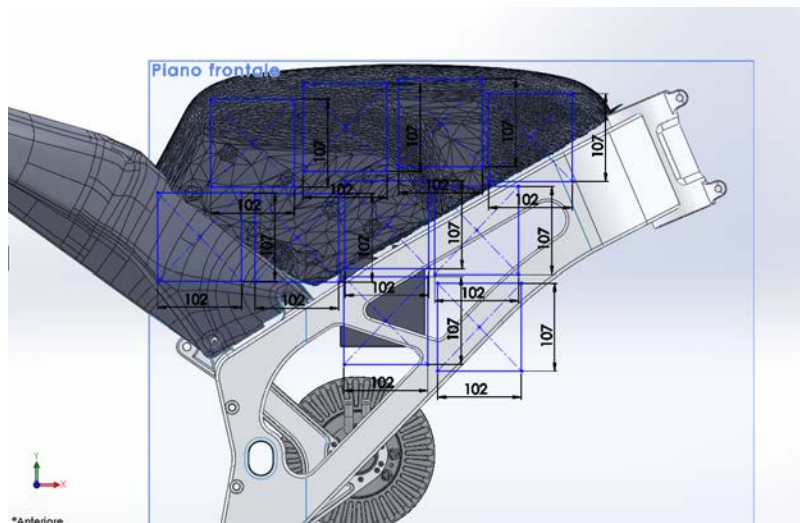


Figure 3.6: Pouch cells disposition attempt number 2

Pouch cells produced for radio controlled models are small and mainstream, but they have been judged to be not reliable enough. The **18650 format** has finally been chosen, due also to its long market history and large models range. As figure 3.7 summarize, the **NMC chemistry** (LiNiMnCoO_2 cathode) has been identified as the best for this application.

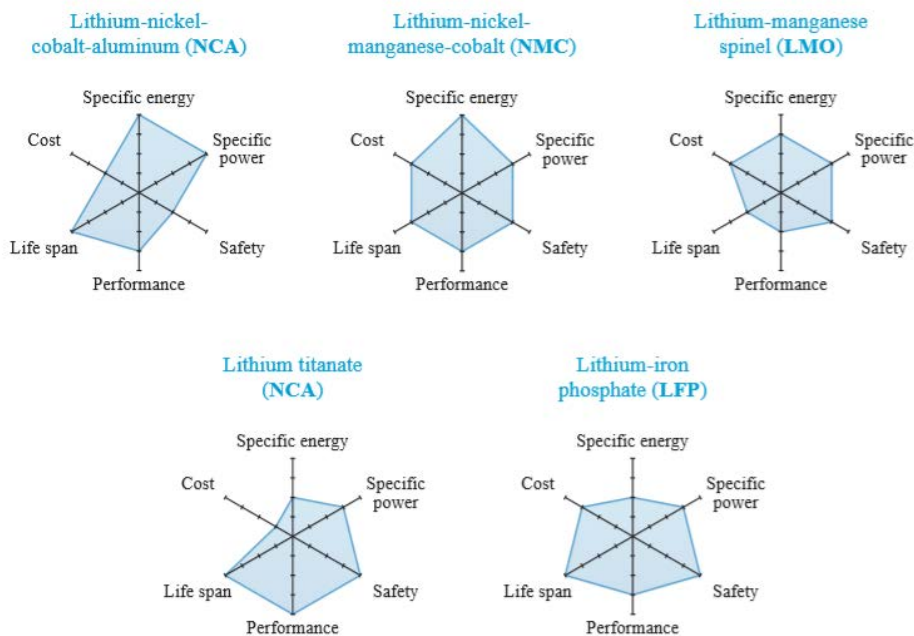


Figure 3.7: Popular lithium-based battery chemistry and their properties are illustrated by means of a polar chart, in which more distance to center means better (which corresponds to "cheaper" on the cost scale).

An example of common electrical characteristics of these cells are the following:

nominal voltage: 3.7 V

maximum voltage: 4.2 V

internal resistance: from about 5 m Ω to about 150 m Ω , depending on quality and chemistry.

capacity: from 2800 to 3500 mAh

discharge current²: up to 10C for some models.

Cells orientation and disposition: The available space for the cells' disposition was suggested by the shape of the gas tank of a typical moto3: the room for the pilot's legs had to be maintained.

After several layout tests, a good volume fill has been obtained arranging the cells with the axis oriented horizontally, transversely to the frame; the cells are organized in two or three stacks side by side, symmetrically with respect to the bike's plane of symmetry.

The cells have been arranged in a honeycomb-like structure here called stack, with 19.5 mm between the cells axes: this means 1.1 mm between the cells with 18.4mm cells diameter, as figure 3.8 clarifies.

The stacks are separated from each other by 5.4 mm, and from the frame by about 35 mm.

²The discharge rate is often expressed as a multiple of the capacity, divided by 1h: xC means that the nominal capacity can be drained in 1/x of an hour

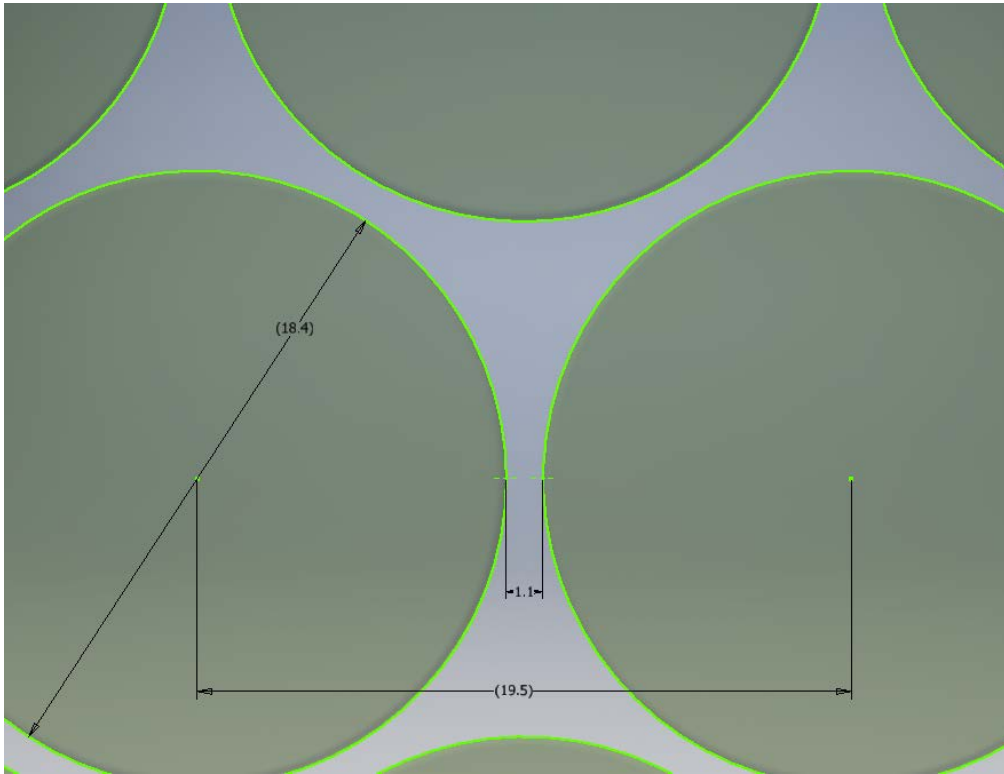


Figure 3.8: Cells' honeycomb geometry; cells are 18.4 mm in diameter, their axes' distance is 19.5 mm, the distance between cells is 1.1 mm

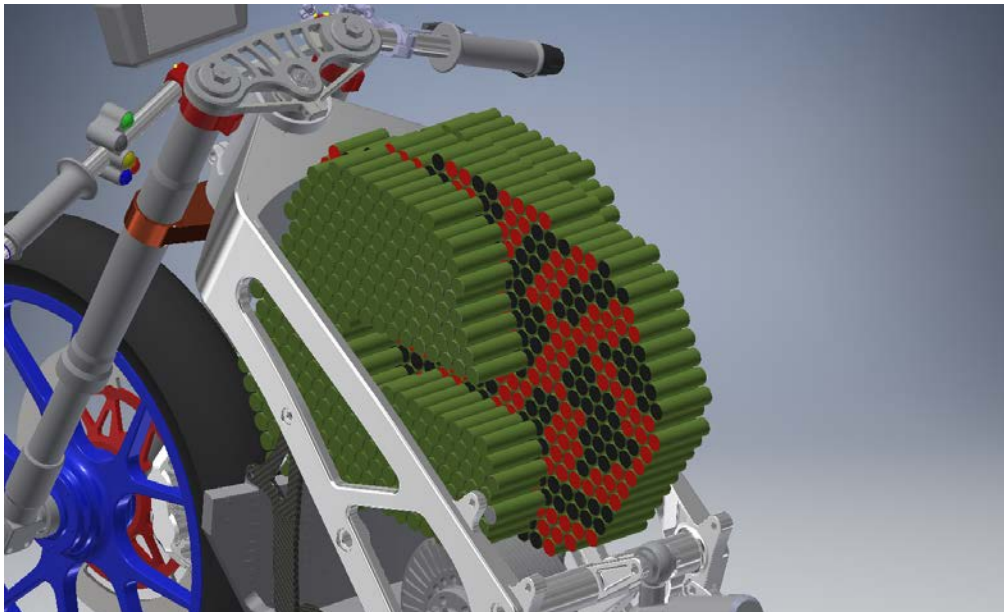


Figure 3.9: Cells' disposition; the C shape of the lateral stack will be clarified in section 4.3; the red (and black) cells' bases represent the positive (and negative) tab.

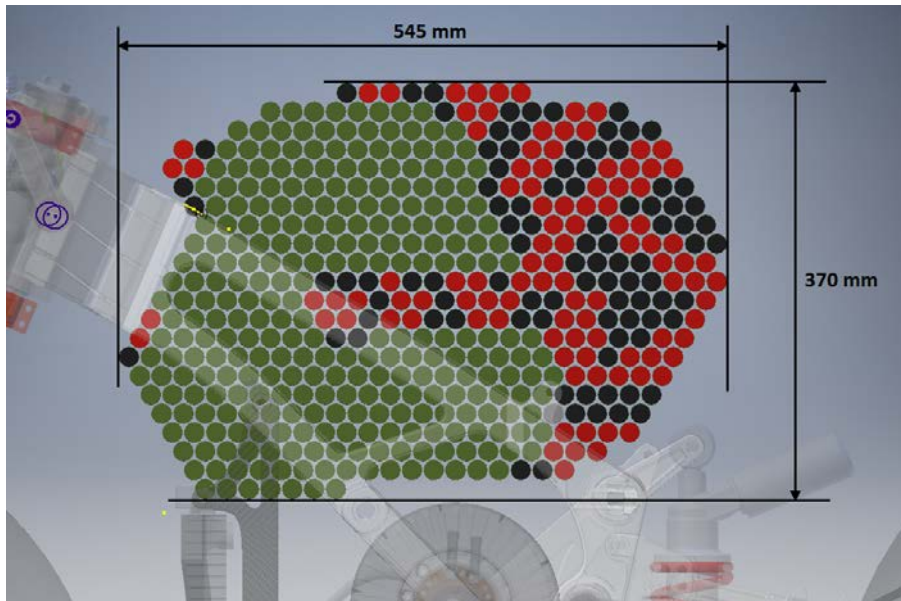


Figure 3.10: Cells' disposition in the frame from the side and overall dimensions; the central cells' tabs are marked with colors representing the polarity of the tab.

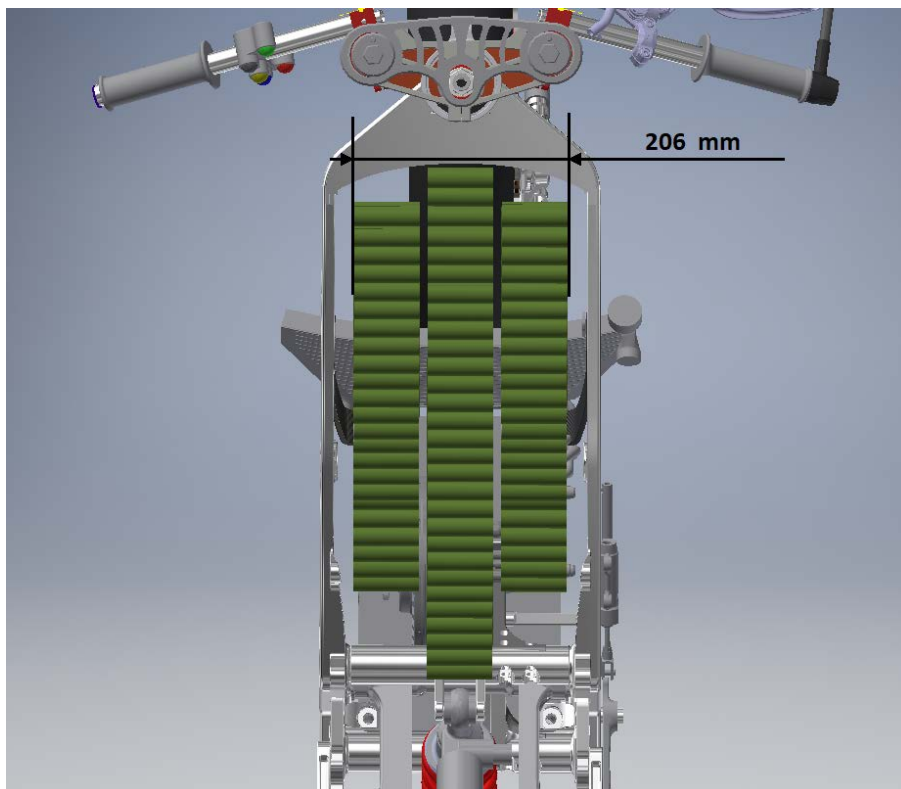


Figure 3.11: Cells' disposition from above: 5.4 mm between the stacks, 35 mm between the frame and a lateral stack.

Cells electrical connection: In most industrial application, 18650 cells are connected with 0.2mm nickel-coated steel stripes.

Indeed, most 18650 cells' cases are made with stainless steel and the nickel coating helps to achieve a good welding with cheaper material; in addition, the steel core offer a higher resistance than copper, and this helps to spot-weld, because the current is more likely to pass through the cell material and not short-circuit in the copper plate.

In this application, **0.2mm copper plates** will be used to connect the cells to exploit their lower resistance (that will make the Joule effect in the conduction plates negligible, as appreciable in section 5.2), even if the spot welding is much more difficult; in this regard a test will be conducted outside this thesis, to verify if the spot-welding heating can damage the cell.

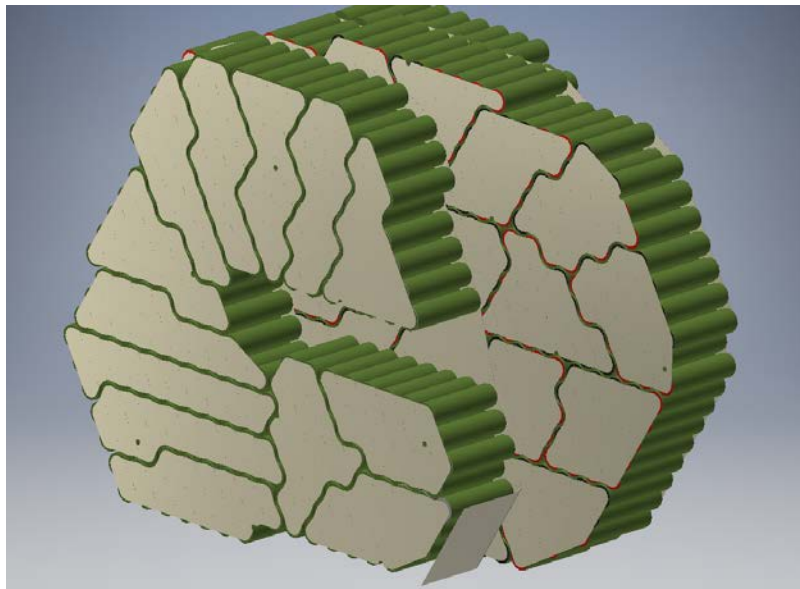


Figure 3.12: Electrical connection plates: on bottom-right one of the two battery output plates, not yet shaped.

3.3 Electrical configuration

In light of the considerations made until now, the pack series and parallel configuration can be determined.

A feasibility study from the electrical point of view, considering several combinations of parameters, led to a satisfactory configuration for the maximum autonomy battery model: a future model with reduced autonomy (and thus weight) is likely to be designed.

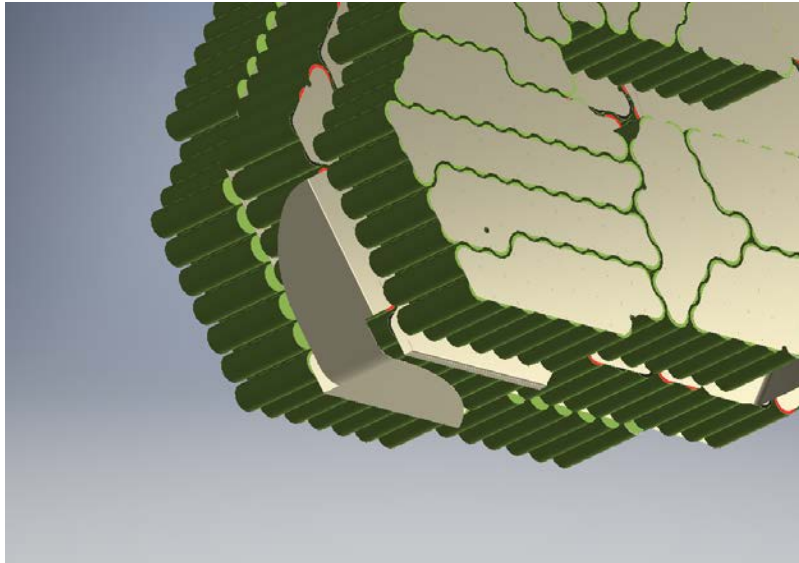


Figure 3.13: Electrical connection plates: detail of the plates connecting the stacks

The following cell characteristics are assumed³:

- nominal voltage : $V_n = 3.7 V$
- maximum voltage : $V_{max} = 4.2 V$
- minimum voltage: $V_{min} = 3.4 V$
- nominal capacity : $C_n = 3.2 Ah$

All the voltages are intended in a open circuit.

The minimum voltage is the cut voltage at which the cell will be considered discharged; further discharge is possible but would drastically reduce the battery life [17].

The nominal capacity is commonly measured by producers discharging the cell from 4.2 V to 2.5 V at a very low current. [8]

Since in this application the current will be conspicuous and the cut voltage is higher than the test one, the educated guess that **only two thirds of the nominal capacity will be actually drained** has been made, as previously stated.

The **pack configuration** reached is the following:

- number of cells : $N_C = 1056$
- number of series: $N_S = 96$
- number of parallels: $N_P = 11$
- abbreviation: 96S - 11P

³At the time of this feasibility study a specific product was not yet determined so a plausible set of properties was assumed

The **pack characteristics** can now be computed:

- nominal voltage** : $V_n \cdot N_S = 355.2 V$
- maximum voltage⁴ : $V_{max} \cdot N_S = 403.2 V$
- minimum voltage : $V_{min} \cdot N_S = 326.4 V$
- average voltage: $V_{av} = N_s \cdot (V_{max} + V_{min})/2 = 364.8 V$
- nominal capacity** : $N_P \cdot C_n = 35.2 Ah$
- effective capacity : $35.2 Ah \cdot 2/3 = 23.5 Ah$
- nominal energy estimated: $V_{av} \cdot 35.2 Ah = 12,84 KWh$

As you can notice, the nominal energy achieved is very close to the design one of 12.75 KWh.

The following are some application parameters calculated for a continuous 35 kW supply⁵ and a 70 kW (peak) one, that are as mentioned the limits of the motor.

	35 kW	70 kW
average current	96 A	192 A
average discharge rate	2.7 C	5.5 C

Where the average current is the ratio between the power and the average voltage, while the discharge rate is the ratio between the discharge current and the nominal capacity of the battery pack.

The discharge rate is compatible with most cells on the market.

⁴Even if the maximum voltage is slightly higher than the one the motor supports, is rare that the cells reach the very 4.20 V value and, anyway, a overvoltage of this entity has been judged not worrying

⁵The powertrain's efficiency has not been considered.

Chapter 4

Technological scouting

The first decision to make is about the cooling method.

To do so is mandatory the comprehension of a cell's thermal behavior and, even earlier, of its basic structure.

4.1 Previous art

Since the present thesis describes a battery pack made out of cylindrical cells, this section will focus on common cooling solutions for this type of cells.

There are, in literature, many systems exploiting different properties of various coolants: air cooling is discussed, for example, in [13], in [13] with a special focus on homogeneity, in [16] using a nano-fluid jacket; liquid cooling is discussed in [19], [20], [5] and [14], but none seem to exploit the huge difference between radial and axial thermal conductivity of cells, explained in section 4.2.

Even if they are aware of the characteristic, the technical problem of cooling the very spots used also for electrical connection seems to be not dealt with yet.

To cite a currently widespread solution, Tesla cools down battery packs with a wavy flat duct, carrying liquid through the cells and exploiting a portion of the lateral surface of the 18650 cells [3].

Some other methods are much more sophisticated (and of complicate adaptation to a huge amount of cells in a narrow space), like the one described in [4], using a pressurized ammonia bath.

An interesting investigation can be found in [11], where some cells are cooled with a nanofluid consisting of a mixture of distilled water and aluminum oxide.

4.2 18650 thermal properties

An embryonic lithium cell can be described as a sandwich of four elements: anode, cathode, a separator, and the electrolyte drenching the whole. This structure can be arranged as a plane or rolled into a compact spiral (figure 4.1).

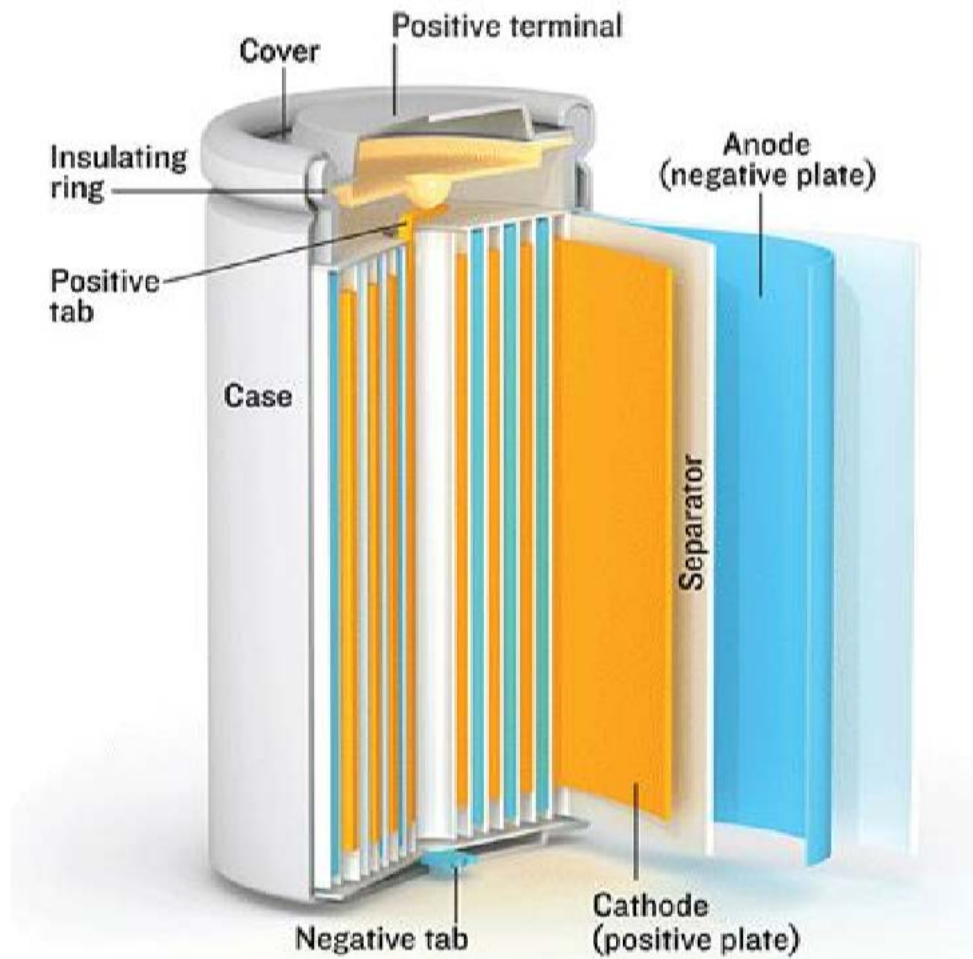


Figure 4.1: Internal structure of a common 18650 lithium cell

A very important property of a lithium cell, from the thermal point of view, is the difference between in-plane and cross-plane thermal conductivity. Cross-plane conduction, it being in a direction orthogonal to the sheets composing the sandwich, is penalized by the high number of different layers with their interface thermal resistances.

In a cylindrical cell like the 18650 it means that the axial and tangential conductivity is much higher than the radial one.

S. J. Drake measured the thermal properties of a cylindrical lithium cell and highlighted that the **axial conductivity is about a hundred times the radial one**. [9]

This is the reason why the so-called ”**tab cooling**” is much more effective than draining heat only from the lateral surface.

A great uncertainty in the FEM modeling of a cell is the **positive tab structure**: the cavity and the presence of an emergency vent moves the real cell away from the uniform solid approximation.

For this reason, an experiment will be conducted and described in section 5.3, to sharpen the modeling.

4.3 Cooling configuration

As good engineering practice, the first attempt to solve the problem is as simple as possible.

For this reason, the initial idea was a forced air convection cooling, with heat sinks on cells’ tabs; this would have, however, forced to maintain some room between the cells stacks, to allow air to pass through.

In this configuration there would be space for only two stacks of cells, limiting their number at about 600.

Excluded the air cooling, **liquid cooling** has been considered: it allows to manage greater energy densities and to delocalize the air side of the heat transfer from the battery pack to the motorcycle frame (radiators), where more space and air flow is available.

This method allowed, although the original frame width had to be increased by a dozen of millimeters, to accommodate three battery stacks, reaching 1056 cells and therefore the design capacity.

Four thin cooling devices have been imagined between and aside the cells stacks, and they will be called battery cooling plates (BCP) from now on. The gap between the stacks is 5.4 mm for the central ones, and about 6 mm for the lateral ones, where however must take place also the pack retention elements.

The **thermal coupling between the cells and the heat sinks** is a problem of great importance.

Electrically insulating materials have generally very low thermal conductivity: a polymeric BCP would be both expensive to fabricate (in low quantities) and ineffective.

On the other side, materials with high thermal conductivity are also good electrical conductors.

It goes without saying that an electrically conductive heat sink cannot be directly in contact with the cells’ connections.

For these reasons, a 0.5mm **thermal pad layer** will separate the metallic heat sinks from the connecting plates, isolating it electrically and, as far as possible, coupling them thermally (see figure 4.3 for clarity).

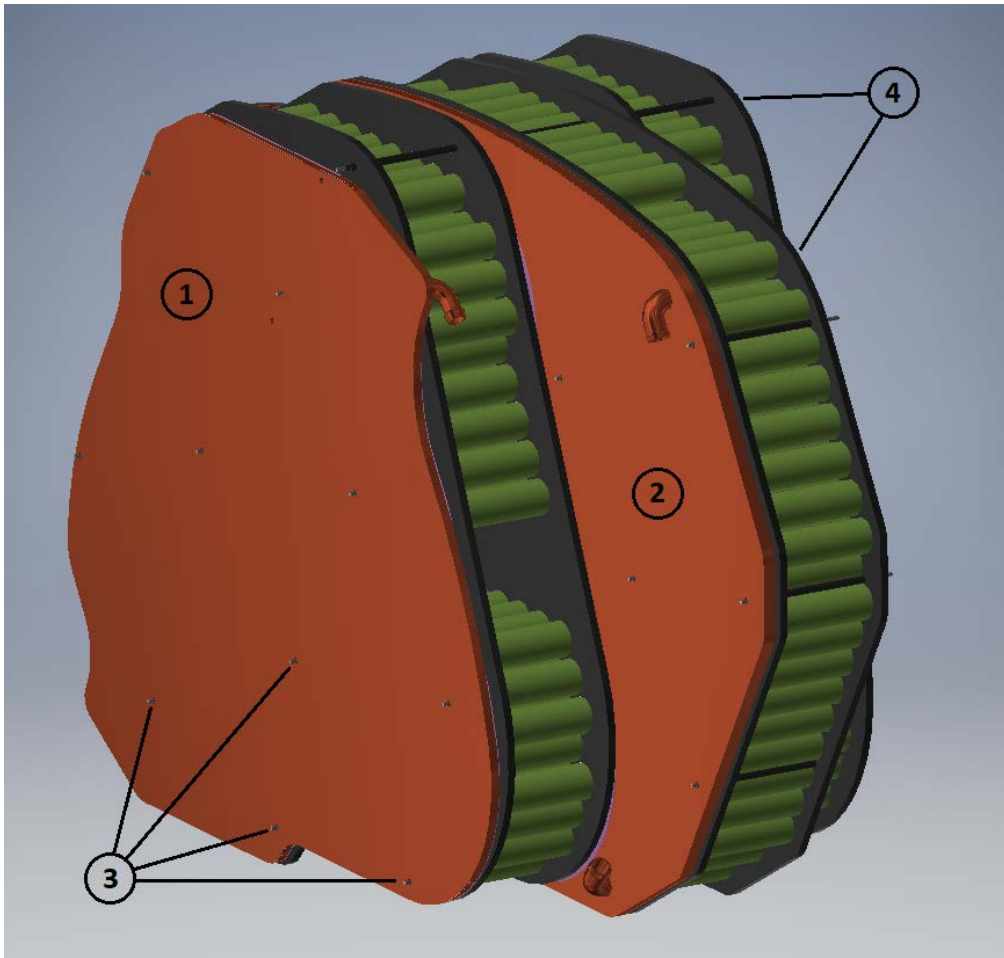


Figure 4.2: An overview of the battery pack, with its cells holder structures (4) and the two BCPs: the bigger one or "central" (2) and the external, or "lateral" (1). The 15 tie-rods (3) are also visible

A matrix of tie-rods, conveniently placed, could compress the pack in the cells axis direction, in order to squeeze the soft thermal pads (originally thicker than 0.5mm) in their gap.

This would assure a good thermal coupling between the surfaces and compensate for the un-flatness .

As mentioned, however, the contact between the electric plates and the BCP must be avoided at all costs: a set of polymeric spacers could be distributed in the area (and/or implemented in the cells holder structure) to prevent the catastrophic event.

The chosen refrigerant is simple **distilled water**.

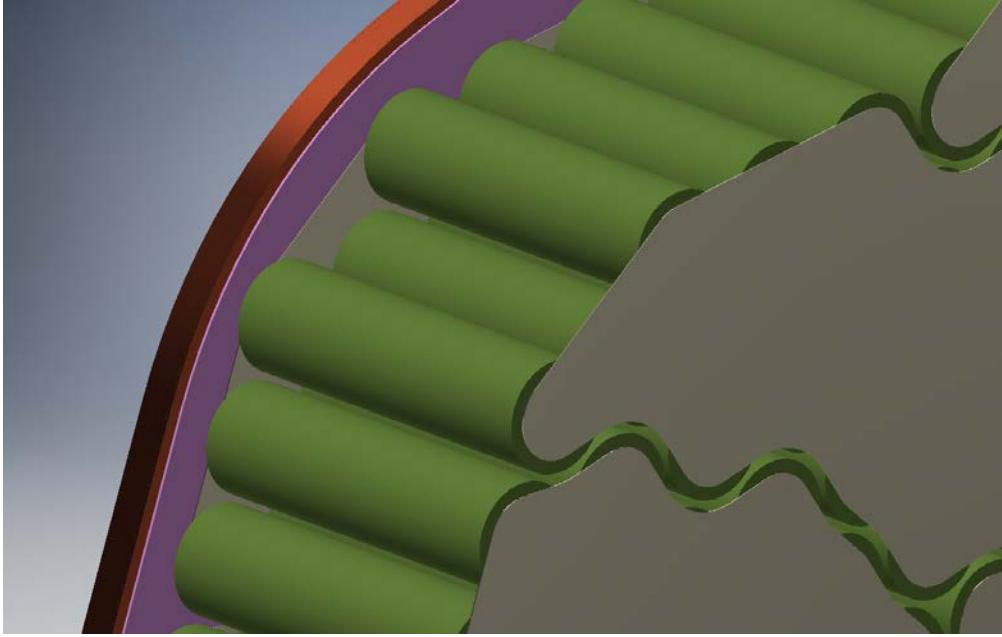


Figure 4.3: The thermal pad layer is represented in purple

4.4 Cooling homogeneity

Looking sideways at a BCP, it appears as a plane to which is applied, in the first approximation, a distributed constant heat flow.

Given the heat that must be extracted, the incompressible fluid flow rate and characteristics, the temperature difference between inlet and outlet is independent from the fluid path, as equation 4.1 states (\dot{m} is the mass flow and c_p the specific heat of the fluid).

$$\Delta T = \frac{Q}{c_p \cdot \dot{m}} \quad (4.1)$$

So the cells near the outlet will be hotter than those near the inlet.

Although the present thesis will never consider the air convection and radiation, inside and outside the pack, as significant, it is undeniable that their effect will be present (the battery pack case will have some vents, to promote a minimal air exchange inside the pack).

Liquid cooling and any kind of forced air convection among the cells aside, it is intuitive that a pack of cells **passively dissipate heat on the outside surface**, so the pack will have its **hotter spot near its center of mass**.

In other words, the passive cooling mechanisms promote a hot pack core and a cool pack surface.

These considerations suggest that the optimal spot to place the fluid inlets is near the mass center of the stacks, so that the **active and passive cooling mechanisms act in opposite direction, partially compensating each other's gradient**.

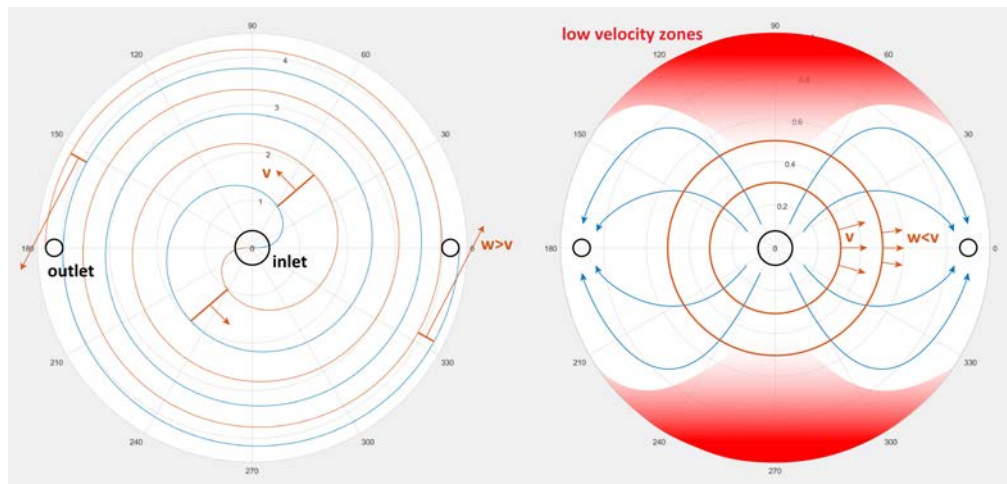


Figure 4.4: Comparison between spiralitic (left) and radial (right) flow: the same cooling plate, with an inlet and two outlets, is represented. In the left one there spiralitic channels. In orange are shown the flow sections at some points; it is clear that in the case without spirals the flow section rises (before the deviation is appreciable) with the distance from the inlet and therefore the velocity decreases, while in the left case the flow section decreases and the velocity increases. While guiding the flow and avoid low velocity zones (in red), controlling the spirals pitch means controlling the fluid speed and therefore the heat transfer coefficient; a comparison between numerical simulations with and without spirals is available in section 8.5.3

Then, a **problem arises: in a radial flow** the perimeter has a much lower velocity than near the central inlet, because the flow section increases with the distance from the inlet (i.e. radius).

As a workaround, a guided spiralitic flow has been adopted, moving some cells from the center of the lateral stack to make room for the inlets (the previous configuration is never represented here, figure 3.12 represents the ultimate cells arrangement).

This prevents the fluid to slow down, penalizing the thermal exchange: the channels formed by the spiralitic separators inside the BCP maintain a reasonably constant flow section and thus, flow velocity. In other words, the spiralitic channels add a tangential component to the flow velocity.

One central inlet per BCP, two spiral ducts for the lateral BCP and four for the central one have been shaped with spline curves (with just as many outlets).

The insertion of fins to increase the exchange area and the interruption of the spirals to promote radial leakage will be considered if the heat exchange obtained without them will be insufficient.

How to produce this kind of structures will be discussed in section 7.

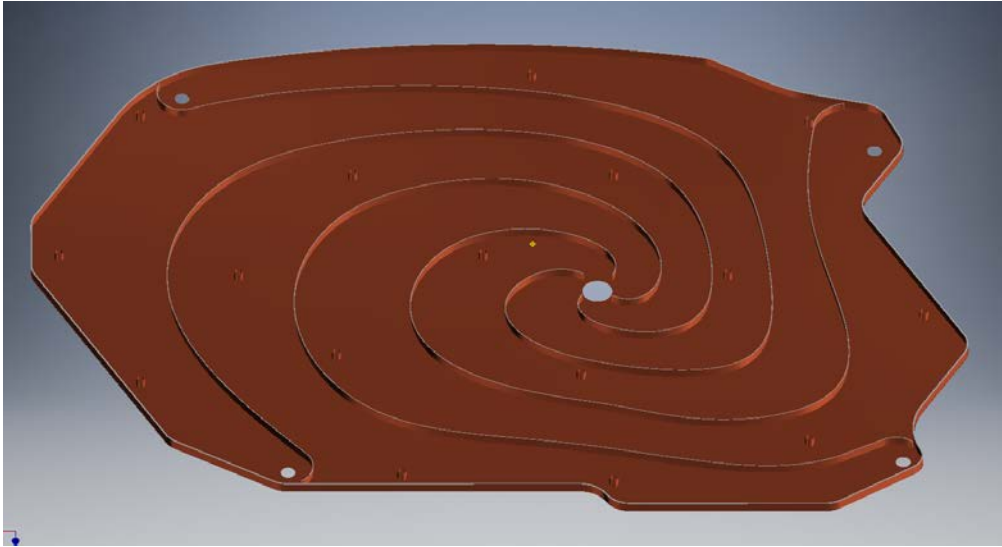


Figure 4.5: Central BCP internals, with central inlet and four perimetral outlets; since a central BCP provides cooling for both a central and a lateral stack, the inlet has been placed near the midpoint of a line linking central stack's center of mass and lateral stack's one.

Overall dimensions: 550x390x5.4 mm



Figure 4.6: Lateral BCP internals, with central inlet and two perimetral outlets.

Overall dimensions: 400x390x4 mm (the external wall is 1 mm thick, all the others are 0.5 mm)

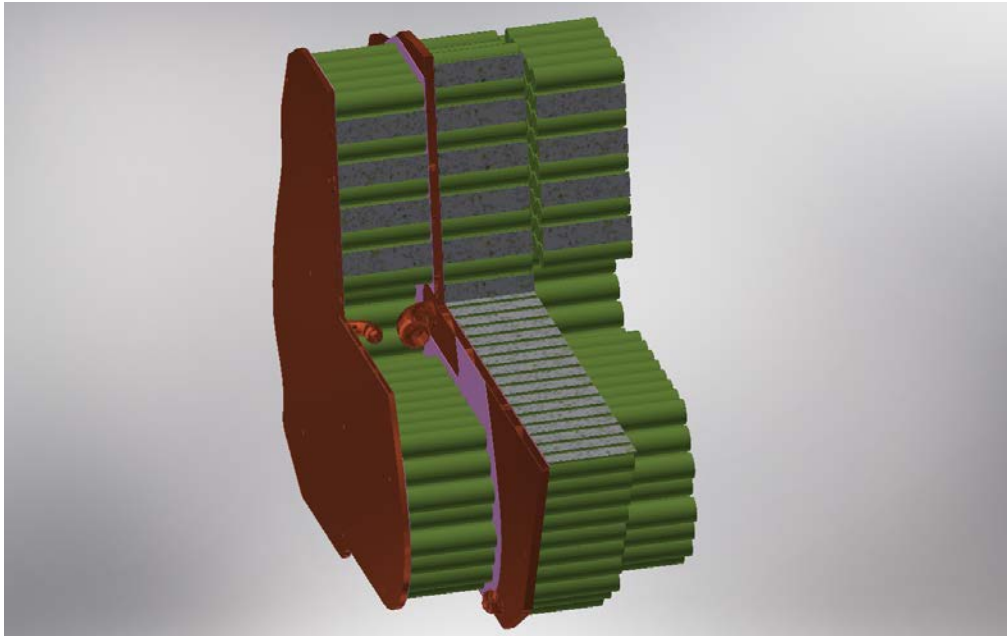


Figure 4.7: Detail section of the inlets location.

Chapter 5

Parameters and precursory data

Let us list first the parameters of the refrigerant water and the materials used, then make some further considerations, computations and measures.

Cooling fluid: Water

- density $\rho = 998 \frac{kg}{m^3}$
- dynamic viscosity $\mu = 0.001 Pa \cdot s = 1 \text{ cP}$
- cinematic viscosity $\nu = 1.05 \cdot 10^{-6} \frac{m}{s}$
- thermal conductivity $\lambda_W = 0.6 \frac{W}{m \cdot K}$
- heat capacity $c_{pW} = 4180 \frac{J}{kg \cdot K}$

Thermal conductivity

- copper : $\lambda_C = 390 \frac{J}{m \cdot K}$
- steel : $\lambda_S = 50 \frac{J}{m \cdot K}$
- thermal pad : $\lambda_{TP} = 12 \frac{J}{m \cdot K}$
- cell [9] : $\lambda_{CA} = 30 \frac{J}{m \cdot K}$ axial/tangential ; $\lambda_{CR} = 0.20 \frac{J}{m \cdot K}$ radial

Other parameters

- number of central cells $N_{cc} = 484$
- number of lateral cells $N_{cl} = 286$
- total cells $N_{ct} = 1056$
- external air temperature $T_{air} = 40 \text{ }^\circ\text{C}$

The air temperature value is a worst-case scenario estimate of a hot summer track day.

5.1 Cells heat generation

The heat generated is ascribable to numerous factors: Joule effect and entropy change inside the cell in first approximation. [10]

The entropy change related term can be relevant in some situations and its evaluation is very sensitive to the cell's composition, temperature, state of charge (SoC) and other parameters.

Lacking the literature in studies on the specific cells used for this design, the author decided to consider only the Joule effect for this thesis and measure the actual heat produced by a cell during the further developments.

For clarity, some values are recalled here:

- cell internal resistance: $R_i = 40 \text{ m}\Omega$
- continuous current: $I_c = 95.9 \text{ A}$
- number of parallels N_{cp} : 11

Now, a little digression on the **operative conditions** must be made.

As stated previously, the motor is capable of 35 kW provided continuously, but also has a current limit due to its cooling system; since the torque is directly proportional to the current, this can be seen as a torque limit.

The motorbike does not have a gearbox, but a fixed transmission ratio: this way, below a certain motor angular speed, the motor would not drain 35 kW but would be controlled via pulse width modulation by the ESC.

For the same reason, below that speed the battery will not supply 35 kW. Firstly, the heat produced by the battery when supplying 35 kW to the power-train will be calculated, then the critical speed will be computed and its importance will be clarified during the feasibility study.

The current drained from a single cell is

$$I_1 = I_c / N_{cp} = 8.73 \text{ A}$$

The heat generated by a single cells is

$$Q_1 = R_i \cdot I_1^2 = 3.04 \text{ W}$$

Consequently, the heat generated by the central and lateral cells stacks are, respectively:

$$Q_C = 484 \cdot Q_1 = 1473 \text{ W} \quad \text{and} \quad Q_L = 286 \cdot Q_1 = 870 \text{ W}.$$

This value is computed using the cell's internal resistance at room temperature (i.e. about 25 °C).

Provided that, in most cases, internal resistance at 50-60 °C is lower than at room temperature [12], this estimate of the heat generation is probably conservative enough for the purpose.

A 18650 cell is 65 mm long and 18.4 mm in diameter, tho its volume is:

$$V_c = \pi \cdot 9.2^2 \cdot 65 = 17283.8 \text{ mm}^3 = 1.72838 \times 10^{-5} \text{ m}^3$$

And then, the internal heat generation to be used in the numerical simulation is:

$$H_{gen} = \frac{Q_1}{V_c} = 1.761 \times 10^5 \frac{W}{m^3}$$

Coming to the critical speed after which this heat is actually generated, we can compute the minimum angular velocity at which the motor can generate 35 kW:

$$\omega_{min} = P/T_{max} = 35000 \text{ W}/50 \text{ Nm} = 700 \text{ rad/s} = 6685 \text{ rpm}$$

and then, through the transmission ratio $t_r = 13/54$, the corresponding vehicle speed:

$$V_{min} = \omega_{min} \cdot t_r \cdot 2\pi r_p \cdot \frac{3.6e-3}{60} = 182 \text{ km/h}$$

Where $r_p = 300 \text{ mm}$ is the rear wheel rolling radius.

5.2 Connection plates heat generation

The electrical connection plates produce heat for **Joule effect**.

During the subdivision of cells in series and parallels, attention has been kept to their shape, in order to make them as wide as possible in the current direction, maximizing the conducting section and avoiding bottle necks.

Because of their shape and connection geometry, it is way too inaccurate to esteem their resistance with a simple calculation (see figure 3.12).

For this reason, **two plates have been electrically simulated** : a nearly square one (fig. 5.1) and a long one (fig. 5.2).

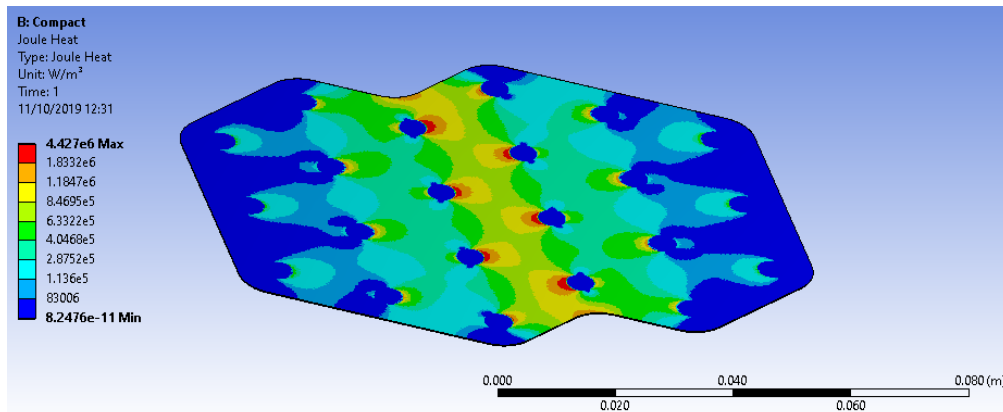


Figure 5.1: Electrical simulation of a compact plate; the Joule heat contour is shown

A 6mm diameter circular area has been divided, on the plate surface, to represent each cell soldering.

Eleven I_1 currents have been injected on the positive cells solderings, while

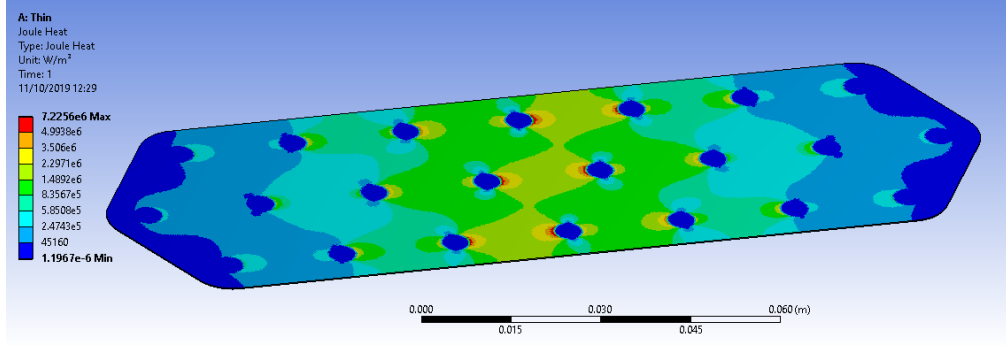


Figure 5.2: Electrical simulation of a long plate, never used in the real battery pack; the Joule heat contour is shown

ten I_1 currents have been extracted from ten of the negative cells solderings; null voltage has been set on the last negative soldering¹.

From these simulations, the average Joule heat generation rate returned:

- compact plate : $H_{min} = 2.96 \times 10^5 \text{ W/m}^3$
- long plate : $H_{max} = 5.99 \times 10^5 \text{ W/m}^3$

There are a total of 100 plates in the battery, and about 20 of them (overestimation) are similar to the long plate that has been simulated. An average value of heat generation density have been computed for the numeric simulation:

$$H_{AV} = \frac{80H_{min} + 20H_{max}}{100} = 3.57 \times 10^5 \text{ W/m}^3$$

The heat generated by all the three connection plates layers will now be calculated.

The volume of the plates can be easily obtained from the CAD model and the average plate volume amounts to about 1260 mm^3 .

The average heat generated by a single plate is therefore:

$$Q_{av_plate} = 1.260 \times 10^{-6} \text{ m}^3 \cdot H_{AV} = 0.449 \text{ W}$$

In the half battery model there are 23 plates on the central stack (sx side), 14 plates on the internal side of the lateral stack and 13 plates on the outer side.

The heat generated by the three layers are, approximately:

$$\begin{aligned} \text{lateral outer plates} \quad Q_{PLO} &= 13 \cdot Q_{av_plate} = 5.84 \text{ W} \\ \text{lateral inner plates} \quad Q_{PLI} &= 14 \cdot Q_{av_plate} = 6.29 \text{ W} \\ \text{central plates} \quad Q_{PC} &= 23 \cdot Q_{av_plate} = 10.33 \text{ W} \end{aligned}$$

We can now compute the **heat that the two BCPs must absorb**.

A central BCP must absorb the heat produced by half of the central cells, half of the cells of a lateral stack, the one produced by a central connection layer and the one from a inner electrical connection layer of a lateral stack:

¹The actual soldering area is wider on the negative tab, see section 5.3

$$Q_{BCP}^{central} = Q_C/2 + Q_L/2 + Q_{PLI} + Q_{PC} = 1188 \text{ W}$$

A lateral BCP must absorb the heat produced by half of a lateral stack and its outer electrical connection layer:

$$Q_{BCP}^{lateral} = Q_L/2 + Q_{PLO} = 441 \text{ W}$$

Initially, nickel-coated steel were considered to make these plates; the same heat generation evaluation was made and the result was more than 8 times greater.

As the reader can note, **copper electric plates contributes to the heat generation as much as the 1.38 %**.

5.3 Conduction calibration

The main uncertainty in this whole system is the thermal resistance between the inside of a cell and the BCP wall.

Indeed, there are many interfaces between metals and thermal pad, where the **interface resistance is unknown**; there is the interface between the conduction 0.2mm plates and the cell's tabs, for which the soldering technology is, to this day, undefined (probably spot-welding, desirably laser-welding); there is, in addition, the internal structure of the cell, varying from supplier to another and too complex to be modeled precisely in the main Computer Fluid Dynamics (CFD) simulation.

In particular, the **positive tab** of a 18650 cell appears, from the outside, as a flat circular button of about 7mm diameter; however, the region underneath presents some structures acting as **emergency gas vent** (Current Interruption Device, or CID) and **current limiter** (Positive Temperature Coefficient, or PTC), as shown in figure 5.3.

The negative tab is, in contrast, connected to the whole remainder of cell's case and, on the base of the cylinder opposite to the positive tab, offers nearly the whole 18mm diameter base for thermal contact.

In the geometric model the cells are a continuous volume; an interface resistance will be set between every cell and its electrical plate, with a value decided after a set of measures described below.

To calibrate the conduction resistance, the idea is to **measure the overall resistance** between the BCP wall (fluid side) and a point right behind the cell tab, inside the cell.

This would provide a value that includes the resistance of all layers, the resistances of the various interfaces and the thermal dynamics of the structure of the cell's tab.

To measure the resistance, **the temperature difference at the two ends must be logged, while a known heat flow passes through** the assembly; this is achieved producing a known heat right behind the cell's tab, isolating every other way for the heat to escape, and cooling the other end of the assembly.

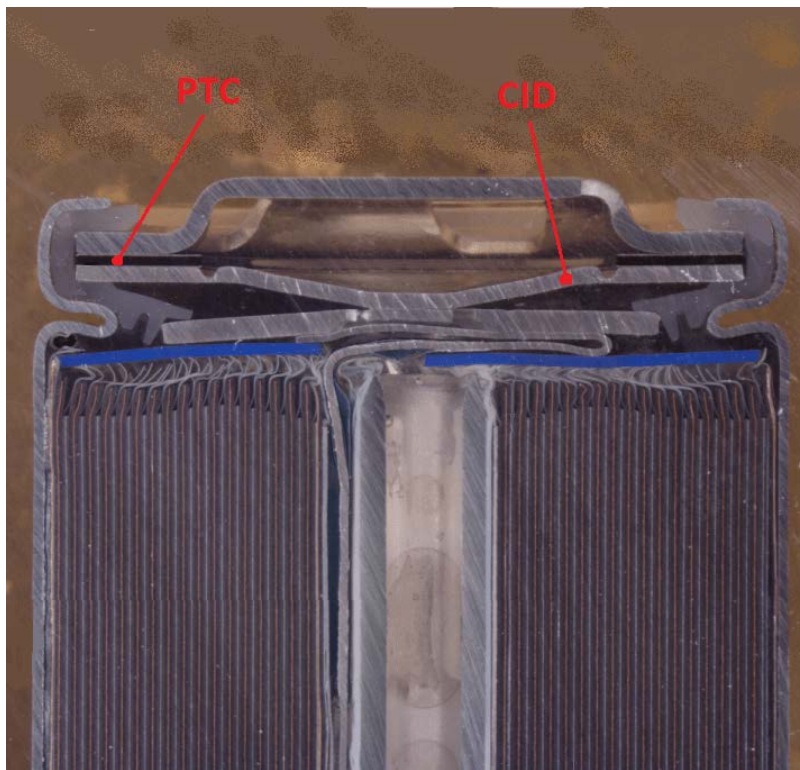


Figure 5.3: Example of positive tab structure of a 18650 cell

To do this, some cells have been disassembled, the positive and negative tabs cut and spot welded to the 0.2mm copper sheet (figure 5.4).



Figure 5.4: Positive (left) and negative (right) tabs, welded to the 0.2mm copper plate and with the K-thermocouple glued in position



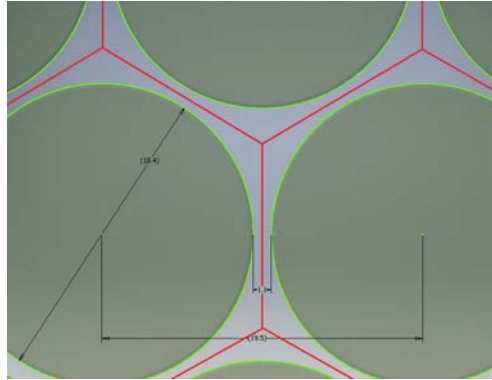
(a) The four resistors



(b) Resistors spreaded in thermal paste and taped, to provide electrical isolation from the case and prevent interferences with the measure



(c) The directional heating can, made from another cell's can and some mineral wool



(d) The shape of the conductive layers replicate the area associate to a single cell

Figure 5.5: Resistors used to produce heat and their mounting; a thermal pad disk have been placed in contact with the tab, and some thermal paste have been spread between the thermal pad and the resistors.

Four resistors (figure 5.5) have been used to produce heat, while voltage and current fed to them were logged to calculate the power.

The "cold" side of the assembly (figure 5.6) has been made out of a 0.5 mm copper plate, representing the BCP wall; a K-thermocouple has been soldered to the plate and the whole has been coupled to a passive heat exchanger with another thermal pad layer.

The thermal pad used has the same characteristics of the one modeled in the numerical simulation: 12 W/mK of thermal conductivity and 1mm in thickness; it is thicker than the 0.5 mm modeled because when pressure is applied, the thermal pad layer squeezes to 0.5-0.6 mm.

An adjustable switching-type power supply was used to power up the resistors, a home made logger wrote on a SD memory card the 8 thermocouples samplings, the voltage and the current fed to the resistors.

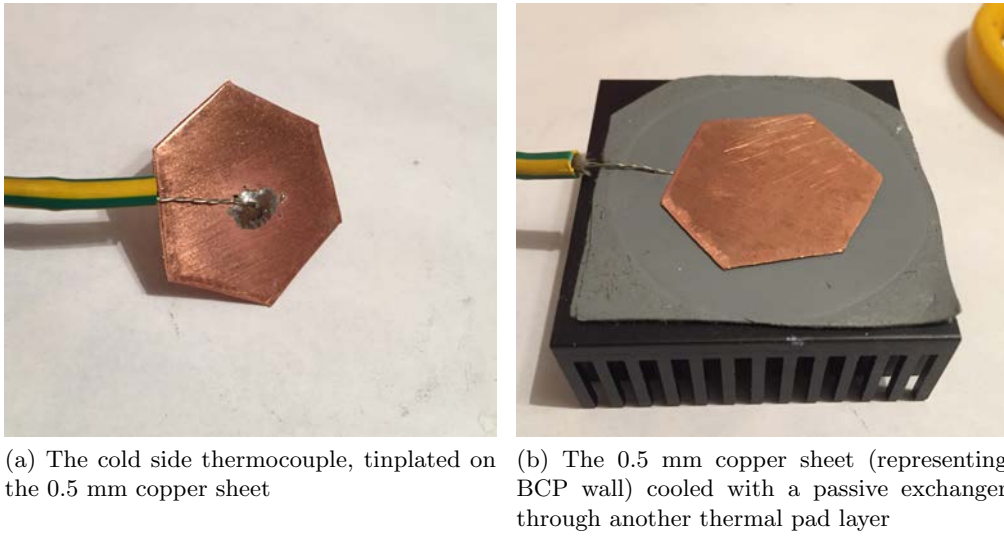


Figure 5.6: The cold side of the conduction measure

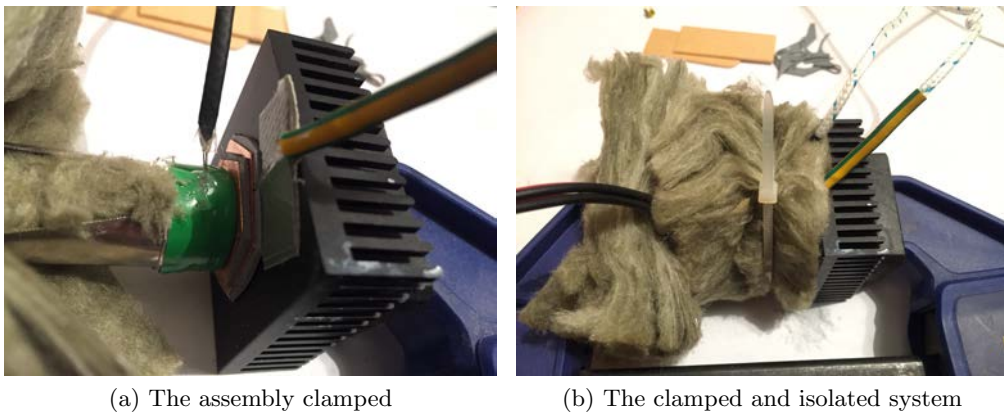


Figure 5.7: The final assembly is lightly pressed with a clamp and covered in mineral wool

The data analysis ended up in a graph like the one in figure 5.8; the temperatures and the heat produced are calculated as the mean during the steady phase (mean of the thermocouples) and the resistance is calculated as follows:

$$R = \frac{\Delta T_e}{Q_e} \quad \left[\frac{K}{W} \right] \quad (5.1)$$

where ΔT_e is the temperature difference between the two thermocouples and Q_e the power fed to the resistors.

The temperature logger has been compared with a Fluke-289 multimeter, a certified instrument, and the accuracy proved to be satisfactory (see appendix A).

Several measures have been taken, since the first results were not satisfac-

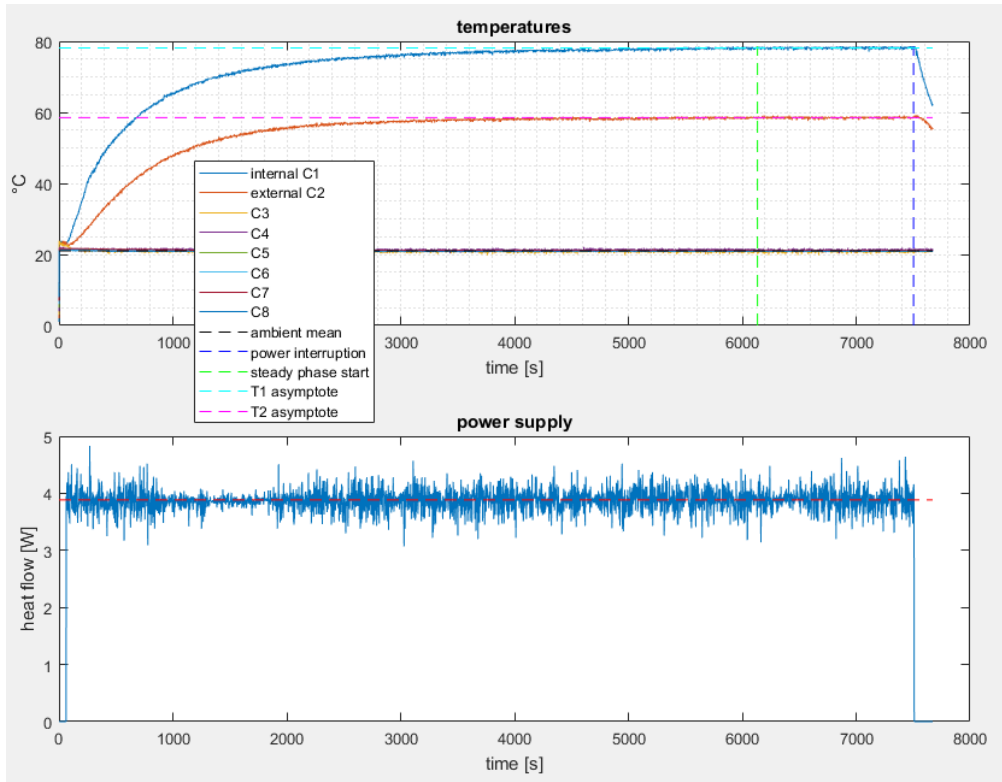


Figure 5.8: The graphs obtained analyzing the data logged during the experiment. Temperatures on the top graph, power to the resistors on the bottom. The blue vertical line is placed where the script detects the power interruption, the vertical green line is placed when the temperatures stabilized sufficiently; between them the system is considered steady and are computed the means of the thermocouples data.

tory: a first try with normally spot-welded tabs resulted in about 6 K/W for the negative tab, and about 12 K/W for the positive one.

Applying some tin paste between the 0.2mm plate and the tab reduced the resistance to **4 K/W for the negative tab** and to 10 for the positive, where the bottle necks were the air gaps in its structure.

Filling them with thermal paste dropped the **positive tab resistance to about 5 K/W**; however, investigating how the thermal paste affects the auto-discharge and the functionality of the emergency vent will be good practice.

Since in the CFD simulation the cells are symmetric, we have to obtain an equivalent resistance for both tabs.

The scheme in figure 5.9 represents four equivalent thermal representations of a cell; the cell has the two tabs for evacuating heat, so the two resistances have to be considered in parallel as follows:

$$R_P = 5 \text{ K/W} \quad R_N = 4 \text{ K/W}$$

$$\frac{1}{R_{eq}} = \frac{1}{R_P} + \frac{1}{R_N} \quad \rightarrow \quad R_{eq} = 2.22 \text{ K/W}$$

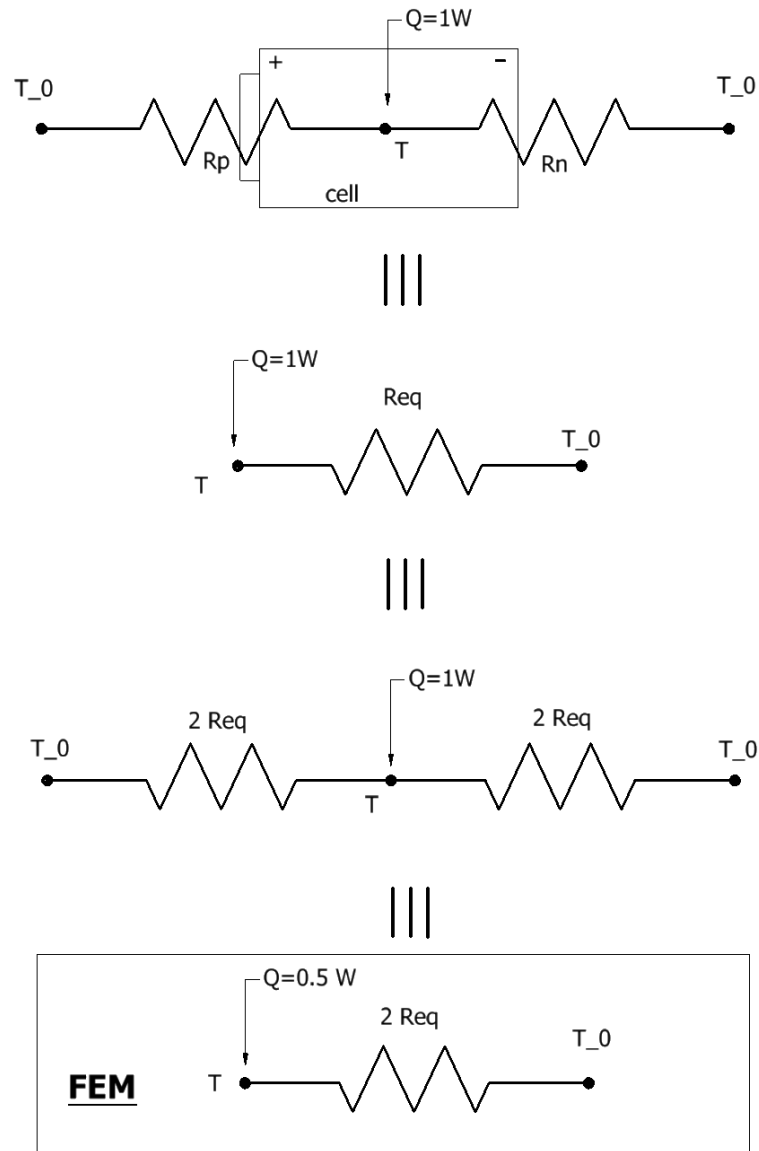


Figure 5.9: Equivalent schemes of conduction for a cell, neglecting air convection and radiation. The first from the top represents the real configuration, the second one is the simplification of the real configuration considering a single equivalent resistance, the third is a symmetric double-interface representation with the equivalent resistances and the third is the representation of the FEM model used to calibrate the interface resistance.

The **experiment** has been then **reproduced in a numerical simulation**, to calibrate an interface conduction leading to the same temperature difference observed experimentally.

A point placed 2 mm inside the cell, on its axis, has been chosen as equivalent to the thermocouple position in the experiment.

Between the two points there are four layers, the thickness and conductivity of which are summarized in table 5.1.

layer	thickness (s)	conductivity (λ)
BCP wall	0.5 mm	390 W/mK
thermal pad	0.5 mm	12 W/mK
electric plate	0.2 mm	390 W/mK
cell material	2 mm	30 W/mK

Table 5.1: Thermal conductive layers characteristics

Their resistance is, then:

$$R = \frac{1}{A} \cdot \sum \frac{s_i}{\lambda_i} = 0.414 \text{ K/W}$$

Where A is the area of the cell's section, having a diameter of 18.4 mm. Since the following equation applies:

$$2 \cdot R_{eq} = R_w + R$$

The **resistance due to the welding and all the interfaces** will be:

$$R_w = 2 \cdot R_{eq} - R = 4.03 \text{ K/W}$$

Then, the conductance to be imposed on the interface will be:

$$C_w = \frac{1}{A \cdot R_w} = 933 \frac{\text{W}}{\text{m}^2 \text{K}}$$

In figure 5.10 the result of the simulation of a single cell, where an **interface conductance of $900 \frac{\text{W}}{\text{m}^2 \text{K}}$ has been imposed between the cell and the electric plate**, can be appreciated; the conductance value has been slightly modified from the analytical solution C_w to meet the temperature difference measured experimentally.

In ANSYS Fluent, this boundary condition will be set up as a **fake wall**, with a prescribed thickness and material properties.

Thermal pads material has been chosen for the wall, and the necessary thickness is calculated as following:

$$t_w = \frac{\lambda_w}{C_w} = \frac{12 \frac{\text{W}}{\text{mK}}}{900 \frac{\text{W}}{\text{m}^2 \text{K}}} = 0.0133 \text{ M}$$

The difference between T_0 and the maximum temperature in the model is $\Delta T_{1W} = 3.14 \text{ }^\circ\text{C}$; remembering this has been obtained with a cell generating 1W (the FEM model actually represents a half of the cell, consequently generating 0.5 W), we can scale this result to the actual heat generation because of the linearity of the system:

$$\Delta T = \Delta T_{1W} \cdot Q_1 = 9.55 \text{ }^\circ\text{C}$$

Wall temperature $T_w = T_{max_cell} - \Delta T = 60 - 9.55 = 50.45 \text{ }^\circ\text{C}$

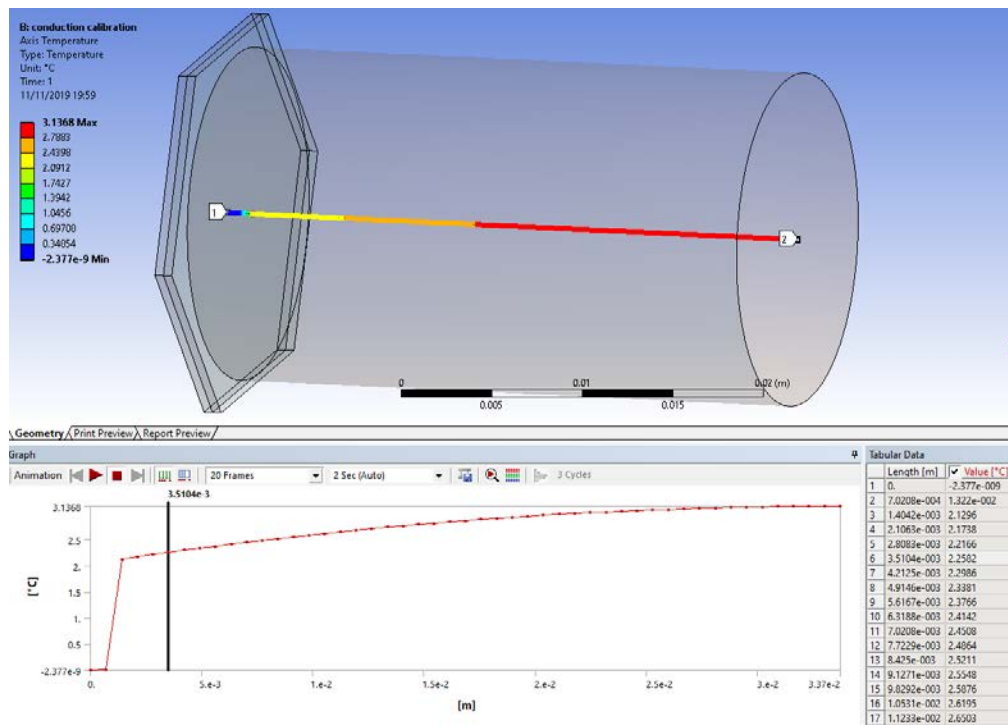


Figure 5.10: Conduction simulation of a single cell, reproducing the measure conditions. A $T_0 = 0 \text{ }^\circ\text{C}$ have been imposed on the surface of the the BCP wall and an internal heat generation rate (57858 W/m^3) have been imposed in the cell volume in order to generate 0.5 W from the half cell. The interface conductance have been modified to reproduce approximately $2.22 \text{ }^\circ\text{C}$ on the cell's axis, 2 mm from the interface inside the cell (3.2 mm from the fluid/BCP wall interface).

Chapter 6

Feasibility study

Before beginning a complex simulation like this, it is mandatory to verify, in a quick (accurate as possible) calculation, if the fluid system is most likely capable of the desired performance.

In addition, this analysis will provide the needed liquid flow rate to be imposed in the simulation.

For simplicity, the **BCPs will be analytically modeled as parallel straight channels**, with an imposed uniform heat flux.

Two parameters must be determined to simplify this study, one is the cell's internal resistance, directly determining the heat produced by the battery, and one is the vehicle speed, determining the air speed passing through the radiator and affecting its performance.

The first has been fixed, with an educated guess, in section 5.1 while the latter will be determined with some considerations in the following section.

6.1 Radiator performance

The air side of the cooling is now analyzed.

As the reader can see in figure 6.1, on the bike there are two radiators: a small triangular one for the group motor-driver (which can sustain higher temperatures than the battery) and a bigger one, occupying all the room available, dedicated to the battery.

Using a software, coded in Matlab and reported in appendix B, it is possible to **estimate the performance of motorsport radiators** [6] [15]. The one reported in the appendix was modified in order to calculate the steady state behaviour described in section 6.3, another version was used to plot the radiator performance varying the air speed and parametrizing the curves on hot water temperature and mass flow.(figure 6.2).

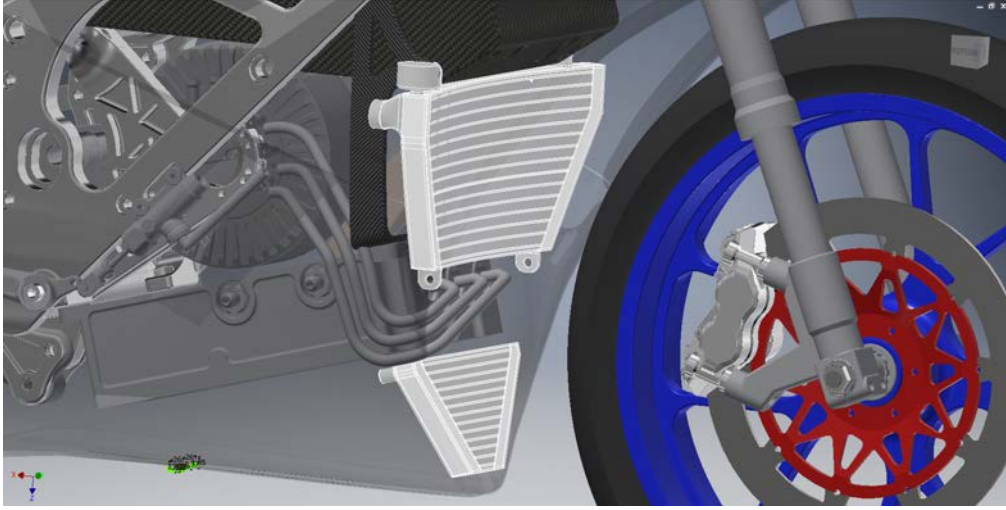


Figure 6.1: The two radiators on the bike; the top one is dedicated to the battery while the bottom one serves motor and regulator

The geometrical parameters used are the following.

- thickness $l = 20 \text{ mm}$
- multiport length (width) $lm = 290 \text{ mm}$
- multiport pitch $p = 10 \text{ mm}$
- multiport number $n = 15 \text{ mm}$
- total multiport thickness $s = 2 \text{ mm}$
- multiport wall thickness $sm = 0.27 \text{ mm}$

For simplicity, the thesis will proceed verifying the coupled radiator-battery system for a single vehicle speed value.

Since at low speed an electric fan can compensate for lack of air to the radiator and in the discontinuity zone the radiator performance is better than the plotted ones, **the check will be carried out at the critical speed** V_{min} computed in section 5.1, to assure proper system performance in all situations.

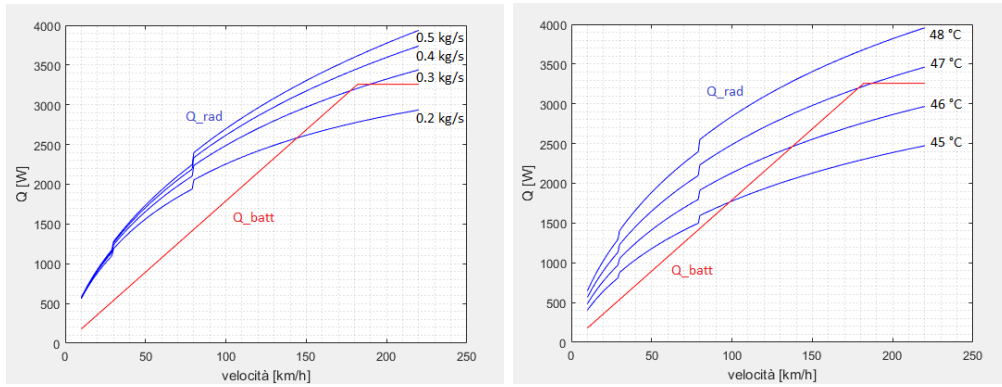
The version of the code reported in appendix B computes, iteratively, the temperature T_{cold} returned from the radiator to the battery (fig. 6.3).

The original software calculates the heat exchanged by the radiator provided the water mass flow \dot{m} , the air speed V and the radiator inlet temperature T_{hot} .

The iteration, conceptually not needed but used to avoid a deep rewriting of the code, uses the difference between the target heat exchange Q_{batt} and the heat actually exchanged by the radiator (Q_{rad}) to compute the value of T_{hot} for the next iteration:

$$T''_{hot} = T'_{hot} + \frac{Q_{batt} - Q_{rad}}{\dot{m}_T \cdot c_{pw}} \quad (6.1)$$

Where $\dot{m}_T = \dot{m}_C + \dot{m}_L$ is the sum of the volume flows to the two BCPs.



(a) radiator performance varying water flow (b) radiator performance varying hot water temperature

Figure 6.2: Radiator performance varying air speed; the heat exchanged by the radiator (Q_{rad}) in blue and the one produced by the battery (Q_{batt}) in red. The discontinuities are due to the step adjustment of the fins efficiency.

6.2 BCPs performance

The performance of the two BCPs are evaluated here with a quick analytical study.

The parameters describing the geometry of the BCPs' channels, partially obtained with measure tools in the CAD software, are collected in table 6.1.

Please note that the geometrical parameters are obtained from the first geometry design and not updated with the minor modifies successively suggested by the finite elements simulation.

Quantity	Central exch.	Lateral exch.
number of channels N_{ch}	4	2
spirals length $L_1, L_2 \dots$ [mm]	761, 750, 713, 747	1050, 1021
channel height h_{ch} [mm]	3	2.5
inlet diameter D_{in} [mm]	18	9
planar exchange area $A_{p_{exc}}$ [m^2]	0.3234	0.1055

Table 6.1: BCPs geometry data, from CAD model

Note that the diameter of the inlets is an initial guess.

The planar exchange area is equal, for the central BCP, to two times the area of a main face of the BCP wall, while it is not doubled for the lateral one, since it is in contact with the cells only on one side.

The channel height of the lateral BCP could have been reduced with respect to the first guess made to get higher fluid speeds and promote heat exchange; the component has, however, also a structural function: the tie-rods discharge their tension on its external surface and the BCP distribute

it on the entire pack, compressing the thermal pad layers. For this reason, reducing too much its thickness would reduce drastically the "sandwich effect", limiting its rigidity.

With the data obtained until now, table 6.2 summarize the procedure to compute the performance of the two types of BCPs in the battery pack.

Quantity	Formula	Central exch.	Lateral exch.	Unit
L_{av}	$\frac{\sum^N L_n}{N}$	0.743	1.04	m
W_{ch}	$\frac{A_{p_{exc}}^*}{N_{ch} \cdot L_{av}}$	0.0544	0.0509	m
P_{wet}	$2(h_{ch} + W_{ch})$	0.1149	0.1069	m
A_f	$h_{ch} \cdot W_{ch}$	1.633×10^{-4}	1.274×10^{-4}	m^2
D_h	$4A_f/P_{wet}$	5.687×10^{-3}	4.766×10^{-3}	m
A_{in}	$\pi D_{in}^2/4$	2.545×10^{-4}	6.362×10^{-5}	m^2
\dot{m}	parameter	0.1393	0.07620	kg/s
v_{in}	\dot{m}/A_{in}	0.5474	1.198	m/s
D_{out}	$\sqrt{4A_{in}/\pi N_{ch}}$	9	6.4	mm
S_f	$N_{ch} \cdot A_f$	6.531×10^{-4}	2.547×10^{-4}	m^2
v_{av}	\dot{m}/S_f	0.2133	0.2992	m/s
Re	$\frac{\rho v_{av} D_h}{\mu}$	1213	1426	-
Pr	$\mu c_{pW}/\lambda_W$	6.967	6.967	-
Gz	$\frac{Re Pr D_h}{L_{av}}$	64.69	45.72	-
T_{cold}	parameter	44.76	44.76	$^{\circ}C$
T_{out}	$T_{cold} + \frac{Q}{\dot{m} c_{pW}}$	46.80	46.14	$^{\circ}C$
ΔT	$T_w - \frac{T_{out} + T_{cold}}{2}$	4.665	4.993	$^{\circ}C$
Nu	$1.86 \left(\frac{Re Pr D_h}{L_{av}} \right)^{\frac{1}{3}}$	7.467	6.651	-
α	$Nu \lambda_W / D_h$	787.8	837.3	$\frac{W}{m^2 K}$
Q	$\alpha A_{p_{exc}} \Delta T$	1188	441.0	W
f	$\frac{64}{Re}$	0.05277	0.04489	-
Δp	$f \cdot \frac{L_{av}}{D_h} \cdot \rho \cdot \frac{v_{av}^2}{2}$	156.8	436.4	Pa

Table 6.2: BCP performance study for thermal behaviour of simplified BCP, calculating exchanged heat from the input of the mass flow \dot{m} and the the cold water temperature T_{cold}

The two parameters T_{cold} and \dot{m} are determined iteratively coupling the present procedure, originally programmed in Microsoft Excel, **with the radiator performance script** described in the previous section, as explained in section 6.3.

L_{av} is the average spiral length, that is the average length of the channel. W_{ch} is the average channel width and is computed so that, multiplied by the average length L_{av} , gives the lateral area of the BCP; since the exchange area is on both side for the central BCP and on one side for the lateral one, Ap_{exc}^* is equal to $Ap_{exc}/2$ for the central exchanger and to Ap_{exc} for the lateral one.

P_{wet} and A_f are the wet perimeter and the flow section for a single channel, respectively.

D_h is the hydraulic diameter.

A_{in} is the inlet section and v_{in} is the inlet velocity, ratio between mass flow rate (\dot{m}_C or \dot{m}_L) and the inlet section.

The flow rate value has been set in order to match the heat absorbed by the BCPs (output of this algorithm) with the one they must absorb: $Q_{BCP}^{central}$ and $Q_{BCP}^{lateral}$.

The outlet diameter D_{out} has been set in order to have se same total area for inlet and outlet.

S_f is the total average flow section available, and v_{av} is the fluid average velocity along the channels.

Re , Pr and Gz are, respectively, the Reynolds, Prandtl and Graetz numbers.

T_{out} is the theoric outlet temperature while ΔT is the average temperature difference between the center of the fluid flow and the wall.

Nu is the Nusselt number: the adopted formula is valid for laminar flows under the following conditions:

- $L_{av} < 2L_i = 2\frac{RePdD_h}{20}$
- $Gz > 10$
- $100 < Re < 2100$
- $0.48 < Pr < 16700$
- $\mu > 1 \text{ cP} = \mu_w$

α is the heat transfer coefficient and Q is the heat exchanged, slightly greater than the generated one.

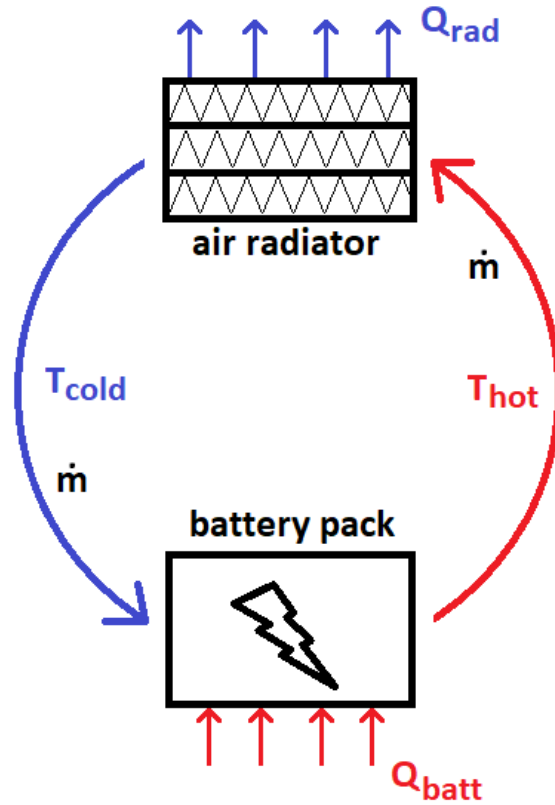
6.3 System steady state

Since the software for the radiators was provided as a Matlab script, while the BCP performance study on the battery BCPs was set up in Microsoft Excel, the coupling between the two systems has been made manually in order to save time.

As figure 6.3 schematize, the two systems have in common the fluid mass flow \dot{m} and the two temperatures T_{cold} and T_{hot} : the latter is an input of the Matlab script on the radiator performance, T_{cold} is an input in the BCPs performance study while \dot{m} is, formerly, an input in both.

In figure 6.4 is represented the **iterative method used to couple the**

Figure 6.3: Radiator-battery system scheme; the battery generates the heat Q_{batt} increasing the temperature of the water mass flow \dot{m} , the opposite happens in the radiator, exchanging the heat Q_{rad} with ambient air, equal to Q_{batt} when the system is in a steady state.



two systems: the BCPs performance study, provided a guess for the water temperature T_{cold} at the inlets, returns the mass flow \dot{m} needed to achieve the desired heat transfer; however, the computation was not originally set up in this way and \dot{m} must be adjusted manually until the heat exchanged, real output of the algorithm, matches the one produced by the cells.

Then \dot{m} is inserted in the Matlab script simulating the radiator and it, provided the velocity of the air V , iterates T_{hot} (as explained in section 6.1) until the heat exchanged Q_{rad} matches the one produced by the battery Q_{batt} .

At this point the the cold temperature for the next iteration can be computed as:

$$T_{cold} = T_{hot} - \frac{Q_{rad}}{\dot{m} \cdot c_{pw}} \quad (6.2)$$

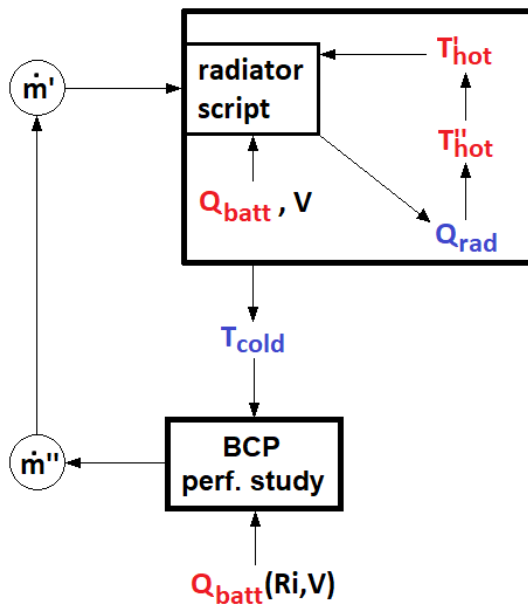


Figure 6.4: Radiator-battery **coupling iteration scheme**.

The radiator script has been included in a *while* cycle to compute iteratively (eq. 6.1) the temperature T_{hot} until Q_{rad} and Q_{batt} match. To do so the script must be provided with the mass flow \dot{m} , computed with the procedure of table 6.2 in turn needing T_{cold} (obtained from T_{hot} through 6.2) as an input.

Chapter 7

Exchangers manufacturing

The manufacturing of the heat BCPs is somehow a technical challenge. Their very low thickness-to-perimeter ratio and the thin spirals makes them very difficult and expensive to be machined from solid: most CNC machines would also require special tools to fix them to the vice. The materials considered are aluminum and copper.

The considered method for the construction is brazing; this method would require a template made from, for example, a 5-10mm aluminum plate, and a method to restrain the spirals in position; a proposal is represented in fig. 7.1.

On this plate would be machined two patterns: the holes, in tie-rods position, in which \varnothing 3.5 mm pins would be inserted, and the spirals shapes in the form of 0.55 mm thick caves, 1-2mm deep.

Firstly, the two 0.5 mm walls would be cut and drilled from a sheet; then the spirals can be manually bent, following the caves in the template, to respect as much as possible the original design.

The soldering would be operated mostly in an oven, in the following steps:

1. Place the first wall on the template, matching the holes with the pins
2. Place weld metal (sheet or paste) with pickling substance on the wall sheet
3. place tie-rods collars on the template's pins and the spirals, fixed in position with the clamps
4. place the second wall with its weld metal
5. plate a distributed weight on the second wall
6. bake the whole
7. extract and weld, manually, the perimetral stripe closing the BCP

In this procedure, the material with which the BCPs are made plays a fundamental role: while aluminum requires high temperatures (~ 600 °C) and a particular atmosphere to prevent oxidation, copper can be soldered with tin at 250-300 °C with pickling paste.

Copper have higher thermal conductivity than aluminum (390 vs $290 \frac{W}{mK}$) and would be better for thermal performance, although its weight would be more than three times higher.

For the the numerical simulation **copper BCP will be used**, because of the advantages in performance and easier construction.

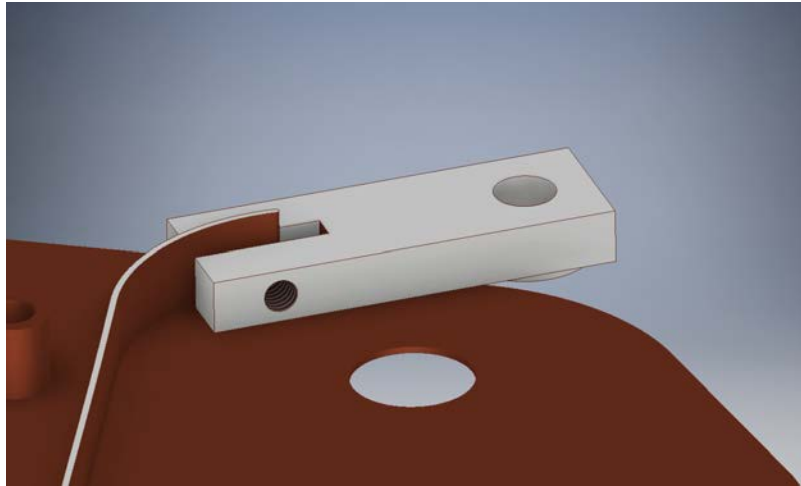


Figure 7.1: Proposal for a clamping device able to restrain the spirals in position; the clamp would be screwed to the template and a lateral screw would clamp the spiral tip.

Chapter 8

Numerical simulation

All the simulations have been carried out with Ansys 19.0 suite.
If an option is not cited, it must be intended with the default setting.

8.1 Objectives of the simulation

The reached configuration is quite complex from the fluid-dynamics and thermal point of view.

The symmetry of the entire pack has been exploited and the geometric model contains only the left side.

The simulation will provide:

1. The **maximum temperature** reached by the cells.
2. The difference between the hotter cell's core and the colder one, index of the **cooling homogeneity**: The complete mesh of the pack allows to inspect the interaction between the two BCPs, and the 3D mesh of the conductive layers (instead of a thin-wall mesh) will take into account the heat spread in every direction.
3. Streamlined to optimize the **flow** inside the BCPs: the geometry of the spirals and the positioning of the tie-rods could generate whirlpools and near-zero velocity zones, they will be modified and re-simulated until a satisfactory flow is obtained.
4. The **pressure drops** in the two BCPs : the design of the remainder hydraulic circuit (pipes, pack connector, pump...) depends on them.
5. The **disequilibrium in multiple outlets flow**, controlled only by the pressure loss in the channels: in the final pack, throttle valves will be placed on every outlet to calibrate the channels.
6. The comparison between the BCP performance with and without the spiralitic channels.

8.2 Geometry simplifications

In order to simplify the mesh generation, some geometrical features of the CAD model have been suppressed and some bodies have been neglected. In addition, trying to overcome some recurring problems caused, probably, by the high order splines defining the spirals, the geometry has been recreated in a second CAD software.

Since, after some simplifications later discussed, all bodies are extrudable, their profile have been exported from the original CAD software and imported in the new one, allowing to create the entire geometry with few functions.

The following figures with their captions will clarify the simplifications made and provide visual examples.

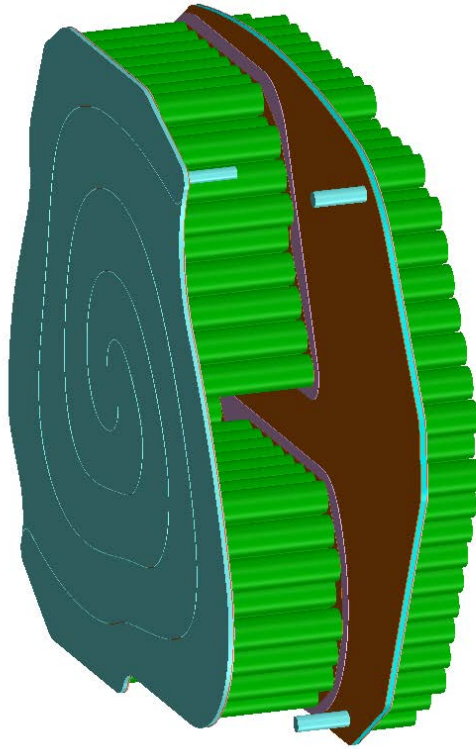


Figure 8.1: The symmetry of the pack has been exploited, cutting the right side. The symmetry plane is adiabatic unless specified, as every other surface. As the reader can see, the external wall of the lateral BCP has been suppressed.

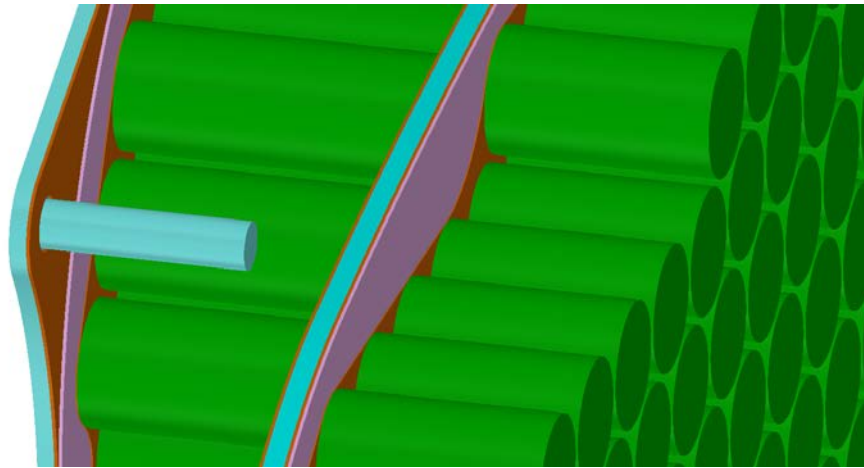


Figure 8.2: The cells are modeled as pure cylinders, the electrical plates have been modeled as a single layer and inlets/outlets as 10 mm straight ducts.

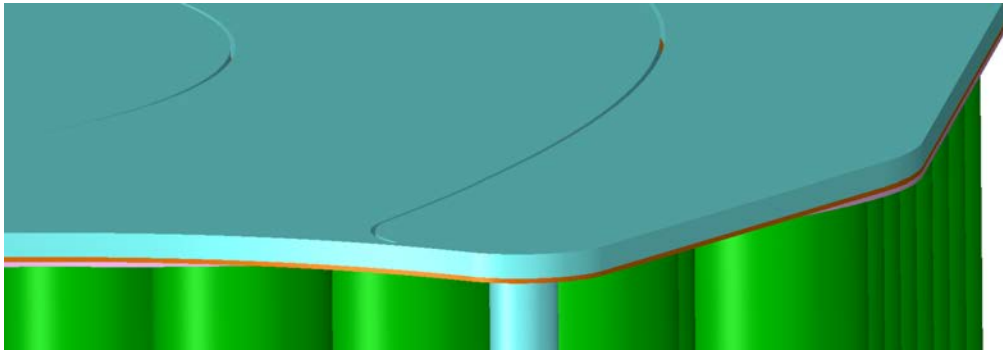


Figure 8.3: The BCPs have been deprived of the copper spirals, perimetral boundaries and tie-rods collars. The collars encumbrance, however, has been eliminated for the thermo-fluid simulation (in order to simplify the fluid mesh) but has been maintained for some precursory CFD simulation, in order to determine if their position was problematic from a streamline point of view; these simulations can be appreciated in section 8.5.1.

8.3 Meshing

First of all, a short discussion on the possibility to achieve a conformal mesh will be carried out, then the mesh setup and results will be described; in the end, some problems and errors encountered will be discussed.

The geometry, with the fluid domains, has been transferred to the meshing software as a STEP203.

The very first operation is, in the design modeler, setting the fluid bodies as fluids to be recognized by the solver and form the parts.

The parts have been grouped as following:

- **Central BCP** : contains the central fluid domain, the two BCP lateral walls and the inlet/outlets ducts.
- **Lateral BCP** : as above for the lateral BCP.
- **Central cells** : contains only the 484 central cells.
- **Lateral cells** : as above with the 286 lateral cells.
- **Lat-in plate + TP** : contains the right plate (representing all the electrical connection plates) and the thermal pad of the lateral stack.
- **Lat-out plate + TP** : as above for the left side of the lateral stack.
- **central plate + TP** : as above for the left side of the central stack.

Then, the SharedTopology (described in section 8.3.1) tool is created and generated¹.

8.3.1 Conformal mesh interruption

In a thermal and CFD simulation, a conformal mesh in the whole domain would be optimal.

A mesh is called conformal when, through an interface between two solids (eventually of different materials), every node on one side of the interface can be matched with a node on the other side with a very low tolerance; in other words, the mesh can be considered continuous through the interface. In contrast, in a non-conformal mesh the nodes on the two sides does not match, and the solver must interpolate the data from one side of the interface to transfer them to the nodes on the other side, increasing computational error.

To operate a conformal mesh between two different solids in Ansys Fluent, the *SharedTopology* tool of the *DesignModeler* must be used: this tool individuates the areas in common between two solids, eventually cuts out the contact region when of the two areas is larger, then deletes one of the duplicates so that there's a single interface area, shared between the two solids.

In this geometry every solid, apart from the cells, can be considered thin and can be extruded in the direction of the cells' axis (Y axis in the mesher).

A tetrahedral mesh in a thin body is not efficient: the method most adopted is the *Multizone* with prismatic elements: this method is more stable and adaptive than the *Sweep* and the result is very similar.

Following this logic, to obtain a completely conformal mesh we should start from one of the "layers" and expand in Y direction.

To clarify what layers means, starting from outside the lateral BCP we

¹Note that this tool operates only inside parts; interfaces between two solids belonging to different parts will not share the surface, and though the mesh will not be conformal through it

find, as layers, the BCP wall, the lateral fluid domains with the BCP internals, the inner wall, a thermal pad layer, a electrical plates layer, the lateral cells, other electrical plates, other thermal pad, the central BCP wall and so on.

Let's imagine we want to have a completely continuous mesh (and thus we have created a single part in the *DesignModeler*) and we start meshing the central cells: The cell's bases, in contact with the electrical plates and thus sharing the surface, will imprint their mesh on the plates.

Then we mesh the plates, the mesher will complete the mesh starting from the area shared with the cells; the plates will then imprint the mesh on the thermal pad and the thermal pad on the BCP wall.

Now the problem arises: the wall would be forced to respect the mesh pattern derived from the cells on one side, and the pattern of the spirals on the other, not matching; the same would happen if we start from the fluid domain toward the cells.

To overcome this obstacle, the cells' areas should be imprinted on the fluid domain or vice-versa; this workaround would be both very time consuming and complicate the mesher's job, not easy by itself.

The reader must remember that the final mesh presented here is the result of many trials and errors, since most meshing algorithm were unstable with this geometry, and every time consuming operation in the geometry preparation must be repeated every time the geometry was modified from the CAD software.

A more practical solution is to give up the completely conformal mesh and interrupt it somewhere.

After some attempts, the author decided to split the model in the different parts listed above, so that every **BCP wall / thermal pad interface is not conformal** (figure 8.9e).

In addition, also the **cells' mesh has been created non-conformal with the plates' one**: otherwise, the mesher failed.

8.3.2 Meshing methods, sizings and results

The final mesh counts about 16.5 millions elements and 50 millions nodes, the meshing duration is around 3 hours and the solver takes nearly 6 hours to perform 1000 iterations.

In this sections the meshing methods, sizings and result will be described, discussed and illustrated.

This mesh encounters the limits of the machine but the fluid's one is not fine (and smart) enough to make the continuity residual drop to $1e-3$; the high-order splines defining the spirals caused many problems to the meshing software and many options and prescription to the mesh, which could have generated a smarter discretization, failed to generate a successful mesh.

However, as section 8.6 will clarify, the results of the numerical simulation

can be considered valid for the purpose.

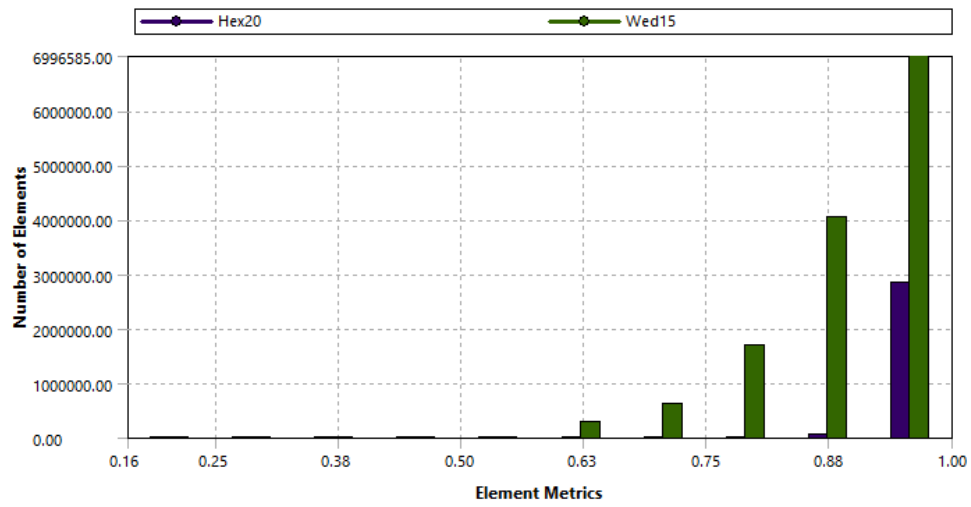


Figure 8.4: Mesh orthogonal quality chart

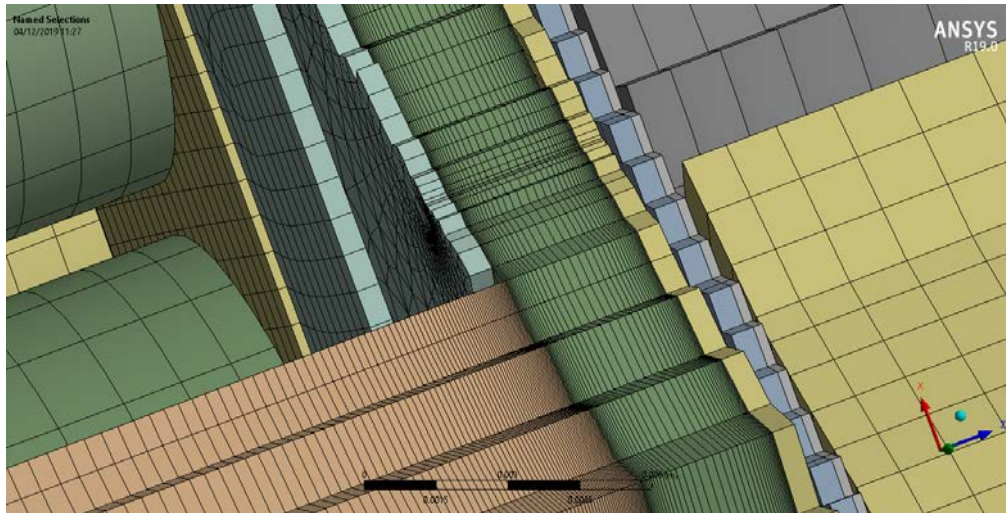


Figure 8.5: Inlets/outlets meshing detail; the inlets/outlets ducts have been refined toward the main fluid domains in order to mitigate the element transition. The BCPs walls have been separated from the ducts with a enlarging the hole, to avoid the *SharedTopology* between them.

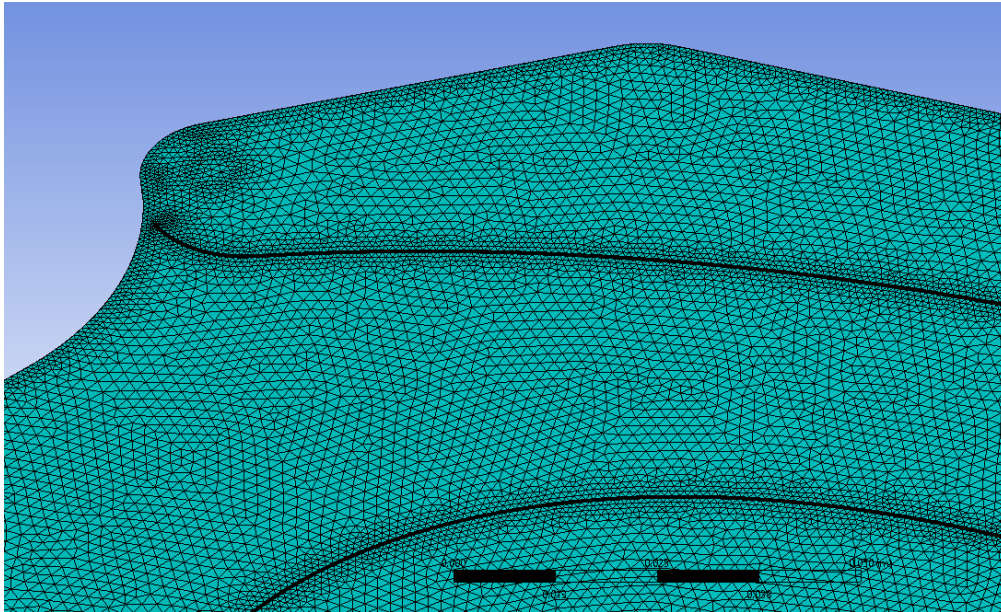


Figure 8.6: Mesh overview of the lateral fluid domain

Details of "Mesh"	
+ Display	
- Defaults	
Physics Preference	CFD
Solver Preference	Fluent
<input type="checkbox"/> Relevance	0
Export Format	Standard
Export Preview Surface Mesh	No
Element Order	Quadratic
- Sizing	
Size Function	Adaptive
Relevance Center	Fine
<input type="checkbox"/> Element Size	5.e-003 m
Mesh Defeaturing	Yes
<input type="checkbox"/> Defeature Size	Default
Transition	Slow
Initial Size Seed	Part
Span Angle Center	Fine
Bounding Box Diagonal	0.68840 m
Average Surface Area	1.5153e-003 m ²
Minimum Edge Length	3.7918e-005 m
- Quality	
Check Mesh Quality	Yes, Errors
<input type="checkbox"/> Target Skewness	Default (0.900000)
Smoothing	Medium
Mesh Metric	Orthogonal Quality

Figure 8.7:

General mesh settings :

Quadratic elements have been used, *orthogonal quality* has been chosen as mesh quality metrics since this is also the quality metrics in Fluent; inflation and assembly meshing were left with default settings.

Details of "cells method" - Method	
Scope	
Scoping Method	Named Selection
Named Selection	cells
Definition	
Suppressed	No
Method	MultiZone
Mapped Mesh Type	Hexa/Prism
Surface Mesh Method	Uniform
Free Mesh Type	Not Allowed
Element Order	Use Global Setting
Src/Trg Selection	Automatic
Source Scoping Method	Program Controlled
Source	Program Controlled
Sweep Size Behavior	Sweep Element Size
<input type="checkbox"/> Sweep Element Size	Default

(a) Cells mesh method

Details of "cell sizing" - Sizing	
Scope	
Definition	
Suppressed	No
Type	Element Size
<input type="checkbox"/> Element Size	2.5e-003 m

Details of "Inflation" - Inflation	
Scope	
Definition	
Suppressed	No
Boundary Scoping Method	Named Selections
Boundary	cells inflation bound...
Inflation Option	Total Thickness
<input type="checkbox"/> Number of Layers	3
<input type="checkbox"/> Growth Rate	1
<input type="checkbox"/> Maximum Thickness	4.e-003 m
Inflation Algorithm	Pre

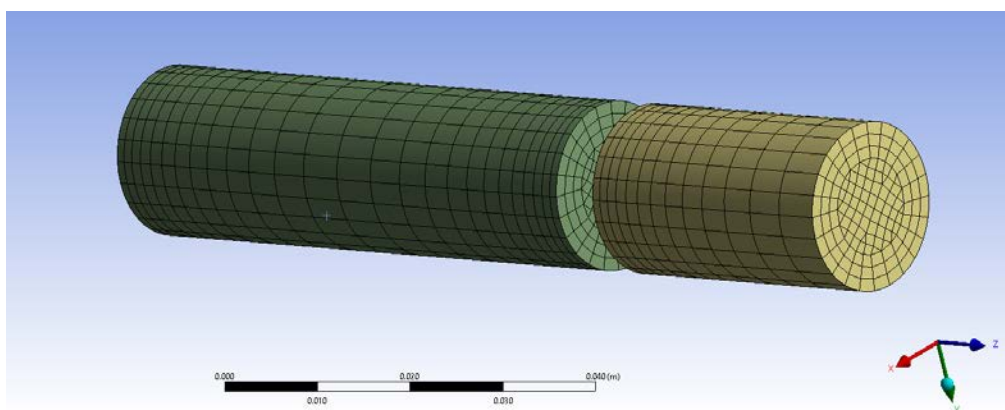
(b) Cells mesh sizing and inflation

Details of "Central cells bias" - Sizing	
Scope	
Definition	
Suppressed	No
Type	Number of Divisions
<input type="checkbox"/> Number of Divisions	13
Advanced	
Behavior	Soft
Bias Type	- - - - -
Bias Option	Bias Factor
<input type="checkbox"/> Bias Factor	5.0
Reverse Bias	No Selection

(c) Central cells bias

Details of "Lateral cells bias" - Sizing	
Scope	
Definition	
Suppressed	No
Type	Number of Divisions
<input type="checkbox"/> Number of Divisions	26
Advanced	
Behavior	Soft
Bias Type	- - - - -
Bias Option	Bias Factor
<input type="checkbox"/> Bias Factor	5.0

(d) Lateral cells bias



(e) Cells mesh

Figure 8.8: **Cells** : The cells are meshed with a *MultiZone* method with imposed non-free *hexa/prism* elements, together with an inflation prescription ; refining the mesh, from the center of the cell to the bases with a bias on their axis, reduced the number of elements for the cells' mesh.

Details of "Plates method" - Method	
+ Scope	
- Definition	
Suppressed	No
Method	Sweep
Element Order	Use Global Setting
Src/Trg Selection	Automatic Thin
Source	Program Controlled
Free Face Mesh Type	Quad/Tri
<input type="checkbox"/> Sweep Num Divs	1
Element Option	Solid
Constrain Boundary	No

(a) Plates mesh method

Details of "TP method" - Method	
+ Scope	
- Definition	
Suppressed	No
Method	Sweep
Element Order	Use Global Setting
Src/Trg Selection	Automatic Thin
Source	Program Controlled
Free Face Mesh Type	Quad/Tri
<input type="checkbox"/> Sweep Num Divs	1
Element Option	Solid
Constrain Boundary	No

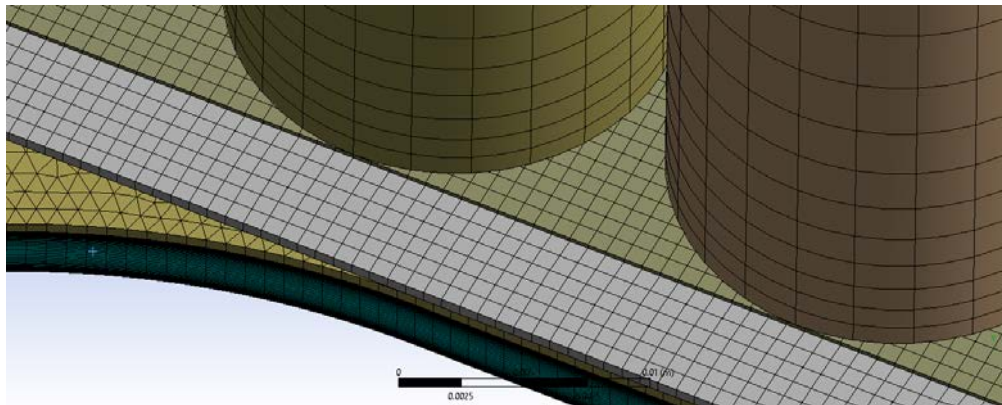
(b) Thermal pads mesh method

Details of "Plates Sizing" - Sizing	
+ Scope	
- Definition	
Suppressed	No
Type	Element Size
<input type="checkbox"/> Element Size	8.e-004 m
- Advanced	
<input type="checkbox"/> Defeature Size	Default
Behavior	Soft

(c) Plates mesh sizing

Details of "TP sizing" - Sizing	
+ Scope	
- Definition	
Suppressed	No
Type	Element Size
<input type="checkbox"/> Element Size	8.e-004 m
- Advanced	
<input type="checkbox"/> Defeature Size	Default
Behavior	Hard

(d) Thermal pads mesh sizing



(e) Electrical plates and thermal pads mesh

Figure 8.9: **Electrical plates and thermal pads** : meshed using the *sweep* method in *automatic thin* mode; the size is pretty fine to limit the interpolation error on the non-conformal interfaces with the cells and the BCPs walls.

Details of "Central fluid method" - Method	
+ Scope	
- Definition	
Suppressed	No
Method	MultiZone
Mapped Mesh Type	Prism
Surface Mesh Method	Pave
Free Mesh Type	Not Allowed
Element Order	Use Global Setting
Src/Trg Selection	Manual Source
Source Scoping Method	Named Selection
Source Named Selection	central fluid source
Sweep Size Behavior	Sweep Element Size
<input type="checkbox"/> Sweep Element Size	Default

(a) Central fluid method

Details of "Lateral fluid method" - Method	
+ Scope	
- Definition	
Suppressed	No
Method	MultiZone
Mapped Mesh Type	Prism
Surface Mesh Method	Pave
Free Mesh Type	Not Allowed
Element Order	Use Global Setting
Src/Trg Selection	Manual Source
Source Scoping Method	Named Selection
Source Named Selection	lateral fluid source
Sweep Size Behavior	Sweep Element Size
<input type="checkbox"/> Sweep Element Size	Default

(b) Lateral fluid method

Details of "Central fluid main sizing" - Sizing	
+ Scope	
- Definition	
Suppressed	No
Type	Element Size
<input type="checkbox"/> Element Size	1.8e-003 m

(c) Central fluid sizing

Details of "Lateral fluid main sizing" - Sizing	
+ Scope	
- Definition	
Suppressed	No
Type	Element Size
<input type="checkbox"/> Element Size	1.8e-003 m

(d) Lateral fluid sizing

Details of "fluid refinement" - Sizing	
+ Scope	
- Definition	
Suppressed	No
Type	Element Size
<input type="checkbox"/> Element Size	8.e-004 m

(e) Fluid refinement

Details of "spirals tips Sizing" - Sizing	
+ Scope	
- Definition	
Suppressed	No
Type	Element Size
<input type="checkbox"/> Element Size	1.e-004 m

(f) Spiral tips sizing

Details of "fluid thickness sizing" - Sizing	
+ Scope	
- Definition	
Suppressed	No
Type	Number of Divisions
<input type="checkbox"/> Number of Divisions	38
- Advanced	
Behavior	Soft
Bias Type	_ _ _ _ _
Bias Option	Bias Factor
<input type="checkbox"/> Bias Factor	10.0

(g) Fluid thickness bias

Details of "Exchanger walls method" - Method	
+ Scope	
- Definition	
Suppressed	No
Method	Sweep
Element Order	Use Global Setting
Src/Trg Selection	Automatic Thin
Source	Program Controlled
Free Face Mesh Type	Quad/Tri
<input type="checkbox"/> Sweep Num Divs	1
Element Option	Solid
Constrain Boundary	No

(h) Exchangers' walls mesh method

Figure 8.10: For **Fluid domains** meshing, although sweepable bodies, the *MultiZone* method came up to be a more reliable algorithm; *prism paved* surface mesh and a bias along thickness generated a sweep-like mesh, refined near the walls. (e) refines the fluid mesh near the perimetral boundaries, spirals and in/outlets regions, while (f) makes the round spirals tips sufficiently refined. For BCPs **walls** only an *automatic thin* method has been defined, since the sizing is entirely copied from the fluid domains. The result can be appreciated in figures 8.6 and 8.11

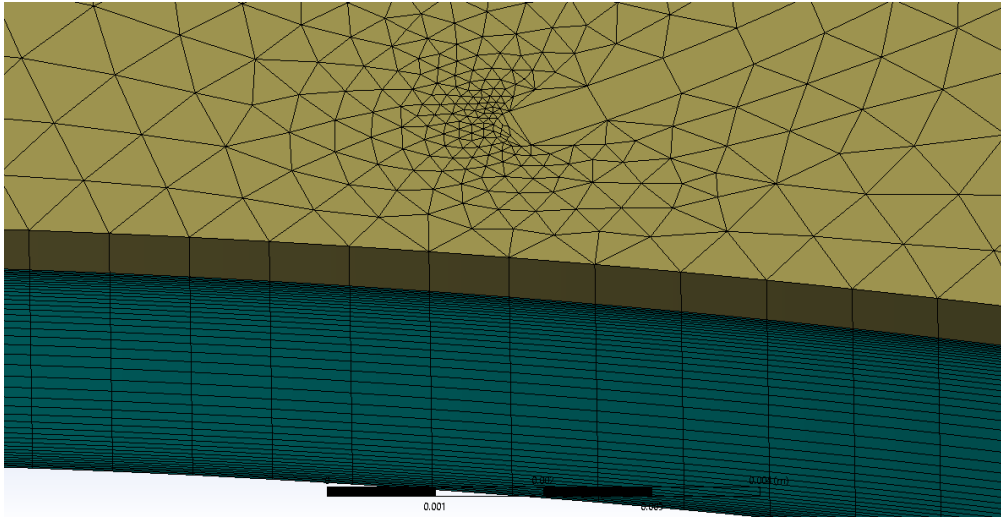
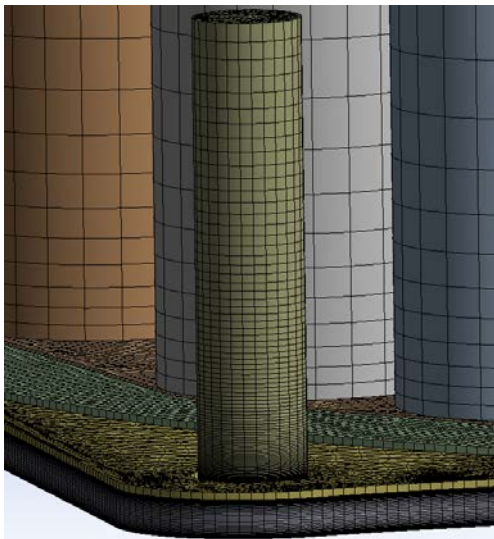


Figure 8.11: Detail of the refinement on the spirals' tips and fluid thickness bias; elements adjacent to the wall are 1.65×10^{-2} mm thick.



(a) Outlet mesh example

Details of "in/outlets method" - Method	
<input checked="" type="checkbox"/> Scope	
<input checked="" type="checkbox"/> Definition	
Suppressed	No
Method	Sweep
Element Order	Use Global Setting
Src/Trg Selection	Automatic
Source	Program Controlled
Target	Program Controlled
Free Face Mesh Type	Quad/Tri
Type	Number of Divisions
<input type="checkbox"/> Sweep Num Divs	100
Element Option	Solid
Constrain Boundary	No
<input checked="" type="checkbox"/> Advanced	
Sweep Bias Type	_____
<input type="checkbox"/> Sweep Bias	50.0

(b) in/outlets method settings

Figure 8.12: Meshing method for **in/outlets** ducts; base surfaces sizing is conformal with the fluid and the wall.

8.3.3 Meshing problems

The meshing process of this geometry has been very problematic. Frequent and inexplicable behaviour, like the one in figure 8.13, of the meshing software has been caused, probably, by the **high order splines** describing the spirals.

In particular, the meshing on the fluid domains became faulty when main sizing (8.10c and 8.10d) and refinement 8.10e were much different and/or requested finer than the values adopted.

Many attempts did not end up with a successful inflation mesh near perimeter and spirals.

A finer mesh was desirable near the inlets and outlets, since the flow in those region is turbulent because of the sudden deviations. This would, however requested to split the solid (path followed and abandoned because even more problems appeared) since the *MultiZone* method doesn't allow a *refinement* ANSYS command.

Creating a conformal mesh, between cells and plates, also demonstrated to be problematic: the cause was probably in a not optimal surface split by the CAD software.

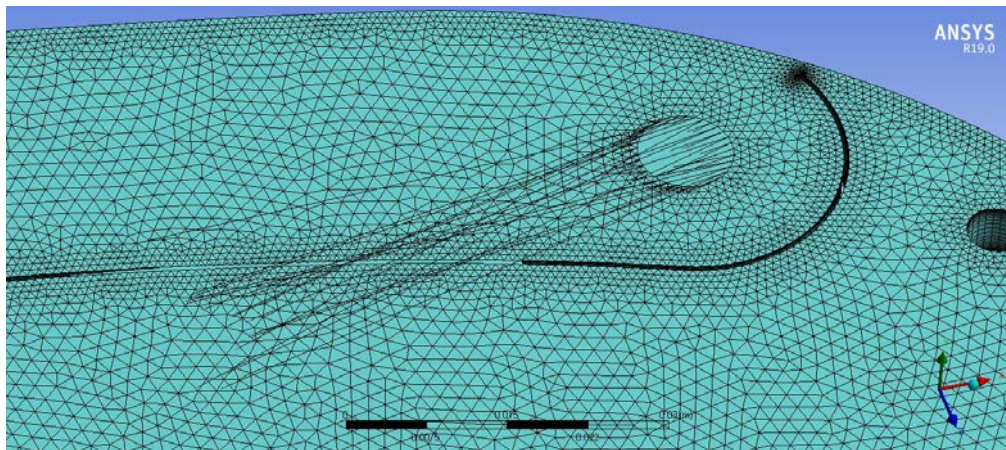


Figure 8.13: An example of an error in the meshing process.

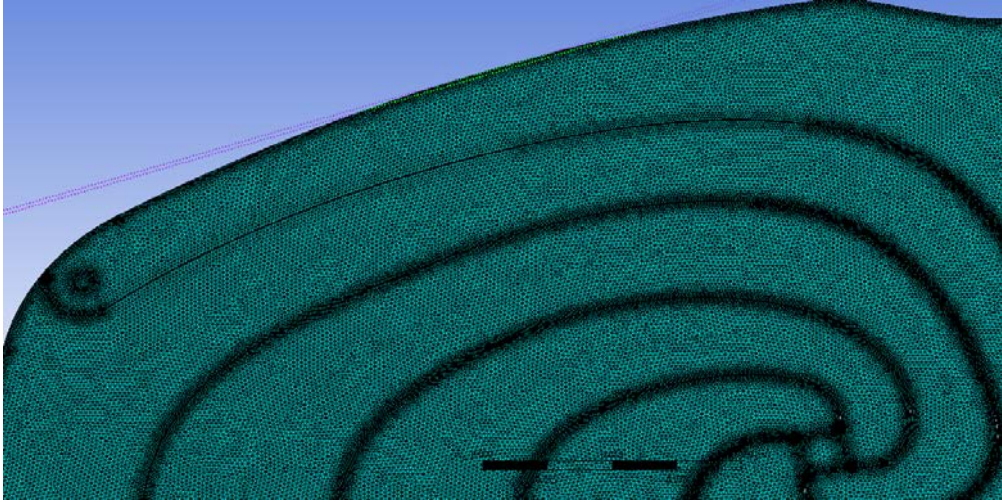


Figure 8.14: Even if the meshing of the central fluid domain was successful, some random areas presented odd behaviour: some spline sections were meshed coarser than the rest, some finer, even if they are a unique geometric line addressed with the refinement

8.4 Ansys Fluent

Firstly, the numerical models for the fluid dynamics and thermodynamics are reported, then follows an overview of the fluent options modified from default and the set-up of the simulation.

8.4.1 Mathematical models

The equation for conservation of mass, or **continuity equation**, can be written as follows:

$$\frac{\partial \rho}{\partial t} + \nabla \cdot (\rho \vec{v}) = S_m \quad (8.1)$$

The source S_m is the mass added to the continuous phase from the dispersed second phase (for example, due to vaporization of liquid droplets) and any user-defined sources.

The **equation for conservation of momentum** in an inertial (non-accelerating) reference frame can be written as follows:

$$\frac{\partial}{\partial t}(\rho \vec{v}) + \nabla \cdot (\rho \vec{v} \vec{v}) = -\nabla p + \nabla \cdot (\bar{\tau}) + \rho \vec{g} + \vec{F} \quad (8.2)$$

where p is the static pressure, $\bar{\tau}$ is the stress tensor (described below), and $\rho \vec{g}$ and \vec{F} are the gravitational body force and external body forces (for example, that arise from interaction with the dispersed phase), respectively. \vec{F} also contains other model-dependent source terms such as porous-media

and user-defined sources. The stress tensor $\bar{\tau}$ is given by

$$\bar{\tau} = \mu[(\nabla\vec{v} + \nabla\vec{v}^T) - \frac{2}{3}\nabla \cdot \vec{v}I] \quad (8.3)$$

where μ is the molecular viscosity, I is the unit tensor, and the second term on the right hand side is the effect of volume dilation.

ANSYS Fluent solves the **energy equation** in the following form:

$$\frac{\partial}{\partial t}(\rho E) + \nabla \cdot (\vec{v}(\rho E + p)) = \nabla \cdot (\lambda_{eff}\nabla T - \sum_j h_j \vec{J}_j + (\bar{\tau}_{eff} \cdot \vec{v})) + S_h \quad (8.4)$$

where k_{eff} is the effective conductivity and \vec{J}_j is the diffusion flux of species j .

S_h includes volumetric heat sources that you have defined but not the heat sources generated by finite-rate volumetric or surface reactions since species formation enthalpy is already included in the total enthalpy calculation.

Energy E is given by

$$E = h - \frac{p}{\rho} + \frac{v^2}{2} \quad (8.5)$$

where sensible enthalpy h is defined for incompressible flows as

$$h = \sum_j Y_j j_j + \frac{p}{\rho} \quad (8.6)$$

where Y_j is the mass fraction of species and

$$h_j = \int_{T_{ref}}^T c_{p,j} dT \quad (8.7)$$

The value used for T_{ref} in the sensible enthalpy calculation depends on the solver and models in use. For the pressure-based solver T_{ref} is 298.15 K except for PDF models in which case T_{ref} is a user input for the species. For the density-based solver T_{ref} is 0 K except when modeling species transport with reactions in which case T_{ref} is a user input for the species.

For the **thermal conduction dynamics**, the governing equation is given by

$$\frac{\partial}{\partial t}(\rho c_p T) = \nabla(\lambda \nabla T) + \frac{Q}{V} \quad (8.8)$$

where Q/V is the internal heat generation rate.

8.4.2 Setup

The following options have been modified from the default settings.

- General : steady state simulation
- Viscous model: **laminar** , energy equation activated
- Materials:
 - fluid domains and in/outlets: water-liquid from Fluent database
 - **cells : orthotropic thermal cond.** 0.20 W/m/K radial, 30 W/m/K axial
 - plates : thermal cond. 390 W/m/K isotropic
 - thermal pads: thermal cond. 12 W/m/K isotropic
 - BCPs: thermal cond. 390 W/m/K isotropic
- Zones conditions: (to every body the corresponding material has been assigned)
 - cells : 176100 W/m^3 internal heat generation (source term)
 - plates : 357000 W/m^3 internal heat generation (source term)
- Mesh interfaces: set all the interfaces as **coupled wall**².
- Boundary conditions: inlets have been set as *velocity inlets* and outlets as *pressure outlets*
 - central inlet : 0.5474 m/s @ 317.91 K
 - central outlets : 0 Pa @ 319.95 K
 - lateral inlet : 0.393 m/s @ 317.91 K
 - lateral outlets : 0 Pa @ 319.29 K
 - cells/plates interfaces : 0.0133 m thickness , thermal-pad material (see section 5.3)
- Report definitions:
 - volume average velocity in fluid domains
 - volume average temperature in cells

8.4.3 Solution convergence

The scaled residuals of the governing equations, especially the continuity one, remained high.

²This option is used to thermally couple the non-conformal interfaces between solids and to make them appear as *wall* entities, allowing to set the fake thickness and material in order to model an interface thermal resistance

Several weeks have been spent trying to obtain the better mesh possible but, as explained in section 8.3.3, the prescription of a smart mesh (refining near the walls, using inflation options etc.) often caused the mesher to fail.

However, as will be explained now, the results can be considered significant for the purpose and the reader should not be alarmed if a mesh-independence test has not been carried out, since it is clearly sub-optimal.

The volume-average velocity in the main fluid domains and the volume-average of the cells temperature have been monitored, during the simulation, to determine its convergence. The simulation has been stopped when these two quantities and the residuals stabilized, after about 500 iterations.

In addition, the mass flow conservation and the correspondence between the heat generated by the cells and the one transferred to the fluid have been verified as following:

The fluid flows, calculated by Fluent, at the inlets are:

- central inlet $\dot{m}_C^{in} = 0.13912 \text{ kg/s}$
- lateral inlet $\dot{m}_L^{in} = 0.075814 \text{ kg/s}$

The fluid flows, calculated by Fluent, at the outlets are:

- central outlets $\dot{m}_C^{out} = 0.13915 \text{ kg/s}$
- lateral outlets $\dot{m}_L^{out} = 0.075835 \text{ kg/s}$

The percentage error on the mass flows is, then:

- central $err_{\dot{m}_C} = \frac{|\dot{m}_C^{out} - \dot{m}_C^{in}| \cdot 100}{\dot{m}_C^{in}} = 0.022\%$
- lateral $err_{\dot{m}_L} = \frac{|\dot{m}_L^{out} - \dot{m}_L^{in}| \cdot 100}{\dot{m}_L^{in}} = 0.028\%$

The fluid temperature at the outlets has been calculated in Fluent as the mass-weighted average on the outlets:

$$\overline{T}_C^{out} = 319.93 \text{ K} \quad \text{and} \quad \overline{T}_L^{out} = 319.30 \text{ K}$$

The heat transferred to the fluid has been calculated as

$$Q_{check} = c_{pw} \cdot (\dot{m}_C^{out} \cdot \overline{T}_C^{out} + \dot{m}_L^{out} \cdot \overline{T}_L^{out} - (\dot{m}_L^{in} + \dot{m}_C^{in}) \cdot T_{cold}) = 1695 \text{ W}$$

Remembering that the total heat produced by the cells is

$$Q = Q_C + Q_L = 1629 \text{ W}$$

the percentage error is

$$err_Q = \frac{|Q - Q_{check}|}{Q} = 4\%$$

During the simulation, reversed flows have been detected on some outlets, probably because the inlets/outlets ducts have not been extended enough to sufficiently reduce the flow rotationality.

8.5 Results

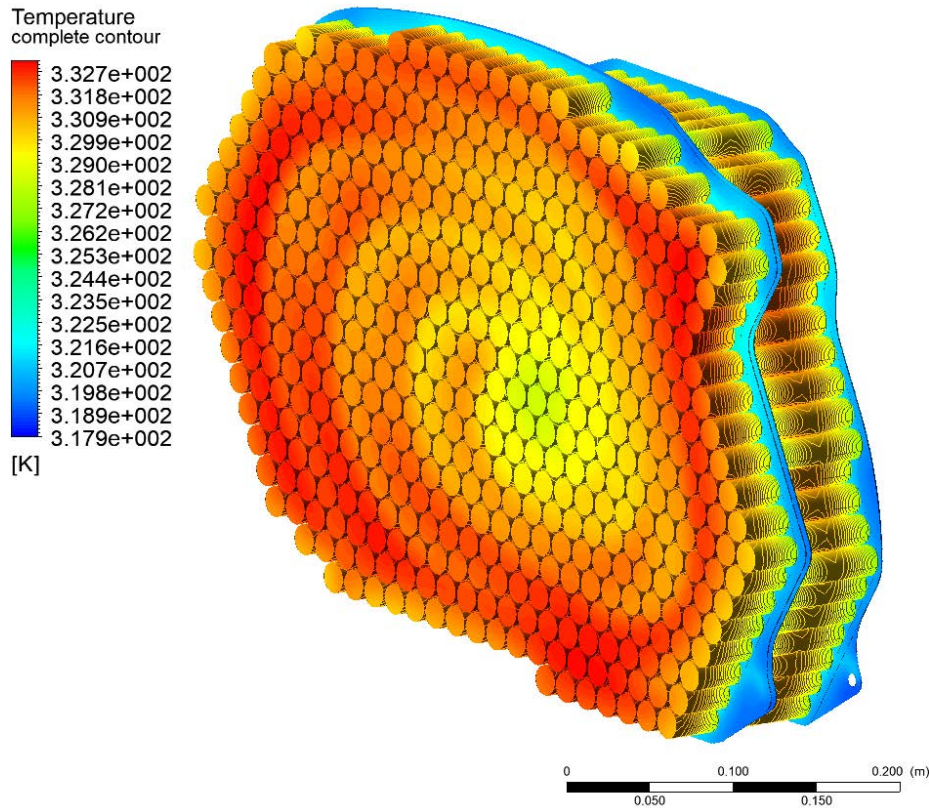


Figure 8.15: Complete temperature contour; the maximum temperature is, just for coincidence, 60.01 °C

Here the results of the numeric simulation are presented and discussed. Some **significant cells** (marked in figure 8.16) have been selected and the quantities on their axis have been investigated and presented in the following sections.

Table 8.1 presents the percentage of the total mass outflow on the single outlets; obviously, because of the shape difference between the channels, the balance is not perfect.

However the difference can be neglected or compensated with throttle valves on the outlets; this could be a method to induce a deliberate disequilibrium to further uniform the temperature distribution.

Table 8.2 provides the heat transfer coefficients and the normalized temperature differences between cells and BCP wall on the significant positions, computed with Fluent's result: α_{LI} is the heat transfer coefficient computed on the inner wall of the lateral BCP, α_{CO} is computed on the wall of the central BCP cooling the lateral cells, α_{CI} is computed on the wall of the central BCP cooling the central cells. Using the same subscripts to refer to the same locations, the ΔT s are reported to check the thermal dynamics of the layers: if the interface resistance were correctly calibrated,

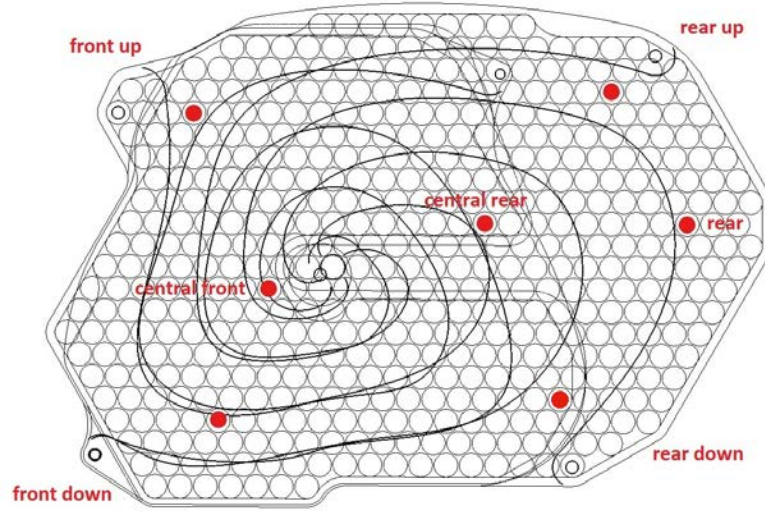


Figure 8.16: Significant cells axes positions with their denomination

outlet	mass flow	percentage
central post-up	0.03263 kg/s	23.45%
central post-down	0.03541 kg/s	25.45%
central front-down	0.03885 kg/s	27.92%
central front-up	0.03225 kg/s	23.18%
lateral up	0.03573 kg/s	47.12%
lateral down	0.04009 kg/s	52.86%

Table 8.1: Mass flow on single outlets and percentage of the total flow

all those values should have been nearly equal to $2.22 K$ (see section 5.3). The heat transfer coefficients are computed as

$$\alpha = \frac{Q_1/2}{A_{hex} \cdot (T_w^* - T_f^*)} \quad (8.9)$$

where $A_{hex} = 3.2931 \times 10^{-4} m^2$ is the area of a hexagon with the opposite sides 19.5mm distant (figure 5.5d), T_w^* is the temperature at the fluid/BCP wall interface and T_f^* is the correspondent temperature in the middle of the fluid layer.

The normalized temperature differences are computed as

$$\Delta T = \frac{T_c^* - T_w^*}{Q_1} \quad (8.10)$$

where T_c^* is the internal temperature on the cell's axis, at 2mm from the tab (same spots used in section 5.3).

The quantities marked with the * have been obtained with the Fluent's probe tool.

position	α_{LI}	α_{CO}	α_{CI}	ΔT_{LI}	ΔT_{CO}	ΔT_{CI}
front up	1457	1126	1072	2.315	2.227	2.277
front dwn	1480	2917	2250	2.294	2.233	2.255
rear up			1276			2.271
rear down	2710	5404	1120	2.209	2.330	2.271
central front	2767	3028	2593	2.270	2.284	2.279
central rear	1977	1899	1514	2.265	2.260	2.253
rear			1519			2.253

Table 8.2: Heat transfer coefficients (α in $\frac{W}{m^2K}$) and temperature differences between the BCP fluid/wall interface and a spot 2 mm inside the cell (ΔT in K), computed on the significant cells' axes marked in 8.16 . The heat transfer coefficient is significantly higher than the one predicted in the BCPs performance study and some hypotheses are formulated in section 8.6.

8.5.1 Fluid flow

During the first few runs of the simulation, while checking convergence behaviour and testing software's options, fluid domains have been simulated with the tie-rods collars encumbrance.

The reader should keep in mind that the results presented here are probably inaccurate, since the mesh and the simulation setup were still provisional.

However, the streamlines suggested some modifications to the spirals geometry and to the tie-rods position, in order to avoid whirlpools and slow sectors.

Another minor modification to the spirals of the central BCP has been made, in a more advanced state of the thesis, to help uniform the temperature.

Figure 8.17 compares the very first geometry with two other stages.

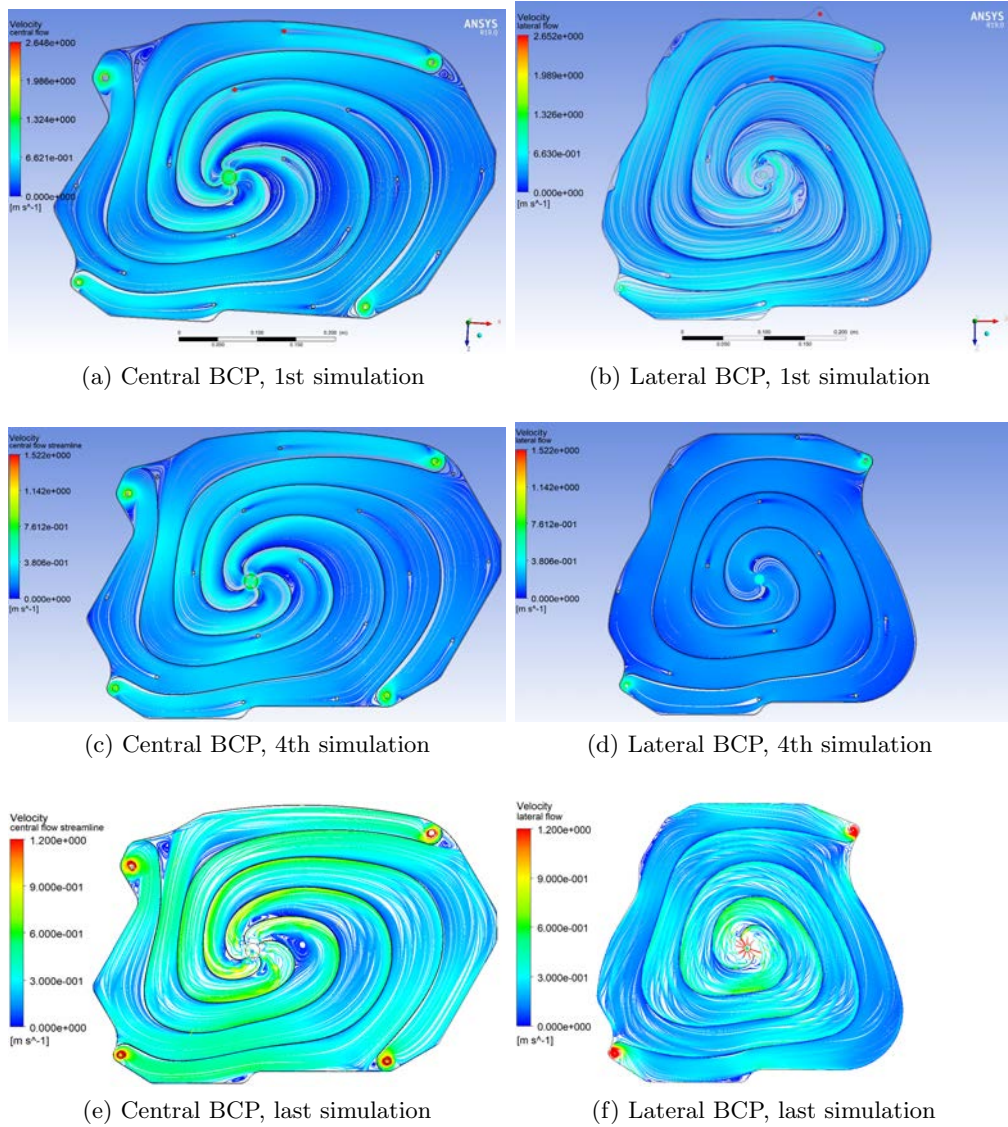


Figure 8.17: History of the fluid flow improvements; the top ones show the streamlines, on planes in the middle of the two BCPs, with from the very first geometry (the tie-rods marked in red are the one that has been relocated, the top one for BCPs manufacturing reasons, the bottom one to improve the lateral BCP flow).

(c) and (d) are the streamlines obtained after some modifications to the spirals (smoothed curves, modified the spiral near the top-front central outlet).

The bottom ones are the streamlines of the last simulation, without tie-rods and with the central spirals slightly modified in the rear zone to increase the fluid velocity.

Note that the viscous model used in (a), (b), (c) and (d) is not necessary the laminar one; this information has not been recorded since those simulation were a test, therefore their result has to be intended as merely qualitative.

8.5.2 Temperature and pressure

The maximum temperature among the cells is **333.16 K** while the minimum is 328.14 K ; the difference between the hotter and the colder cell in the pack is therefore $333.16\text{ K} - 328.14\text{ K} = 5.02\text{ K}$.

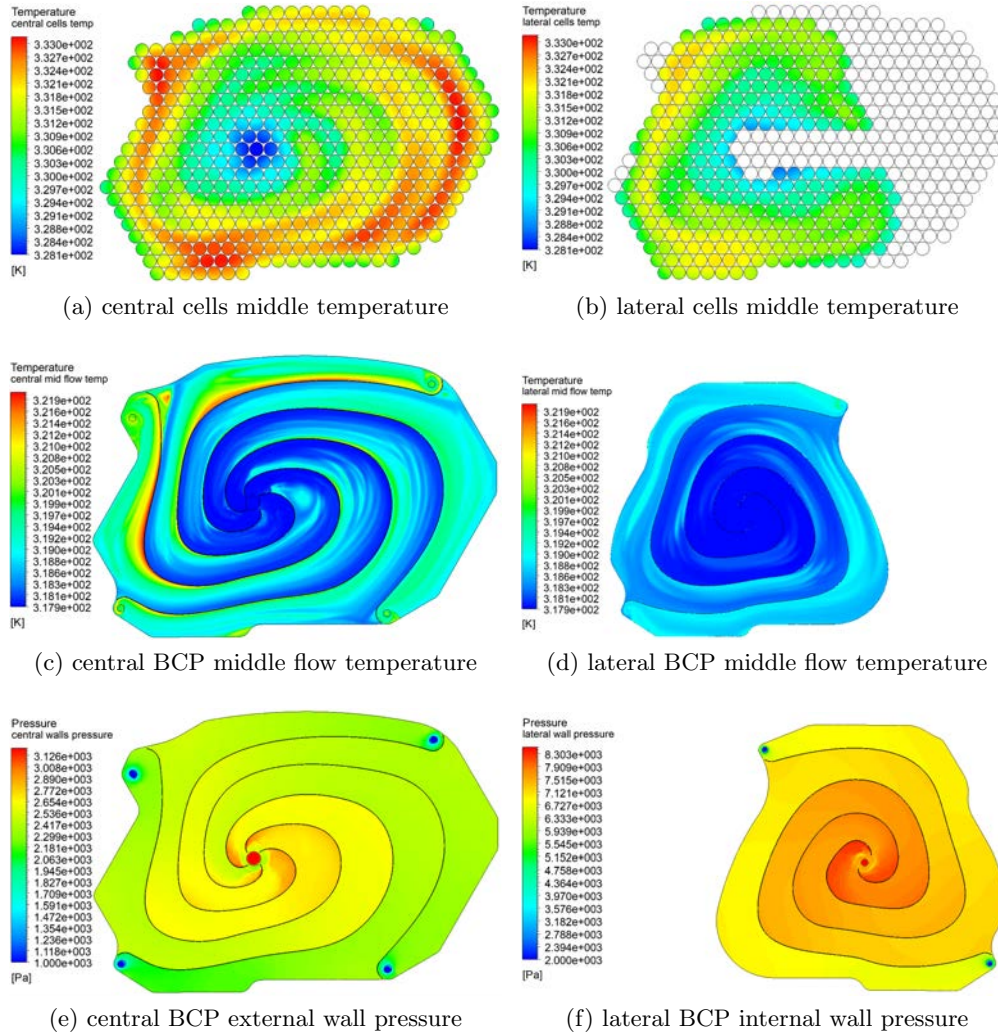


Figure 8.18: Contours of cells temperature, flow temperature and pressure; the cell temperature is investigated on their symmetry plane, flow temperature is investigated on a plane placed in the center of the flow while pressure is investigated on the fluid/wall interface on the inlets/outlets side.

The lateral/central temperature contours have the same max/min settings in order to appreciate the differences.

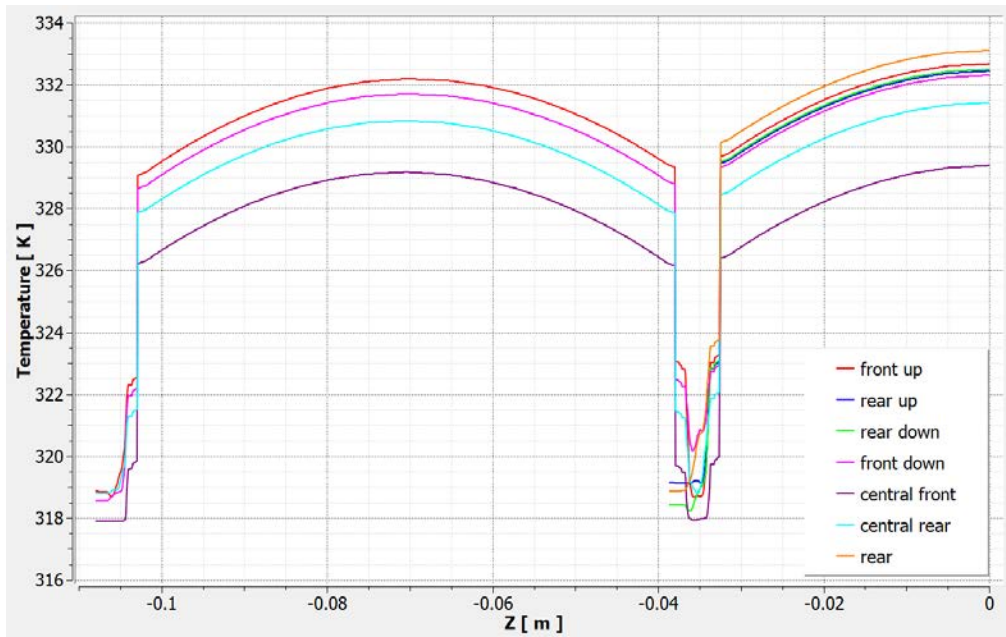


Figure 8.19: Temperature of the cells axis in the significant positions (figure 8.16). The temperature difference in the same cell is about 3 K and the disequilibrium between the two BCPs is quantifiable with the difference in the maximum temperature of two coaxial cells; for example, the front-up axis measures a maximum of 332.2 K on the lateral cell and 332.7 K on the central one.

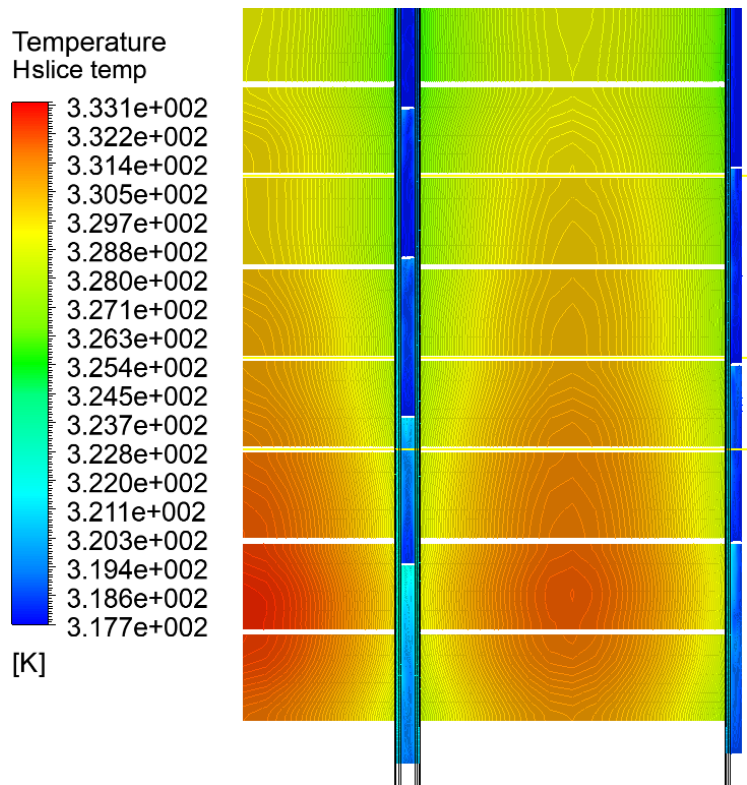


Figure 8.20: Horizontal section temperature contour

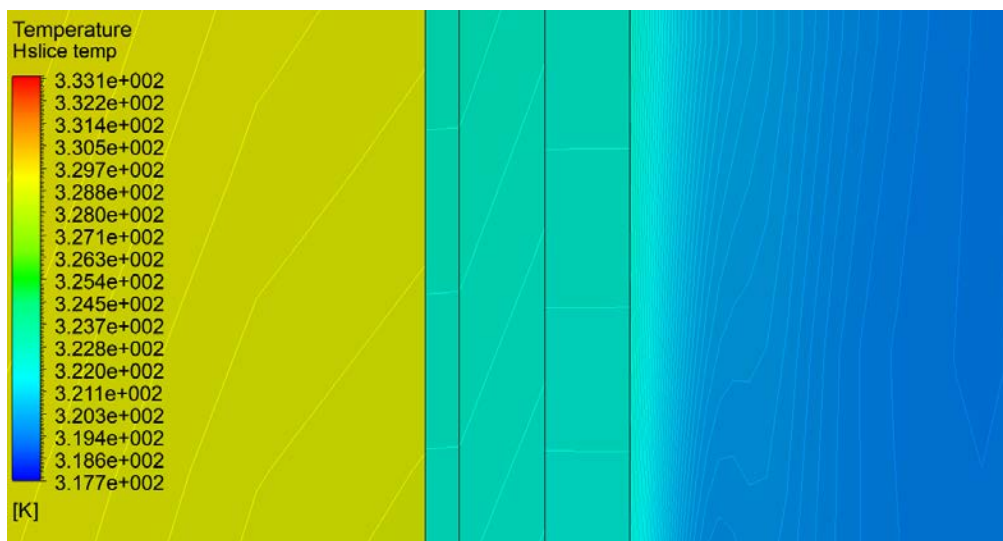


Figure 8.21: Horizontal section temperature contour, detail. The temperature step between the cell and the electric plate, caused by the interface resistance, is clearly visible. Another small step can be spotted between the BCP wall and the thermal-pad layer; this is probably caused by an interpolation error due to mesh not being conformal.

8.5.3 Comparison of the flow with and without spirals

Now a brief comparison between the cases with and without the spirals. The first difference can be noticed in the volume-average fluid velocity in the main fluid domains, provided by Fluent:

- average velocity **with** spirals : 0.3076 m/s
- average velocity without spirals : 0.08162 m/s

Also the volume-average temperature in the cells is significantly different:

- average temperature **with** spirals : 330.1 K
- average temperature without spirals : 332.3 K

In addition, figure 8.22 shows the fluid flow and cells temperature in this case.

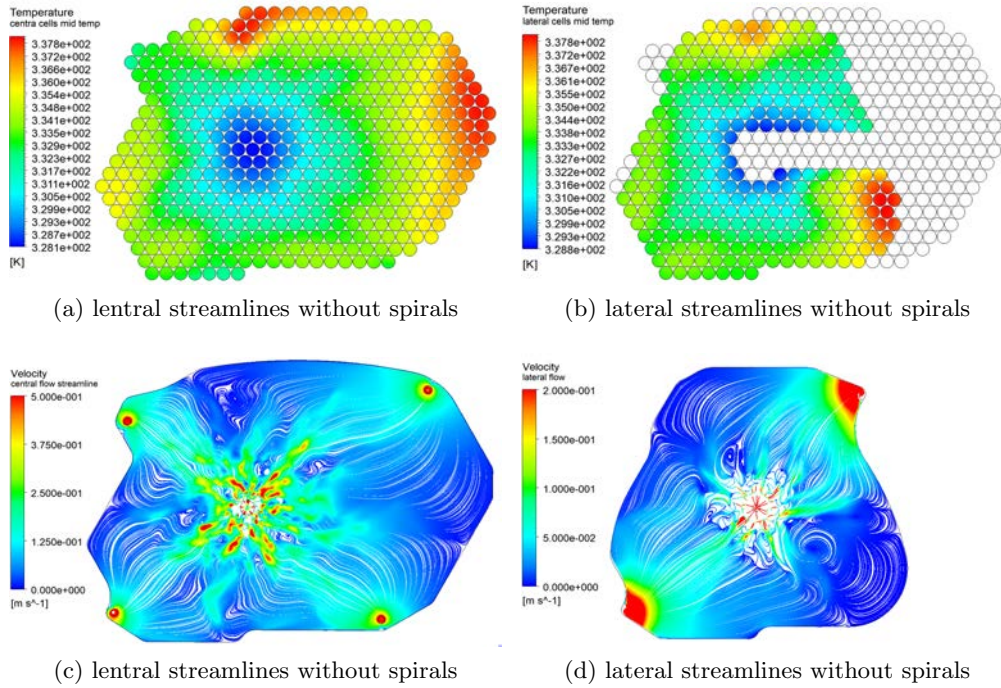


Figure 8.22: Cells temperature and velocity streamlines in the case of radial flow. The velocity is much lower, on average, than with the spirals. It is also clearly visible the problem of slow zones mentioned in section 4.4. The maximum temperature is 338.1 and the difference between the hotter and the colder cell in the pack is 9.32 K.

In addition, the same table of the heat transfer coefficients computed in the case of the spirals (table 8.2) has been made in the case without spirals (table 8.3).

position	α_{LI}	α_{CO}	α_{CI}
front up	755	829	853
front dwn	848	845	833
rear up			669
rear down	1607	894	821
central front	1935	2248	1894
central rear	928	1431	965
rear			569

Table 8.3: Heat transfer coefficients table in the case without spirals, for details refer to table 8.2. These coefficients are 47.6 % lower, on average, than the ones in the case with spirals.

8.6 Comments

In figure 8.17 we can observe the streamlines in the lateral BCP behave better than the ones in the central BCP; indeed, while the central cells stack has been adapted to the frame before the adoption of the spirals and presents some sharp corners, the lateral stack has been modeled to be as round as possible and its shape is therefore optimal for the spiralitic channels layout.

In the central BPC some whirlpools are present in consequence of the last modification with which the spirals have been extended toward the rear of the pack; **the central spirals could be further optimized** to improve the quality of the fluid flow and even better results could be achieved if the central stack is modeled from the beginning with this in mind.

The **disequilibrium between the performance of the two BCPs**, appreciable in fig. 8.19, is probably caused by the way the performance of the two BCPs are computed in the study: considering only one lateral area Ap_{exg} for the lateral BCP lead to an overestimation of the necessary mass flow.

The pressure on central inlet is about 3500 Pa, while on lateral inlet is about 9500 Pa; since the outlet pressure have been set at 0 Pa, these can be seen as the **pressure losses** in the BCPs; the central BCP must have a throttle valve in its inlet or outlets, in order to be fed in parallel with the lateral BCP. Since **no material roughness has been set up** in Fluent, these pressure losses only take into account the sudden deviations. These values are much higher than the calculated ones in the BCP performance study and this is not a surprise, since those values did not take into account the losses from sudden deviation especially near the inlets and outlets; however, the proportion between the pressure losses in the two BCPs has been maintained (2.78 in the feas. study vs 2.71 in Fluent).

As shown in figure 8.21, the non-conformal mesh between the BCP walls and the thermal-pad layer causes a **undesired interface resistance** due to the interpolation error between the two meshes; this is probably con-

tributing in the small difference (4.95 % max) between the expected thermal resistance (2.22 K/W) and the measured one (table 8.2). The other inaccuracy is considering Q_1 as the heat flow through the area: the heat flow through the cells' tabs can be unbalanced and influenced by the nearby cells.

The **heat transfer coefficients** presented in table 8.2 are **very different from the predictions** in the BCPs performance study. The reasons can be multiple:

- As mentioned, Q_1 is not necessarily the heat flowing through the tab and the underneath layers; the real heat flow depends also, in first approximation, on BCPs disequilibrium.
- The equation used to compute the Nusselt number Nu can lead to high errors, especially with particular shapes of the channels.

Last, a little modeling imprecision must be highlighted and explained: the electrical connection plates have been merged in a single, continuous layer to simplify the meshing process; consequently, while in the real system the plates edges are at a minimum of 4mm from each other (for insulation reasons, see figure 3.13) and thus they are not completely in contact with the cell, in the simulation all the cells have their tabs completely in contact with the plate (see figure 8.3).

Since the plates are not divided, the heat from a 11 cells parallel group can spread also to the nearby groups through the copper, and this slightly improve the cooling homogeneity in the simulation; moreover, since in the simulation even the cells that in reality are connected to the perimeter of a plate are cooled from the whole tab surface, their cooling completely exploit the higher axial thermal conduction of the cell and is therefore overestimated.

A better modeling procedure would have been using the actual plates geometry: meshing problems aside, Fluent permits to define either an *orthogonal* thermal conductivity or a *cyl-orthogonal* one. The correct definition for a single cell would be a cylindrical-orthogonal since the high conductivity, as explained in section 4.2, is both axial and tangential; however it is not allowed to specify multiple axis, in the same model, for this option and the possibility to create some sort of super-element for the cell has not been taken into account until a late stage of the work.

Not being able to model the conductivity in the cell as cylindrical means that cells can not take advantage of the high tangential conduction to spread the heat toward the partial region of the tab in contact with the plate, therefore excessively penalizing the cooling of these cells.

Chapter 9

Conclusions

The **cooling system passed the verification** and is able to drain the heat produced by the cells, maintaining them under the acceptable limit in most circumstances and with a **satisfactory homogeneity**.

The boundary conditions of the system were:

- External air temperature: 40 °C
- External air speed: 182 *km/h*
- Heat production in the cells pack: 3258 *W* (9.3 % of the power supplied)

And the resulting operative conditions are:

- Maximum cell core temperature: 60,01 °C, while the maximum temperature acceptable was 60 °C
- Difference between the hottest cell core and the colder one: 5.02 °C
- Temperature difference inside a cell: about 3 °C

Since the passive cooling (radiation and air convection) has not been taken into account, both the maximum temperature and the maximum temperature difference between the cells of an operative system (with the same heat generation) is **expected to be lower than the simulation predictions**.

Some critic comments to the modeling are reported in section 8.6 while the limits of the design and the future developments are listed in chapter 10.

Chapter 10

Future developments

This thesis is clearly the most technical part of a larger project, started with the general design of the motorbike and going on to produce a mature project for the construction of the battery, once the funds are raised. Here is a list of the programmed activities that will be carried outside this thesis.

- The very first activity must be the measurement of the **actual heat produced** by the selected cells and its implementation in the numerical simulation.
- A battery management system (**BMS**) must be chosen and fit inside the battery pack: it provides cells balancing, telemetry and security features. A feasibility reasoning already proved that the space between the cells is just enough to accommodate the wiring.
- Some dimensions in the geometry can be adjusted, as explained in the results discussion section (8.6).
- A **reduced model** of the battery (≈ 50 cells) will be built, to measure the actual performance of the cooling system and definitively prove the feasibility of the BCPs manufacture process.
- The very next design topic is the **detachment system**; the hydraulic circuit must be quickly decoupled and coupled with the air side, fixed to the frame.
Since the fast couplers would likely introduce air, an anti-bubble system must be inserted in the circuit.
- The hydraulic circuit must also, as stated above, be calibrated: the two BCPs (central and lateral) have different pressure drop but they are fed in parallel, so the branch with the lower pressure drop must be compensated with a **restrictor**.
- A performance improvement can derive from the research of a **more conductive thermal pad**, or its substitution with thermal paste (together with a more solid polymeric net preventing the electrical

contact between cells and BCPs), generally having a lower interface resistance.

- A **thermostatic system** can be implemented, so the water circulation is controlled to maintain the pack at an optimal temperature.
- **More versions of this battery pack** could be designed; this configuration aimed to high autonomy and cooling performance, but some applications may require a lighter pack with a lower capacity: the number of cells could be reduced and aluminum can be used in place of copper for the BCPs.
- **The security of spreading thermal paste on the positive tab** of the cell must be investigated: it may increase the self discharge of the cell and compromise the functionality of the vent valve (CID), so a measure of the self-discharge should be executed and a security test, provoking the thermal run-away of a cell should be carried on.
- The **peak power behaviour** of the system would be interesting to be investigated: the motor (and also the battery) can produce 70 kW for a few seconds and this can be exploited as a temporary boost in a race.
The cooling system would not be capable of extracting the consequent amount of heat in the same environment
- The cooling technology can be extended to every type of cylindrical cell, so other formats can be considered.
- Finally, while this thesis is being valuated by the university, there's a **patent pending** on the cooling plates' internal geometry.

Now some **limits of the present design** deserve to be highlighted:

- **The cells are not easily replaceable**, and repairing the pack if some cells fails can be both expensive and dangerous; it is therefore good practice to use cells with a low fail rate.
- Since the cells have, as any other mechanical product, dimensional tolerances on their length, **the connection plates layer could result wavy**; the thermal pad layer is able to compensate this problem within certain limits, but would be good practice to choose cells with low dimensional tolerances.
- Lacking the cells of an individual fuse, if a cells short-circuits it reserves the same fate for all the other cells connected in parallel with it.

Acknowledgements

The greatest acknowledgement goes to professor P. Brunello, who embraced with enthusiasm the proposal of being the supervisor for this thesis and guided its development with interest, great competence and professionalism.

Special thanks go to the Corvedo group whose members are Giorgio Scantamburlo, Luca Sandrucci, Alessandro Maiorca, Barnaba Marchesini, Matia Bettio, Daniele Ferrotti and Matteo Destro, which played a crucial role in the genesis of the electric moto3 project and led to the design of this battery, supporting the project with great excitement, deep passion and desire to take the challenge; a special mention is reserved to Giorgio, passionate engineer by my side during the technological scouting ended up in the simulated system.

In addition, Ing. Stefano Bortolin and Prof. Massimo Guarnieri deserve many thanks, since their willingness to support the project and provide very useful tips surely paved the way to these results.

I also want to thank Francesco Maltoni, who firstly proposed to supervise this thesis and provide support.

Last but not least, i want to thank my family, always supporting and inspiring me, source of never ending curiosity and passion for science and technology. Vi voglio bene.

Appendix A

Data-logger calibration

The measurements of the data logger have been compared with the ones of a Fluke 289 (serial number: 43930028), metrologically certified by the producer.

Voltage measures:

Fluke resolution: 0.001 Vdc

Datalogger resolution: 0.01 V

Fluke accuracy: $\pm (0.025 \% + 2)$ Vdc

The following table reports the comparison between the same voltage (Vdc) values measured with Fluke 289 and the homemade datalogger.

Fluke	datalogger	Δ	$\Delta \%$
0.518	0.54	0.022	4.111
1.037	1.07	0.033	3.047
3.059	3.07	0.011	0.358
10.332	10.34	0.008	0.077
19.906	19.90	0.006	0.030
30.055	30.04	0.015	0.050
40.529	40.51	0.019	0.047
50.646	50.58	0.066	0.130
58.22	58.27	0.05	0.086

The maximum percentage difference is 4.111 %, so we can say, in first approximation, that the accuracy of the datalogger is:

Datalogger accuracy: $\pm (4.136 \% + 2)$ Vdc

Current measures:

Fluke resolution: 0,001 Adc

Datalogger resolution: 0.01 Adc

Fluke accuracy: 0,3 % + 2 Adc

The following table reports the comparison between the same current (Adc) value measured with Fluke 289 and the homemade datalogger.

Fluke	datalogger	Δ	Δ %
0.295	0.30	0.005	1.67
0.523	0.54	0.017	3.20
0.990	1.01	0.020	1.99
2.164	2.19	0.026	1.19
3.013	3.04	0.027	0.90
3.952	3.96	0.008	0.20
4.965	4.98	0.015	0.31
9.980	9.99	0.010	0.10

The maximum percentage difference is 3.20 %, so we can say, in first approximation, that the accuracy of the datalogger is:

Datalogger accuracy: $\pm (3.50 \% + 2)$ Vdc**Temperature measures:**

Fluke resolution: 0,1 °C

Datalogger resolution: 0,1 °C

Fluke accuracy: $\pm (1\% + 10)$ °C

The datalogger has 8 thermocouples, named from T1 to T8.

Their measurement, compared with the multimeter's one, on two different hot bodies are reported in the following table.

Fluke	measure	Δ	Δ %	measure	Δ	Δ %
	22.1	-	-	50.5	-	-
T1	22.3	0.2	0.90	51.4	0.9	1.75
T2	22.8	0.7	3.07	50.4	0.1	0.20
T3	22.6	0.5	2.21	50.9	0.4	0.79
T4	21.8	0.3	1.38	50.8	0.3	0.59
T5	22.7	0.6	2.64	50.7	0.2	0.39
T6	22.4	0.3	1.34	50.9	0.4	0.79
T7	22.8	0.7	3.07	51.2	0.7	1.37
T8	22.3	0.2	0.90	51.0	0.5	0.98

The maximum percentage difference is 3.07 %, so we can say, in first approximation, that the accuracy of the datalogger is:

Datalogger accuracy: $\pm (4.07 \% + 10)$ °C

Appendix B

Matlab scripts

Here are reported the Matlab codes used to simulate the radiator and analyze the conduction calibration experiment data.

The radiator code is divided in a main script, *software_radiator_coupling* and three functions, *parametri_geometrici*, *gui_radiator2* and *verifica_radiatore*. This last function calculates the heat exchanged, provided with the inputs requested in the main script and converted in *parametri_geometrici*, that contains other typical air radiators parameters.

The nature of this software is explained in [15] and [6].

The last code analyzed the data logged during the experiment for the conduction calibration (section 5.3); another script, automatically generated by Matlab, imported the data and created the following variables:

- *ID* : logs counter
- *date* : a *table* containing the six vectors reporting the date and time
- *Cs* : a *cell* containing the eight vectors with the thermocouples' log
- *AMPERE* : current fed to the resistors
- *VOLT* : voltage on the resistors
- *WATT* : the multiplication of the last two vectors

```

%%%%%%%%%% COOLING SYSTEMS VERIFY %%%%%%%%%%%

clearvars
clc

T= 50;           %motor continuos torque in Nm
R= 13/54;        %transmission ratio
rr=0.3 ;         %wheel radius in m
V=182;           %air speed km/h

T_hot= 44; %guess
deltaT=1e-4;
k=1; %counter

while abs(deltaT)>1e-6
    %% PARAMETERS

    l = 20 ;           % spessore [mm]
    lm = 290;          % Lunghezza multiporte [mm]
    p = 10;            % Passo multiporte [mm]
    n = 15;            % Numero di multiporte

    global PR
    PR= 2.7;           % passo reale alette [mm]
    s = 2;             % Spessore totale multiporte in mm
    sm = 0.37;         % Spessore parete multiporte in mm
    T_hot=T_hot+deltaT
    Q_H2O = 0.3622;    % Portata di H2O [kg/s]
    V_aria= V/3.6;     % Velocità aria [m/s]
    T_aria= 40;        % Temperatura aria in ingresso✓

[C°]

    %%CICLI
    g=0;

    %% PARAMETRI FISSI DEL MATERIALE (ALLUMINIO)
    % k = 237;          % Conduttività alluminio in✓
W/mK
    d = 2700;          % Densità alluminio in Kg/m^3
    global mu
    mu = 0.000377;    % Kg/m*s

    %% PARAMETRI ARIA
    global cpAria
    cpAria=1010; % in J/KgK
    global roAria
    roAria= 1.175;% in Kg/m^3
    global muAria
    muAria= 1.7*10^-5; %in Pa*s

```

```

global LambdaAria
LambdaAria= 0.026; %[W/m*K]

%% VERIFICA TERMICA
%Si vuole effettuare la verifica termica del sistema di raffreddamento
%vettura. si considerano due casi di verifica: radiatori acqua e
%radiatori olio.
scelta_radiatore = 1; %Quale tipo di radiatore si vuole✓
verificare?
%1) Radiatore Acqua 2) Radiatore Olio

if scelta_radiatore == 1;

    %RADIATORI ACQUA:
    % global cpH2O
    cpH2O=4186; % in J/kgK
    % global roH2O
    roH2O= 975; % in Kg/m^3
    global LambdaAcqua
    LambdaAcqua= 0.676; %[W/m*K]
    global muAcqua
    muAcqua = 0.000377; %[kg/m*s]
    % Q_H2O = input('Portata di H2O [kg/s]: '); %espressa in✓
kg/s
    % V_aria=input('Velocità aria [m/s]: '); %espressa in✓
m/s
    % T_H2O=input('Temperatura acqua in ingresso [C°]: ');
    % T_aria=input('Temperatura aria in ingresso [C°]: ');

    [li,si,Lp,Fl,tD,Ll,Tp,Ft,teta,A,Aa,At,Aba] =...
        parametri_geometrici(l,lm,p,n,PR,s,sm);

    [NTU,eps,Qreal,C,Ca,r,Qmax1,V_aria] =...
        verifica_radiatore (cpAria,cpH2O,li,si,Lp,Fl,tD,Ll,...
            Tp,Ft,teta,A,Aa,At,Aba,Q_H2O,V_aria,T_hot,T_aria);

end

% if scelta_radiatore == 2
%
% %RADIATORI OLIO:
% %NB i nomi delle variabili rimangono uguali per semplicità di
% scrittura del software
% global cpH2O
% cpH2O=1280; % in J/kgK
% global roH2O
% roH2O= 9000; % in Kg/m^3
% global LambdaAcqua
% LambdaAcqua= 0.145; %[W/m*K]
% global muAcqua
% muAcqua = input('inserire viscosità olio in [kg/m*s] = ');
% Q_H2O = input('Portata di Olio [kg/s]: '); %espressa in✓

```

```

kg/s
% V_aria=input('Velocità aria [m/s]: ');           %espressa in m/s
% T_H2O=input('Temperatura olio in ingresso [C°]: ');
% T_aria=input('Temperatura olio in ingresso [C°]: ');
% [li,si,Lp,Fl,tD,Ll,Tp,Ft,teta,A,Aa,At,Aba] =...
%     parametri_geometrici(l,lm,p,n,PR,s,sm);
% [NTU,eps,Qreal,C,Ca,r,Qmax1,V_aria] = ...
%     verifica_radiatore (cpAria,cpH20,li,si,Lp,Fl,tD,Ll,Tp,...
%     Ft,teta,A,Aa,At,Aba,Q_H20,V_aria,T_H20,T_aria);
%
% end

omega= V/3.6 / (2*pi*rr) / R *2*pi;   %velocità angolare motore in
Q= omega*T*0.951; %potenza erogata se la coppia rimane sempre massima
Qmax= 3258; % W @ 182 km/h(da excel)
Q_diss=Qreal*1000;

T_cold=T_hot - Q_diss/(Q_H20*cpH20)
deltaT=(min(Q,Qmax)-Q_diss)/(Q_H20*cpH20);

k=k+1;
end

% %% PLOT Eps vs NTU
% figure(1)
% % Qa= A*V_aria;           %Portata aria m^3/s
% % C=Q_H20*cpH20;         %[W/K]
% % Ca=Qa*cpAria;         %[W/K]
% r=Ca/C;
% NTUi = 0:0.10:5;
% eps_real = 1-exp(((1/r)*NTUi.^0.22).*(exp(-r*(NTUi).^0.78)-1));
% plot(NTUi,eps_real,'r','linewidth',3)
% xlabel('NTU');
% ylabel('Eps');
% text(3,0.6,sprintf(['r =',num2str(r),'\n','epsilon =',num2str(eps),...
%     '\n','NTU =',num2str(NTU)]),'FontSize',16);
% grid on
% %%%

```



```

function[li,si,Lp,Fl,tD,Ll,Tp,Ft,teta,A,Aa,At,Aba] =...
    parametri_geometrici(l,lm,p,n,PR,s,sm)

% PARAMETRI MULTIPORTE CALCOLATI

li = l-2*sm;           % Larghezza multiporte interna
si = s - 2*sm;        % Spessore interno multiporte in mm
h = n*p + n*s;        % Altezza Radiatore

% PARAMETRI ALETTE FISSI
S=0.14;               %spessore aletta
H = p;                %altezza aletta=passo tra i multiporte
pa=PR/2;              %passo aletta
HR=sqrt(p^2+pa^2);    %altezza reale aletta
Lp=1;                 %passo intaglio
Fl=8;                 %lunghezza aletta
sm = 0.37;            %spessore della parete del multiporte
tD = l-(sm*2);        %diametro maggiore tubo (multiporte)
Ll=6.44;              %lunghezza intaglio
Tp = p;               %passo multiporte
Ft=0.14;              %spessore aletta
teta=23;              %angolo di intaglio

% AREE [m^2]
A =(lm*n*p)/10^6;     % Area frontale radiatore
Aa=((n*(lm^2)/PR)*HR*1)/10^6; % Area alettata in m^2
At =((s*lm*(n-1))+((S*HR*(lm^2)/PR)*n)+(2*(n-1)*1*lm)-...
    (((lm/PR)*S^2)*1))/10^6+Aa; % Area totale
Aba = lm*(2*(li+si)*n)/10^6;

end

```

```
function varargout = gui_radiator2(varargin)
%GUI_RADIATORI2 M-file for gui_radiator2.fig
%   GUI_RADIATORI2, by itself, creates a new GUI_RADIATORI2 or raises
%   the existing singleton*.
%
%   H = GUI_RADIATORI2 returns the handle to a new GUI_RADIATORI2 or
the
%   handle to the existing singleton*.
%
%   GUI_RADIATORI2('Property','Value',...) creates a new GUI_RADIATORI2
%   using the given property value pairs. Unrecognized properties are
%   passed via varargin to gui_radiator2_OpeningFcn.
%   This calling syntax produces a warning when there is an existing
%   singleton*.
%
%   GUI_RADIATORI2('CALLBACK') and
%   GUI_RADIATORI2('CALLBACK',hObject,...) call the local function
named
%   CALLBACK in GUI_RADIATORI2.M with the given input arguments.
%
%   *See GUI Options on GUIDE's Tools menu. Choose "GUI allows only
one
%   instance to run (singleton)".
%
% See also: GUIDE, GUIDATA, GUIHANDLES

% Edit the above text to modify the response to help gui_radiator2

% Last Modified by GUIDE v2.5 21-Feb-2017 17:24:41

% Begin initialization code - DO NOT EDIT
gui_Singleton = 1;
gui_State = struct('gui_Name',       mfilename, ...
                  'gui_Singleton',  gui_Singleton, ...
                  'gui_OpeningFcn', @gui_radiator2_OpeningFcn, ...
                  'gui_OutputFcn',  @gui_radiator2_OutputFcn, ...
                  'gui_LayoutFcn',  [], ...
                  'gui_Callback',   []);
if nargin && ischar(varargin{1})
    gui_State.gui_Callback = str2func(varargin{1});
end

if nargout
    [varargout{1:nargout}] = gui_mainfcn(gui_State, varargin{:});
else
    gui_mainfcn(gui_State, varargin{:});
end
% End initialization code - DO NOT EDIT

% --- Executes just before gui_radiator2 is made visible.
function gui_radiator2_OpeningFcn(hObject, eventdata, handles, varargin)
```

```
handles.output = hObject;

% Update handles structure
guidata(hObject, handles);

% UIWAIT makes gui_radiator2 wait for user response (see UIRESUME)
% uiwait(handles.figure1);

% --- Outputs from this function are returned to the command line.
function varargout = gui_radiator2_OutputFcn(hObject, eventdata, handles)
% varargout cell array for returning output args (see VARARGOUT);
% hObject    handle to figure
% eventdata  reserved - to be defined in a future version of MATLAB
% handles    structure with handles and user data (see GUIDATA)

% Get default command line output from handles structure
varargout{1} = handles.output;

function boxSX_CreateFcn(hObject, eventdata, handles)
imshow('sintesi.JPG')

function boxDX_CreateFcn(hObject, eventdata, handles)
imshow('sintesi.JPG')

function calcola_Callback(hObject, eventdata, handles)

function modifiche_Callback(hObject, eventdata, handles)

function modifiche_CreateFcn(hObject, eventdata, handles)
% hObject    handle to modifiche (see GCBO)
% eventdata  reserved - to be defined in a future version of MATLAB
% handles    empty - handles not created until after all CreateFcns called

% Hint: popmenu controls usually have a white background on Windows.
%       See ISPC and COMPUTER.
if ispc && isequal(get(hObject,'BackgroundColor'),...
    get(0,'defaultUicontrolBackgroundColor'))
    set(hObject,'BackgroundColor','white');
end

function edit19_Callback(hObject, eventdata, handles)
% hObject    handle to edit19 (see GCBO)
% eventdata  reserved - to be defined in a future version of MATLAB
% handles    structure with handles and user data (see GUIDATA)
```

```
% Hints: get(hObject,'String') returns contents of edit19 as text
%         str2double(get(hObject,'String')) returns contents of edit19 as a
%         double
```

```
% --- Executes during object creation, after setting all properties.
function edit19_CreateFcn(hObject, eventdata, handles)
% hObject    handle to edit19 (see GCBO)
% eventdata  reserved - to be defined in a future version of MATLAB
% handles    empty - handles not created until after all CreateFcns called
```

```
% Hint: edit controls usually have a white background on Windows.
%         See ISPC and COMPUTER.
```

```
if ispc && isequal(get(hObject,'BackgroundColor'),...
    get(0,'defaultUicontrolBackgroundColor'))
    set(hObject,'BackgroundColor','white');
end
```

```
function edit20_Callback(hObject, eventdata, handles)
% hObject    handle to edit20 (see GCBO)
% eventdata  reserved - to be defined in a future version of MATLAB
% handles    structure with handles and user data (see GUIDATA)
```

```
% Hints: get(hObject,'String') returns contents of edit20 as text
%         str2double(get(hObject,'String')) returns contents of edit20 as a
%         double
```

```
% --- Executes during object creation, after setting all properties.
function edit20_CreateFcn(hObject, eventdata, handles)
% hObject    handle to edit20 (see GCBO)
% eventdata  reserved - to be defined in a future version of MATLAB
% handles    empty - handles not created until after all CreateFcns called
```

```
% Hint: edit controls usually have a white background on Windows.
%         See ISPC and COMPUTER.
```

```
if ispc && isequal(get(hObject,'BackgroundColor'),...
    get(0,'defaultUicontrolBackgroundColor'))
    set(hObject,'BackgroundColor','white');
end
```

```
function edit21_Callback(hObject, eventdata, handles)
% hObject    handle to edit21 (see GCBO)
% eventdata  reserved - to be defined in a future version of MATLAB
% handles    structure with handles and user data (see GUIDATA)
```

```
% Hints: get(hObject,'String') returns contents of edit21 as text
%         str2double(get(hObject,'String')) returns contents of edit21 as a
%         double
```

```
% --- Executes during object creation, after setting all properties.
function edit21_CreateFcn(hObject, eventdata, handles)
% hObject    handle to edit21 (see GCBO)
% eventdata  reserved - to be defined in a future version of MATLAB
% handles    empty - handles not created until after all CreateFcns called

% Hint: edit controls usually have a white background on Windows.
% See ISPC and COMPUTER.
if ispc && isequal(get(hObject,'BackgroundColor'),...
    get(0,'defaultUicontrolBackgroundColor'))
    set(hObject,'BackgroundColor','white');
end

% --- Executes during object creation, after setting all properties.
function passo_alette_CreateFcn(hObject, eventdata, handles)
imshow('passo.JPG')

function Q_motore_in_Callback(hObject, eventdata, handles)
% hObject    handle to Q_motore_in (see GCBO)
% eventdata  reserved - to be defined in a future version of MATLAB
% handles    structure with handles and user data (see GUIDATA)

% Hints: get(hObject,'String') returns contents of Q_motore_in as text
%        str2double(get(hObject,'String')) returns contents of Q_motore_in
%        as a double

% --- Executes during object creation, after setting all properties.
function Q_motore_in_CreateFcn(hObject, eventdata, handles)
% hObject    handle to Q_motore_in (see GCBO)
% eventdata  reserved - to be defined in a future version of MATLAB
% handles    empty - handles not created until after all CreateFcns called

% Hint: edit controls usually have a white background on Windows.
% See ISPC and COMPUTER.
if ispc && isequal(get(hObject,'BackgroundColor'),...
    get(0,'defaultUicontrolBackgroundColor'))
    set(hObject,'BackgroundColor','white');
end

function Spessore_in_Callback(hObject, eventdata, handles)
l=get(handles.Spessore,'string');
l=str2num(a);
```

```

function [NTU,eps,Qreal,C,Ca,r,Qmax1,V_aria] = ...
    verifica_radiatore (cpAria,cpH2O,li,si,Lp,Fl,tD,Ll,Tp,Ft,...
        teta,A,Aa,At,Aba,Q_H2O,V_aria,T_H2O,T_aria)

global roAria;
global muAria;
global LambdaAcqua;
global LambdaAria;
global muAcqua;
global PR;
global mu;
dT = (T_H2O-T_aria);

%% VERIFICA
Qa = A*V_aria; %Portata aria m^3/s
C = Q_H2O*cpH2O; %[W/K]
Ca = Qa*cpAria; %[W/K]

Qmax1 = (Ca*dT)/1000;
r = Ca/C; %adimensionale
Pr = (cpH2O*mu)/LambdaAcqua; %adimensionale_Pr Acqua
%Calcolo del diametro idraulico in base al numero dei canali
N = 1;
li0 = li/N;
Diam_idraulico = (((2*li0*si)/(si+li0))/1000)*N; %Diametro idraulico
NiA=0; %efficienza alette (di solito si indica con omega)
g=0;
if(V_aria<8.3)
    NiA=0.87;
else if((8.3<V_aria)&&(V_aria<22.2))
    NiA=0.77;
    else if(V_aria>22.2)
        NiA=0.69;
    end
end
Ni = 1-(Aa/At)*(1-NiA); %rendimento area totale
AlfaAcqua=((LambdaAcqua/Diam_idraulico)*0.023*...
    ((4*Q_H2O/pi/Diam_idraulico/muAcqua)^0.8)*Pr^(1/3));
ReLp = (V_aria*roAria*(Lp/1000))/muAria;
J = ReLp^-0.49*(teta/90)^0.27*(PR/Lp)^-0.14*(Fl/PR)^-...
    0.29*(tD/Lp)^-0.23*(Ll/Lp)^0.68*(Tp/Lp)^-0.28*(Ft/Lp)^-0.05;
%NB ho cambiato Fp con PR (Fp= fin pitch= PR)
PrAria = (muAria*cpAria)/LambdaAria;
AlfaAria= (J*V_aria*roAria*cpAria)/(PrAria)^(2/3);
K= 1/(((1/AlfaAcqua)*(At/Aba))+((1/AlfaAria)*Ni));
NTU= (K*At)/Ca;
eps= 1-exp(((1/r)*NTU^0.22)*(exp(-r*(NTU)^0.78)-1));
Qreal = Qmax1*eps;
% disp(Qreal)

end

```

```
close all
clearvars -except Cs AMPERE WATT ID VOLT date

time=ID*2; % sampling every 2s

%correct NaN values in time vector
nantime=find(isnan(time));
for i=1:length(nantime)
    index=nantime(i);
    time(index)=(index-1)*2;
end
clear nantime index i

%finding the instant in which the power supply is turned off
start_exclusion=150; %exclude first samples
pwr_end_ind=find(abs(WATT(start_exclusion:end))<0.1)+start_exclusion;
if isempty(pwr_end_ind)
    pwr_end=length(WATT);
else
    pwr_end=(pwr_end_ind(1)-5); % in [s/2]
end
clear pwr_end_ind starting_exclusion

%computing ambient temperature
T_amb=mean([nanmean(Cs{5}),nanmean(Cs{6}),nanmean(Cs{7}),nanmean(Cs{8})]);

%% finding steady state start:
%computing the difference, in the steady state region mean value, between
%computing it from a certain instant and computing from that instant plus
%time_jump.
time_jump_ID=5*60/2; % in [s/2]
pertol=6e-3;
tol1=max(Cs{1})*pertol; % C1 tolerance
tol2=max(Cs{2})*pertol; % C2 tolerance
N=30; % diff under tolerance occurrences to identify steady state begin

for i=1:(pwr_end-time_jump_ID)
    diff_1(i)=Cs{1}(i+time_jump_ID)-Cs{1}(i);
    diff_2(i)=Cs{2}(i+time_jump_ID)-Cs{2}(i);
    if diff_1(i)<tol1 && diff_2(i)<tol2
        k(i)=1;
    else k(i)=0;
    end
end

for j=1:length(k)-N
    if sum(k(j:j+N))==N
        steady_start=j;
        break
    else
        steady_start=pwr_end;
    end
end
```

```

end

%computing steady state temperatures and heat flow
T1=nanmean(Cs{1}(steady_start:pwr_end));
T2=nanmean(Cs{2}(steady_start:pwr_end));
HF=nanmean(WATT(steady_start:pwr_end));
clear time_jump_ID i j diff_1 k N tol1 tol2

%% plotting
F1=figure('units','normalized','outerposition',[0 0 1 1]); %full screen✓
fig.
subplot(2,1,1);
plot(time,Cs{1},time,Cs{2},time,Cs{3},time,Cs{4},time,Cs{5},...
      time,Cs{6},time,Cs{7},time,Cs{8});
line([0,time(end)],[T_amb,T_amb],'Color','black','LineStyle','--'); %amb✓
mean
line(pwr_end*2*[1,1],[0,max(Cs{1})],...
      'Color','blue','LineStyle','--'); %pwr_end
line(steady_start*2*[1,1],[0,max(Cs{1})],...
      'Color','green','LineStyle','--'); %steady_start
line([0,time(end)],[T1,T1],'Color','cyan','LineStyle','--'); %T1 asymptote
line([0,time(end)],[T2,T2],'Color','magenta','LineStyle','--'); %T2✓
asymptote
grid minor; xlabel('time [s]'); ylabel('°C'); hold on
legend('internal C1','external C2','C3','C4','C5','C6','C7','C8',...
      'ambient mean','power interruption','steady phase start',...
      'T1 asymptote','T2 asymptote');
title('temperatures');
clear steady_start

subplot(2,1,2);
plot(time,WATT); title('power supply');
line([0,time(end)],[HF,HF],'Color','red','LineStyle','--'); %heat flow✓
mean
ylabel('heat flow [W]'); xlabel('time [s]');

%% thermal resistance
R=(T1-T2)/HF; %resistance in K/W
dT=T1-T2;

disp(' ');
disp(['La resistenza termica vale R = ',num2str(R,4),' K/W']);
disp(['La differenza di temperatura vale T1-T2 = ',num2str(dT,4),' K']);
disp(' '); disp(' ');

```


Bibliography

- [1] <https://www.energicamotor.com/motoe/>.
- [2] <http://www.mugen-power.com/english/news/detail/id=416>.
- [3] Daniel T Adams, Gene Berdichevsky, Thomas Everett Colson, Arthur Hebert, Scott Kohn, David Lyons, Noel Jason Mendez, Jeffrey Brian Straubel, Dorian West, Andrew Simpson, et al. Battery pack thermal management system, January 22 2009. US Patent App. 11/779,583.
- [4] Maan Al-Zareer, Ibrahim Dincer, and Marc A Rosen. Electrochemical modeling and performance evaluation of a new ammonia-based battery thermal management system for electric and hybrid electric vehicles. *Electrochimica Acta*, 247:171–182, 2017.
- [5] Suman Basu, Krishnan S Hariharan, Subramanya Mayya Kolake, Tae-won Song, Dong Kee Sohn, and Taejung Yeo. Coupled electrochemical thermal modelling of a novel li-ion battery pack thermal management system. *Applied Energy*, 181:1–13, 2016.
- [6] Yu-Juei Chang and Chi-Chuan Wang. A generalized heat transfer correlation for iouver fin geometry. *International Journal of heat and mass transfer*, 40(3):533–544, 1997.
- [7] Boucar Diouf and Ramchandra Pode. Potential of lithium-ion batteries in renewable energy. *Renewable Energy*, 76:375–380, 2015.
- [8] Marc Doyle, John Newman, and Jan Reimers. A quick method of measuring the capacity versus discharge rate for a dual lithium-ion insertion cell undergoing cycling. *Journal of Power Sources*, 52(2):211–216, 1994.
- [9] SJ Drake, DA Wetz, JK Ostanek, SP Miller, JM Heinzl, and A Jain. Measurement of anisotropic thermophysical properties of cylindrical li-ion cells. *Journal of Power Sources*, 252:298–304, 2014.
- [10] Stephen Drake. Thermal conduction and heat generation phenomena in li-ion cells. 2015.
- [11] Yutao Huo and Zhonghao Rao. The numerical investigation of nanofluid based cylinder battery thermal management using lattice boltzmann method. *International Journal of Heat and Mass Transfer*, 91:374–384, 2015.

- [12] Matteo Muratori. Thermal characterization of lithium-ion battery cell. 2010.
- [13] Sungjin Park and Dohoy Jung. Battery cell arrangement and heat transfer fluid effects on the parasitic power consumption and the cell temperature distribution in a hybrid electric vehicle. *Journal of Power Sources*, 227:191–198, 2013.
- [14] Zhonghao Rao, Zhen Qian, Yong Kuang, and Yimin Li. Thermal performance of liquid cooling based thermal management system for cylindrical lithium-ion battery module with variable contact surface. *Applied Thermal Engineering*, 123:1514–1522, 2017.
- [15] Luca Sandrucci. Ottimizzazione di un impiantodi raffreddamento per una vettura formula sae. 2015.
- [16] Ali M Sefidan, Atta Sojoudi, and Suvash C Saha. Nanofluid-based cooling of cylindrical lithium-ion battery packs employing forced air flow. *International Journal of Thermal Sciences*, 117:44–58, 2017.
- [17] Shoichiro Watanabe, Masahiro Kinoshita, Takashi Hosokawa, Kenichi Morigaki, and Kensuke Nakura. Capacity fading of lialyni1- x- ycoxo2 cathode for lithium-ion batteries during accelerated calendar and cycle life tests (effect of depth of discharge in charge–discharge cycling on the suppression of the micro-crack generation of lialyni1- x- ycoxo2 particle). *Journal of Power Sources*, 260:50–56, 2014.
- [18] Naixing Yang, Xiongwen Zhang, BinBin Shang, and Guojun Li. Unbalanced discharging and aging due to temperature differences among the cells in a lithium-ion battery pack with parallel combination. *Journal of Power Sources*, 306:733–741, 2016.
- [19] Matthew Yates, Mohammad Akrami, and Akbar A Javadi. Analysing the performance of liquid cooling designs in cylindrical lithium-ion batteries. *Journal of Energy Storage*, page 100913, 2019.
- [20] Haobing Zhou, Fei Zhou, Qian Zhang, Qianzhi Wang, and Zebin Song. Thermal management of cylindrical lithium-ion battery based on a liquid cooling method with half-helical duct. *Applied Thermal Engineering*, 162:114257, 2019.
- [21] Muhammad Fahad Zia, Elhoussin Elbouchikhi, and Mohamed Benbouzid. Optimal operational planning of scalable dc microgrid with demand response, islanding, and battery degradation cost considerations. *Applied Energy*, 237:697–707, 03 2019.